MASTER THESIS

SUBDUCTION-INDUCED BREAK-UP AND DRIFTING OF CONTINENTAL PLATES

LUCA DAL ZILIO

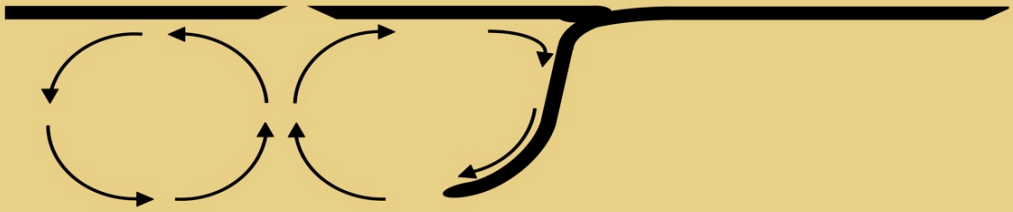

Supervisor

Dr. Manuele Faccenda

Università degli Studi di Padova
Department of Geosciences

Co-supervisor

Dr. Fabio A. Capitanio

Monash University
School of Geosciences

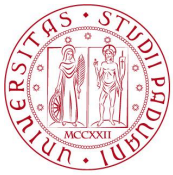

UNIVERSITÀ DEGLI STUDI DI PADOVA

MONASH University

SUBDUCTION-INDUCED BREAK-UP AND DRIFTING OF CONTINENTAL PLATES

A dissertation submitted to
Università degli Studi di Padova
Facoltà di Scienze MM. FF. NN.
Department of Geosciences

for the Master degree of
Geologia e Geologia Tecnica (LM-74)

presented by

Luca Dal Zilio
born on January 25 1989
citizen of Italy

accepted on the recommendation of
Dr. Manuele Faccenda (supervisor)
Dr. Fabio A. Capitanio (co-supervisor)

2014

"No great discovery was ever made without a bold guess"
— Isaac Newton

Abstract

Since the early theory of Wegener, the break-up and drift of continents have been controversial and hotly debated topics. To assist the interpretation of the break-up and drift mechanisms and its relation with mantle circulation patterns, we carried out a 2-D numerical study that will provide insight into the dynamics of these processes. Different regimes of upper plate deformation are studied as consequence of stress coupling with mantle convection patterns. The most important results indicate that three different styles of subduction can be defined by increasing the viscosity contrast between upper and lower mantle: penetrating slab, slab avalanche and stagnant slab. Subduction of the oceanic plate induces mantle flow that, in turn, exerts basal tractions on the upper plate. These acting mantle drag forces (F_{MD}) can be subdivided in two types: (1) active mantle drag occurring when the flow drives plate motion (F_{AD}), and (2) passive mantle drag (F_{PD}), when the asthenosphere resists plate motion. The active traction generated by the subduction-induced convective cell is counterbalanced by passive mantle viscous drag away from it and therefore tension is generated within the continental plate. The shear stress profiles indicate that break-up conditions are met where the gradient of the basal shear stress is maximized. However the break-up location varies largely depending on the convection style primarily controlled by slab stagnation on the transition zone or by slab penetration into the lower mantle. Our study, compared with real subduction settings, suggests that: (1) The stagnating slab models with break-up at about 250-350 km from the trench and drifting of small continental portions can be compared with the evolution of the Japan Arc and the opening of the Western Mediterranean, where stagnant slabs and microcontinents migrated following the retreat of the Pacific and Ionian slab, respectively. (2) The penetrating slab model with break-up at about 2800-3500 km from the trench and drifting of large continental plates could explain the opening of the Atlantic Ocean and westward drifting of the South and North American Plates following the retreat of the ~15000 km wide Farallon Plate. Good correspondences between our models and these convergent margins provide an alternative interpretation for their evolution and, more in general, for the break-up and drifting mechanisms of continents.

Contents

Chapter 1

Introduction

It was the German geophysicist Alfred Wegener in the early 20^{th} century (Wegener, 1920) who first suggested a theory of continental drift after he had recovered the striking similarity between the coastlines of South America and Africa, located on opposite sides of the Atlantic Ocean. He concluded that these two continents had once been merged. Wegener pushed his new idea even further and proposed that once all landmasses had been clustered into a single super-continent, which is now called Pangaea. At the time it was first promoted, Wegener's theory remained highly controversial and literally divided the geoscience community into supporters and challengers, who simply neglected his revolutionary ideas, particularly because Wegener was not able to provide a mechanism that could drive continental drift. He tried to explain the motion of continents by tidal and centrifugal forces, but it turned out soon after his proposition that these forces are too small. It took several years until Arthur Holmes suggested a more consistent explanation for Wegener's ideas: vigorous convection taking place in the Earth's mantle (Holmes, 1931). This suggestion was highly innovative, but on the other hand its proof was quite difficult at that time and it took almost

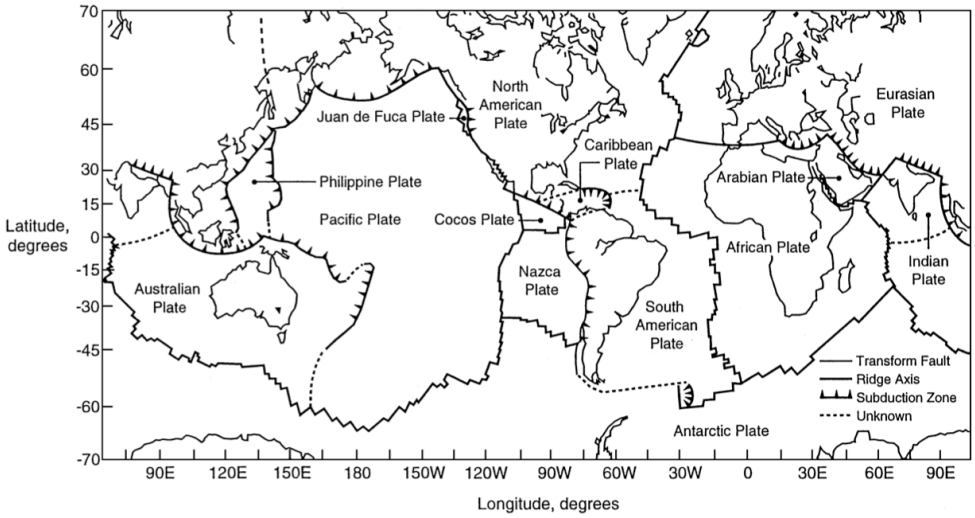

Figure 1.1: Distribution of the major tectonic plates. The ocean ridge axis (accretional/divergent plate margins), subduction zones (disruptive/convergent plate margins), and transform faults (conservative plate margins) that make up the plate boundaries are shown. From Turcotte & Schubert (2002)

three more decades until observational evidence in the form of seafloor spreading was found (Hess, 1962). The ideas of Wegener and Holmes paved the way for a new theory, which is nowadays well-accepted and forms the standard model for any large-scale geodynamic problem: the theory of plate tectonics, which links the motion of plates at the surface to the convection in the mantle.

1.1 Plate tectonics

Earth's outermost stiff layer, known as lithosphere, is subdivided into a dozen of larger and many other smaller fragments: the tectonic plates (Fig. 1.1). Individual plates are characterized by quasi-rigid motion with little internal deformation and more or less uniform velocity (e.g. Bird, 2003). Different plates, however, are separated by narrow zones in which

most of the surface deformation takes place. Where two lithospheric plates diverge at mid-oceanic spreading ridges, new material rises to the surface and causes the growth of young lithosphere. As it moves apart from the oceanic spreading ridges, the oceanic lithosphere experiences significant cooling, which causes a density increase. Once a critical density is reached, the lithosphere is recycled back into the Earth's interior by subduction, which takes place at convergent plate boundaries. The major present-day belt of subduction zones encompasses the Pacific plate and is called Ring of Fire (see Fig. 1.2). Some convergent plate boundaries are characterized by tensional forces caused by oceanic trench rollback (i.e. the oceanic trench is wandering in the seafloor direction) and the overriding plate is stretched up to form a back-arc basin; a well example of back-arc marginal basin is the Sea of Japan.

The evolution of the tectonic plates can be simply explained through the Wilson's Cycle (Wilson, 1966). The first step is the break-up of a continent and occurs on continental rift zones. The first stage of the splitting process is the formation of a rift valley. Two mechanisms for continental rifting, active and passive, have been proposed by Turcotte & Emerman (1983):

1. The passive mechanism hypothesizes that the continental lithosphere fails under tensional stresses transmitted through the elastic lithosphere by plate margin forces (e.g., trench suction). In this mechanism volcanism and uplift associated with rifting are secondary processes.

2. The active mechanism hypothesizes that a mantle plume impinges on the base of the continental lithosphere causing volcanism and

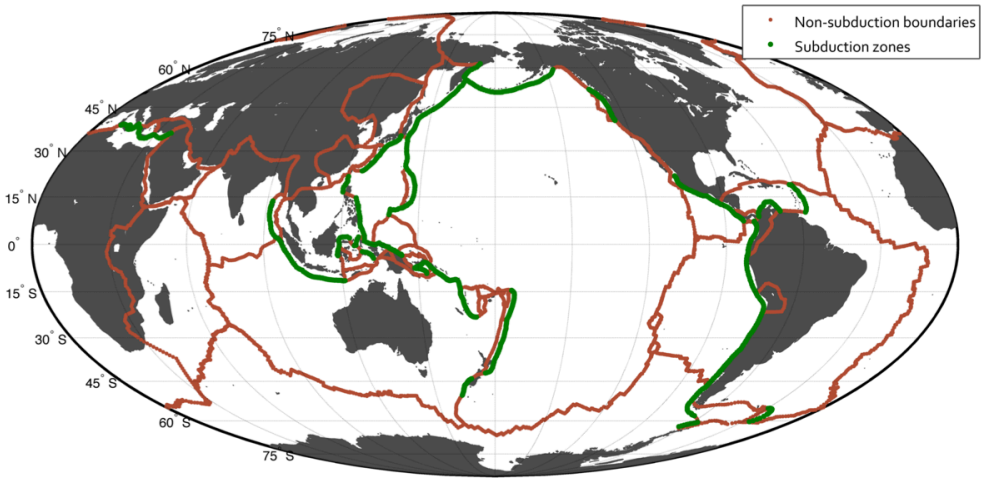

Figure 1.2: Plate boundary on Earth, shows convergent boundaries (green) and non-convergent boundaries (red). From Bird (2003).

uplift. In this mechanism the tensional failure of the lithosphere is a secondary process.

The second step of the Wilson's Cycle is the opening of the ocean. However, there is ample evidence in the geological record that some rift valleys (aulacogen) never evolved into an ocean; in other words, the splitting process may be aborted. On the other hand, if a further horizontal extension occurs, a new ocean ridge can be formed. This is how the Atlantic Ocean initially formed and subsequently expanded owing to the westward drift of both North- and South-American plates relative to the Eurasian and African plates.

However, the break-up and drift of continents have been controversial and hotly debated topics due to the inability to explain how these mechanisms take place.

1.1.1 Driving forces

Mantle convection in rocky planetary body is mainly driven by heat in its interior:

- **Accretion and differentiation** of the planet provides potential energy that is converted to one part of the total heat in the Earth's interior (Birch, 1965).
- **Cooling** is the loss of primordial heat of the planet and makes up a substantial fraction (~25%) of today's surface heat flow (Schubert *et al.* , 1980).
- **Radioactive decay**of the uranium, thorium and potassium isotopes result in heat makes up most of today's total heat flow (Schubert *et al.* , 1980).

The heat from accretion and differentiation, cooling and radioactive decay can be converted to material motion by thermal convection.
Additionally, the Earth has negatively buoyant plates and is thus able to evolve in a mobile-lid style. The negative buoyancy of the plates is, however, only one of the several forces acting on mobile plates (Fig. 1.3) that can promote or resist their motion. Some of these forces acting on the bottom or the edges of plates are listed below (Forsyth & Uyeda, 1975):

- **Slab pull (F_{SP})** promotes the downwelling and converging motion of plates and arises from the negative buoyancy of the down-going plate portion. The slab is colder and thus heavier than the mantle material surrounding it. An older plate and a wider subduction zone increase the slab pull. Slab pull together with slab suction is thought to make up the major force ($\geq$90%) acting on lithosphere

plates. The descending motion contributes to mantle circulation, and thus acts indirectly as a driving force for plate motions.

- **Mantle drag (F_{DF} + F_{CD}).** The force acting at the bottom surface of plates is due to the viscous coupling between plates and underlying asthenosphere; this force is called mantle drag force (F_{DF}). If there is an active flow in the asthenosphere, such as thermal convection or induced by descending lithosphere during subduction processes, F_{DF} will act as a driving force (e.g. Turcotte & Oxburgh, 1972). If, on the other hand, the asthenosphere is passive with regard to the plate motion, F_{DF} will be resistive force. Because of the possible difference in the rheological properties of the asthenosphere under oceanic and continental plates, the drag force acting on continental plates may be different from that acting on oceanic plates. Therefore, Forsyth & Uyeda (1975) have introduced an additional drag force is considered for continental plates, the continental drag (F_{CD}). The drag acting on continental plate is thus expressed as F_{DF} + F_{CD}.

- **Ridge push (F_{RP})** is another positive forcing for a mobile lid and makes up ~10% of the total. The force is mainly exerted by gravitational sliding from the elevated ridge toward the lower trench.

- **Slab resistance (F_{SR})** is the force opposing plate motions and occurs when the sinking slab has reached a thermal equilibrium with its surrounding mantle but still pushed further down into the stiffer mantle.

- **Transform resistance (F_{TF})** is the friction force to a transform motion at the conservative contact zone between two plate portions.

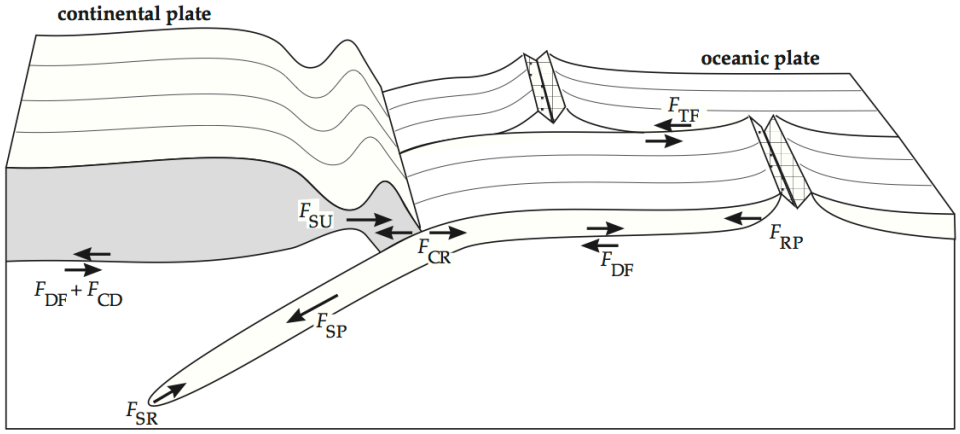

Figure 1.3: Forces controlling subducting lithosphere plates. Reproduced from Lowrie (2007) after Forsyth & Uyeda (1975).

It therefore acts as a resisting force for subduction.

- **Trench suction (F_{SU} or F_{TS})** is the dragging of the continental plate towards the trench caused by increased bending of the descending lithosphere or due slab rollback. When the slab retreats, the upper plate, if coupled with the lower one, is forced to 'flow' in the same direction because mass continuity does not allow formation of voids.

- **Bending friction (F_{CR})** is the internal friction arising due to the enforced deformation (mostly bending) of the plate at the subduction zone.

In summary, the driving forces on plates are slab pull, trench suction, ridge push on the upper plate. The motions are opposed by slab resistance, collision resistance and transform fault forces. Whether the forces between plate and mantle (i.e. mantle drag) promote or oppose motion, depends on the relative motion between the plate and the mantle. The

motive force of plate tectonics is clearly a composite of these several forces. Some can be shown to be more important than others, and some are insignificant. However, it is believed that descending slabs are the main driver of plate tectonics because observations revealed that plates velocity strongly correlates with its trench length, while it does not correlate with its ridge length (Forsyth & Uyeda, 1975). It is important to consider that the amount of contribution of each of these forces to a specific plate motion can strongly vary.

1.1.2 Linking between plates and mantle flow

If feasibility of mantle convection is accepted, still remains some doubt as to the form it takes. There are uncertainties as to the role played by the seismic discontinuities at 400 km and 670 km depth, which bound the upper-mantle transition zone. The discontinuities are not sharp, and are understood to represent mineral phase changes rather than compositional differences (as, for example the crust-mantle and core-mantle boundaries). In principle, we can assume that mass can be carried by convection currents across these discontinuities.

There are two main models of mantle convection, each with an interface at the 670 km seismic discontinuity (Fig. 1.4). An important change in viscosity occurs at this level. In whole-mantle convection system (Fig. 1.4a) the viscosity increases from the upper mantle to the lower mantle and there is a net flow of material across the boundary. In this model, convection ensures that the entire mantle is well mixed mechanically, and the phase changes at 400 and 670 km have only a small effect on the temperature gradient. This model agrees with much of the available evidence.

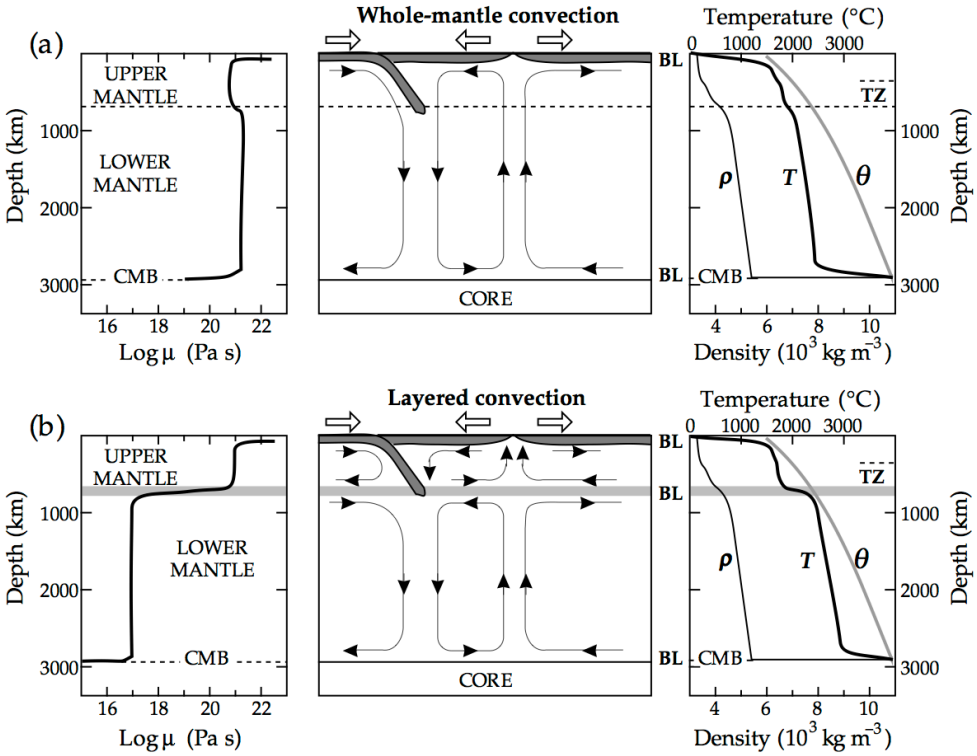

Figure 1.4: Possible convection flow pattern (center) and profiles of viscosity (left), density, temperature and solidus temperature (right) for (a) whole-mantle convection and (b) layered mantle convection. TZ is the upper-mantle transition zone, BL are boundary layers, CMB is the Core-Mantle Boundary. From Peltier (1989).

The alternative layered convection model has distinct convecting layers in the upper and lower mantle (Fig. 1.4b). There are two ways in which this can take place:

1. The upper and lower convection patterns in a vertical section may represent circulations in the same sense (as in Figure 1.4b).

2. The upper and lower convection patterns have opposite senses.

Opposite senses of circulation in the layers would cause little or no shear between the tangential flows at the boundary, resulting in mechanical coupling between the layers. However, if the layered flow patterns have

the same sense of circulation, hot material rising in the upper mantle overlies hot material rising in the lower mantle, so that the flow regimes are coupled thermally. This model has a strong velocity shear across the 670 km discontinuity, which requires a large and abrupt change in viscosity at this depth; viscosity in the lower mantle would need to be at least two orders of magnitude smaller than in the upper mantle. Estimates of mantle viscosity indicate the opposite: viscosity is higher in the lower mantle than in the upper mantle (Lowrie, 2007).

The problem of understanding mantle convection is complicated by the non-uniform structure and rheology of the mantle. As yet, there is no complete picture of how the various factors that influence convection act together. Convection patterns depend strongly on what happens physically and thermodynamically at the 670 km discontinuity and this can only be inferred indirectly. Our understanding of the discontinuity is incomplete, but it is essential to resolve the real pattern of mantle convection.

1.2 Framework of this thesis

This dissertation is embedded with the SINDRICO project under the supervision of Dr. Manuele Faccenda (PI - principal investigator) and co-supervision of Dr. Fabio A. Capitanio (Monash University) and has been developed at University of Padua - Department of Geosciences. SINDRICO project (i.e. **S**ubduction-**IN**duced break-up and **DRI**fting of **CO**ntinental plates) is an interdisciplinary project, which links numerical modeling and geophysics with the aim to improve the knowledge of

the Earth's mantle behaviour, the break-up and drifting mechanisms of the continental plates during the subduction processes. Computational resources of this project are supported through the high-performance computing facilities at CINECA, Bologna (Italy).

1.3 Motivation

Understanding the dynamics of the Earth's interior is important for several reasons. Convection is the most important process within the mantle and is mainly responsible for the evolution of our planet (Schubert *et al.* , 2001). It controls the distribution of land and water bodies over geological time scales. An important function of mantle convection is the heat transport from the hot deep interior to the surface. In doing so, it forms continents and causes them to drift; it is responsible for volcanism, earthquakes and mountain building.

On the other hand, subduction processes are highlighted due to the role they play in the global dynamics: they provide the most important driving force and form the sites of interaction between Earth's interior and the surface; hence, it is crucial to understand the dynamics of subduction and its effects. Subduction is a dynamically complex process controlled by two converging plates characterized by highly non-linear rheologies, in contact with surface and upper mantle and eventually with the deep mantle.

The motivation of the project is to deepen our understand of mantle flow induced by the descending lithosphere and how such mantle flow

may affect continental plates. Especially, the present research try to shed light on the dynamic evolution of the Earth's mantle during subduction processes characterized by the presence of continental plates, in order to reproduce geodynamic contexts comparable to those observed nowadays as well as those indicated by the geological record.

1.4 Aims of the thesis

The aim of the project is to understand: (1) which is the size of the poloidal convective cell forming above the subducting slab responsible for the breakup and drifting of the continent as a function of the convective pattern (layered vs. whole mantle convection) and viscosity ratio between the upper and lower mantle, (2) in which conditions continental break-up and drifting can occur, (3) which is the size of the drifting continent as a function of the poloidal convective cell size.

Through a deep analysis of these points, we want to reach the central goal of this thesis: provide a new interpretation for the break-up and drifting of continental plates.

1.5 Outline

After this general introduction to the research topic, the motivation and main aims of this thesis, the remainder of this section lists the thesis's structure.

The present dissertation has been organized in individual chapters as

follows:

- **Chapter 2** describes the numerical methods. Firstly, the used I2VIS code accounting for visco-plastic rheology is presented. Then, the fundamental thermo-mechanical equations and the mixed Eulerian-Lagrangian scheme, followed by the rheological model and boundary condition are y explained. Finally, the numerical technique to reproduce mantle phase transitions, the computational strategy adopted and the main abbreviations used are described.

- **Chapter 3** deals with one of the fundamental problems of the plate tectonics: how the subduction induces the break-up and drifting of continental plates. To reproduce large-scale geodynamic settings, we have used I2VIS, a petrological-thermo-mechanical 2-D code. This chapter describes the model setup for each simulation and the corresponding outputs. Finally, further and more realistic numerical settings are tested. In addition, a 1-D MatLab code (called YSE_1D) was written to compute the yield strength envelope, the integrated strength (B) and the elastic thickness (Te) of the continental plates. As a powerful tool, YSE_1D can be used to compare the I2VIS-outputs. Additional information can be found in the Appendix A.

- **Chapter 4** presents an efficient and simple 2-D mechanical code (called SINDRICO) written in MatLab using the finite-difference method. The code describes the evolution of the mantle flow pattern affected by different viscosity contrast between upper and lower mantle; all variables are scaled from factors initially defined. Numerical approach and the results are presented and compared

with the I2VIS-simultations. Additional information can be found in the Appendix B.

- **Chapter 5** focuses on the evolution of real ocean-continent convergent margins, such as the North and South American plates, Calabria, Sardinia, Corsica microplates and the Japan arc. It presents the geophysical data (e.g. tomography data, plate tectonics reconstruction etc.) to evaluate the correspondence with our results.
- **Chapter 6** systematically summarizes the most important findings of this thesis. Finally, last section highlights some on-going and possible future researches related to the topic.

Chapter 2

Numerical methods

For this project, we have used I2VIS, a petrological-thermo-mechanical 2D code developed by *Taras V. Gerya (ETH, Zürich)* and designed for realistic simulations of tectonic, geodynamic and planetary processes.
The code is based on finite differences (FD) method and marker-in-cell (MIC) technique, it uses a complex viscoplastic rheology of rocks and it accounts for changes in topography due to erosion-sedimentation processes and for changes in physical properties of rocks due to phase transformations. The initial model setup varies according to the given geodynamical process of investigation. I will describe in the following chapters the numerical setup used in this study.

2.1 I2VIS

All numerical models described in the thesis were performed with the I2VIS code (Gerya & Yuen, 2003) using conservative finite differences (FD) scheme of first order accuracy and a non-diffusive marker-in-cell technique (e.g. Moresi *et al.* , 2003) to simulate multiphase flow. The I2VIS code is a petrological-thermo-mechanical code that solves numer-

ically the equations of conservation of mass, momentum and energy (Gerya & Yuen, 2003).

A Eulerian/Lagrangian primitive variable formulation is combined with a moving markers technique (e.g. Woidt, 1978; Christensen, 1982). Advection of markers is done using a fourth-order in space, first order in time explicit Runge-Kutta interpolation scheme applied to the globally calculated velocity field on the Eulerian grid (Gerya & Yuen, 2003). The conservative finite-difference scheme is designed over a non-uniformly spaced fully staggered grid in the Eulerian form configuration (Fig. 2.1). Discretization of the thermo-mechanical equations on the fully staggered grid is very natural, gives simple FD formulas (Gerya, 2010), prevents pressure oscillations and leads to a notably higher accuracy (up to four times, Fornberg, 1998) than that on a non-staggered grid. The non-uniform grid is extremely useful in handling geodynamical situations with multiple-scale character, such as in a subducting slab and the wedge flow above it (Davies & Stevenson, 1992). The material properties are initially distributed on Lagrangian points and advected according to a computed velocity field. The material properties are then interpolated from displaced Lagrangian points to the Eulerian grid by using a weighted-distance averaging to solve the equations. The adopted computation strategy is explained in detail in Section 2.5 and is shown schematically in Figure 2.7.

2.2 Fundamental equations

The governing conservation equations of mass, momentum and energy and the constitutive relationships between stress and strain-rate (needed

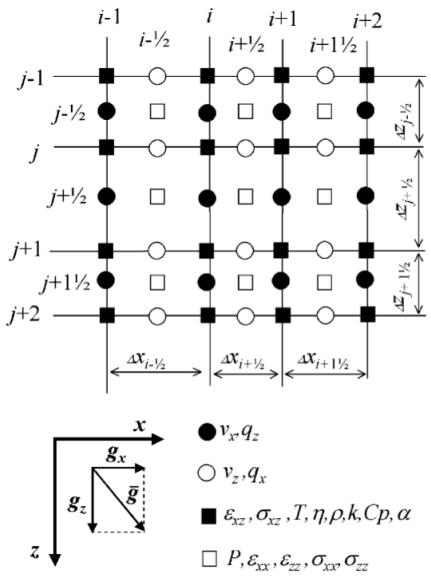

Figure 2.1: Schematic representation of non-uniform rectangular staggered Eulerian grid used for the numerical solution of equations; g_x and g_z are components of gravitational acceleration in the $x-z$ coordinate frame. Different symbols correspond to the nodal points for different scalar properties, vectors and tensors $i, i+1/2$, etc. and $j, j+1/2$, etc. indexes represent the staggered grid and denote, respectively, the horizontal and vertical positions of four different types of nodal points. Many variables ($V_x, V_z, \sigma_{xx}, \sigma_{xz}, \sigma_{zz}, \varepsilon_{xx}, \varepsilon_{xz}, \varepsilon_{zz}, P, T, \eta, \rho, k, C_p$,etc.), up to around 25 at grid point, are part of the voluminous output in this code. From (Gerya & Yuen, 2003).

in the creeping flow regime) are solved on an irregularly spaced staggered grid in Eulerian configuration (Gerya & Yuen, 2003).

2.2.1 Conservation of mass

The equation establishes the balance of mass within an elementary volume during the displacement of continuous medium. The Eulerian continuity equation (i.e. for fixed elementary volume) has the following general form:

$$\frac{\partial x}{\partial t} + \nabla(\rho\, \vec{v}) \;=\; 0\,; \tag{2.1}$$

where ρ is the local density and $\vec{v}$ is the local velocity vector. In our models the material is assumed to be compressible (i.e. density of material points may change with time). And thus, the 2-D continuity equation has the form:

$$\frac{\partial v_x}{\partial x} + \frac{\partial v_z}{\partial z} = -\frac{1}{\rho}\frac{D\rho}{Dt}\,; \tag{2.2}$$

where $\frac{D\rho}{Dt} = \frac{d\rho}{dt} + \vec{v}\,\nabla(\rho)$ is the *substantive density time derivative*, v_x and v_z are, respectively, the horizontal and vertical velocity component, x and z denote horizontal and vertical Cartesian coordinates.

2.2.2 Conservation of momentum

The relationship between internal and external forces acting on the material and deformation of material is governed by the *2D-Stokes equation* for slow flow and takes the following form:

$$\frac{\partial \sigma_{ij}}{\partial x_j} + \rho g_i = \rho\left(\frac{\partial v_i}{\partial t} + v_j\frac{\partial v_i}{\partial x_j}\right)\,; \tag{2.3}$$

or by separating the stress into deviatoric and isotropic components:

$$\frac{\partial \sigma'_{ij}}{\partial x_j} - \frac{\partial P}{\partial x_i} + \rho g_i = \rho\left(\frac{\partial v_i}{\partial t} + v_j\frac{\partial v_i}{\partial x_j}\right)\,; \tag{2.4}$$

where x_i and x_j are coordinates, σ is stress tensor, σ' is deviatoric stress tensor, g_i is gravity acceleration component, P is pressure, v_i and v_j are velocity vector components. Taking into account the fact that rocks behave as a highly viscous fluid at geological time scales and thus the term on the right-hand side is negligible ($\sim n$ x 10^{-22} m/s^2) compared

to the term ρg_j on the left-hand side, the deformation can be accurately described by the Stokes equation of slow flow:

$$\frac{\partial \sigma'_{ij}}{\partial x_j} - \frac{\partial P}{\partial x_i} + \rho g_i = 0\,; \tag{2.5}$$

which in 2-D reads:

$$\frac{\partial \sigma'_{xx}}{\partial x} + \frac{\partial \sigma'_{xz}}{\partial z} - \frac{\partial P}{\partial x} = 0\,; \tag{2.6}$$

$$\frac{\partial \sigma'_{zz}}{\partial z} + \frac{\partial \sigma'_{xz}}{\partial x} - \frac{\partial P}{\partial z} = -\rho g_z\,; \tag{2.7}$$

The density depends on P (pressure), T (temperature) and C (composition). σ'_{xx}, σ_{xz}, σ'_{zz} are the deviatoric stress tensor components. The components of the deviatoric stress tensor (σ'_{ij}) are calculated using the viscous constitutive relationship between stress and strain rate ($\dot{\varepsilon}$) for a compressible fluid (Gerya & Yuen, 2007), as follows:

$$\sigma'_{ij} = 2\eta \left(\dot{\varepsilon}_{ij} - \frac{1}{3}\delta_{ij}\dot{\varepsilon}_{kk} \right) + \delta_{ij}\,\eta_{bulk}\,\dot{\varepsilon}_{kk} \approx 2\eta \left(\dot{\varepsilon}_{ij} - \frac{1}{3}\delta_{ij}\dot{\varepsilon}_{kk} \right)\,; \tag{2.8}$$

$$\dot{\varepsilon}'_{xx} = \frac{1}{2}\left(\frac{\partial v_x}{\partial x} + \frac{\partial v_x}{\partial x} \right)\,; \tag{2.9}$$

$$\dot{\varepsilon}'_{xz} = \frac{1}{2}\left(\frac{\partial v_x}{\partial z} + \frac{\partial v_z}{\partial x} \right)\,; \tag{2.10}$$

$$\dot{\varepsilon}'_{zz} = \frac{1}{2}\left(\frac{\partial v_z}{\partial z} + \frac{\partial v_z}{\partial z} \right)\,; \tag{2.11}$$

Transport coefficient η represents the viscosity, which depends on the temperature (T), pressure (P), composition (C) and strain-rate ($\dot{\varepsilon}$). δ_{ij} is the Kronecker delta: $\delta_{ij} = 1$ when $i = j$ and $\delta_{ij} = 0$ when $i \neq j$, while $\dot{\varepsilon}_{kk}$ is the bulk strain rate.

2.2.3 Conservation of energy

The temperature changes in a continuum are due to either internal heat generation or advective and conductive heat transport. The balance of heat is described by the heat conservation equation, which in 2D Eulerian frame is:

$$\rho C_p \left(\frac{\partial T}{\partial t} + v \, grad(T) \right) = -\frac{\partial q_x}{\partial x} - \frac{\partial q_z}{\partial z} + H_r + H_a + H_s + H_l \, ; \quad (2.12)$$

$$q_x = -k(T, P, C) \frac{\partial T}{\partial x} \, ; \quad (2.13)$$

$$q_z = -k(T, P, C) \frac{\partial T}{\partial z} \, ; \quad (2.14)$$

where q_x and q_z are heat flux components; $k = f(P, T, C)$ is thermal conductivity which depends on the pressure-temperature conditions and composition (Hofmeister, 1999). H_r, H_a, H_s and H_l are, respectively, radioactive, adiabatic, shear and latent heat production. Radioactive heat production dependent on the rock type (Turcotte & Schubert, 2002) and is assumed to be constant:

$$H_r = const(C) \, ; \quad (2.15)$$

The adiabatic heat production/consumption is related to pressure changes (compression - decompression):

$$H_a = T \propto \left(v_x \frac{\partial P}{\partial x} + v_z \frac{\partial P}{\partial z} \right) ; \tag{2.16}$$

The shear heat production is related to dissipation of mechanical energy during viscous deformation and depends on the deviatoric stress and deviatoric strain rate:

$$H_s = \sigma'_{xx}\, \dot{\varepsilon}'_{xx} + \sigma'_{zz}\, \dot{\varepsilon}'_{zz} + 2 \cdot \sigma'_{xz}\, \dot{\varepsilon}'_{xz} ; \tag{2.17}$$

The effect of latent heating related to the phase transformations of the rocks is included implicitly by calculating the effective heat capacity (Cp_{eff}) and the thermal expansion (α_{eff}) of the phase transformations as it is explained in the Section 2.4.

2.2.4 Marker-in-cell technique

Very accurate advection of non-diffusive properties such as rock type (composition) with strongly discontinuous (e.g., layering) distribution in space is fundamental. I2VIS combines the use of Lagrangian advecting points (also called markers or particles) with an immobile Eulerian grid (e.g. Woidt, 1978; Christensen, 1982; Schmeling, 1987; Weinberg & Schmeling, 1992). In this approach, physical properties are initially distributed on a large amount of Lagrangian particles (for example, more than 8 million particles are used in our models) that are advected according to a given velocity field interpolated from the Eulerian nodes. The advected material properties (e.g. density, viscosity, etc.) are then

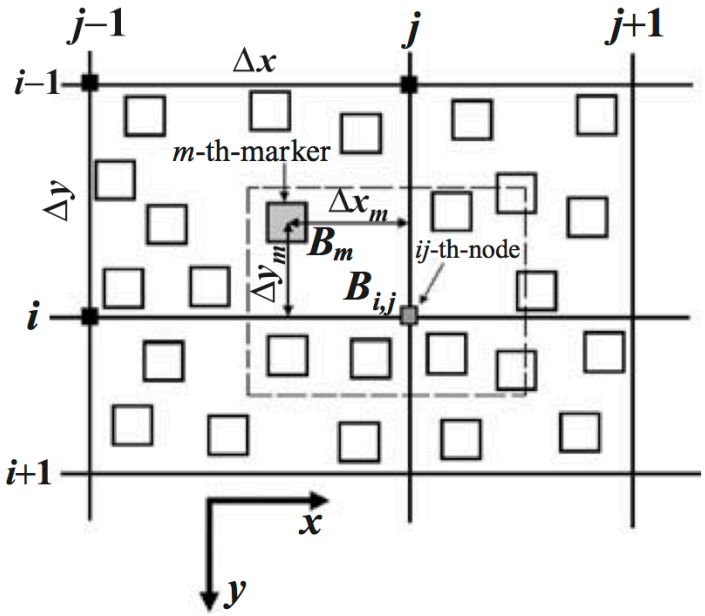

Figure 2.2: Scheme of 2D grid used for the interpolation of physical properties from the markers to the nodes. The dashed boundary indicates the area from which markers are used for interpolating properties to node (i, j) in the case of a 'local' interpolation scheme. From (Gerya & Yuen, 2003).

interpolated from the displaced Lagrangian points to the Eulerian grid (Fig. 2.2) by using a weighted-distance averaging:

$$\rho_i^{t+\Delta t} = \left(\sum_m \rho_m w_{m(i)} / \sum_m w_{m(i)} \right) ; \tag{2.18}$$

$$w_{m(i)} = \left(1 - \frac{\Delta x_{m(i)}}{\Delta x} \right) ; \tag{2.19}$$

2.2.5 Rheology

The rheology used in this study is visco-plastic. The viscous creep of rocks is defined in terms of deformation invariants and depends on tem-

perature, pressure and strain rate. The effective viscosity for dislocation creep is defined as follows (Ranalli, 1995):

$$\eta_{creep} = \frac{1}{2} A_D^{\frac{1}{n}} \dot{\varepsilon}_{II}^{\frac{1}{n}-1} exp\left(\frac{E_a + PV_a}{nRT}\right) ; \tag{2.20}$$

where $\dot{\varepsilon}_{II}$ is the second invariant of the strain rate tensor. A_D (pre-exponential factor), E_a (activation energy), n (creep exponent), V_a (activation volume) are experimentally determined flow law parameters and R is the gas constant. At low deviatoric stresses, thermally activated diffusion becomes the dominant creep mechanism. Following Turcotte & Schubert (2002), it is assumed a transition from dislocation to diffusion creep at a given deviatoric stress, τ_{II-trs}, implying that:

$$\eta_{creep} = \frac{1}{2} A_D \, {\tau_{II-trs}}^{1-n} exp\left(\frac{E_a + PV_a}{RT}\right) ; \tag{2.21}$$

A low transition stress value (τ_{II-trs} = 0.03 MPa) favouring dislocation creep is used for the upper mantle and the lower mantle.
Visco-plasticity is implemented using the following yield criterion, which limits the creep viscosity, altogether yielding an effective visco-plastic rheology:

$$\eta_{creep} \leq \frac{\sigma_{yield}}{2\dot{\varepsilon}_{II}} ; \tag{2.22}$$

where σ_{yield} is defined by the Drucker-Prager yield criterion:

$$\sigma_{yield} = c + \mu \cdot P\,(1 - \lambda_{fluid}) ; \tag{2.23}$$

and by the von Mises yield criterion:

$$|\sigma_{yield}| = const. ; \tag{2.24}$$

where μ is coefficient of friction, defined as

$$\mu = tan(\varphi)\,; \tag{2.25}$$

and λ_{fluid} is the pore fluid pressure factor

$$\lambda_{fluid} = \frac{P_{fluid}}{Psolid}\,; \tag{2.26}$$

The local plastic strength of a rock depends on invariant variables, such as the mean stress $P_{solid} = P$ (dynamic pressure), the cohesion c, which is the strength at $P = 0$, and depends on the internal friction coefficient μ, which is a function of the internal friction angle φ. Additionally, plastic strength depends on λ_{fluid}, interpreted as pore fluid pressure factor. The pore pressure P_{fluid} reduces the yield strength σ_{yield} of fluid-containing porous or fractured media. In our numerical experiments λ_{fluid} of the hydrated oceanic crust (Faccenda, 2014b, Water in the slab: a trilogy) was varied from 0.2 to 0.3 for different runs. In all rock type, brittle weakening is implemented through the following conditions:

$$\begin{cases} if\ \varepsilon < \varepsilon_0 \Rightarrow \mu = \mu_0\,; \\ if\ \varepsilon_0 < \varepsilon < \varepsilon_1 \Rightarrow \mu = \mu_0 + (\mu_1 - \mu_0)(\frac{\varepsilon - \varepsilon_0}{\varepsilon_1 - \varepsilon_0})\,; \\ if\ \varepsilon > \varepsilon_1 \Rightarrow \mu = \mu_1\,; \end{cases} \tag{2.27}$$

where μ_0 and μ_1 are the coefficient of friction at zero deformation and at strain ε_1; Figure 2.3 schematizes as $\mu = f(\varepsilon)$. Brittle weakening is needed to ensure lubrication at the plates contact after bending-related deformation. Given that the models have relatively low resolution, very low values of μ_0, μ_1 and ε_1 are needed to ensure an efficient lubrication on the top boundary of the subducting slab. Although simplified,

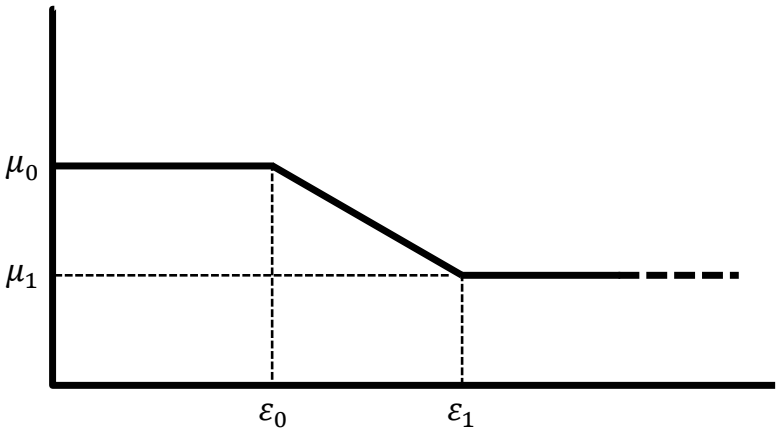

Figure 2.3: Schematic representation of how the coefficient of friction (μ) is a function of the strain (ε). The chosen values of μ_0, μ_1, ε_0 and ε_1 are summarized in Chapter 3.

such layered rheological structure captures the essential characteristic of the lithosphere yielding profile producing realistic subduction patterns (e.g. Faccenda, 2014a). All chosen values of coefficients of friction and corresponding strain are defined in Chapter 3. At high pressure the strength of rocks is limited by the Peierls mechanism (Karato *et al.* , 2001; Katayama & Karato, 2008), which is a temperature-dependent mode of plastic deformation that takes over from the dislocation mechanism at elevated stresses and low temperatures:

$$\eta_{creep} = \frac{1}{2A_{peierls}\sigma_{II}} exp\left(\frac{E_a + PV_a}{nRT}\left(1 - \left(\frac{\sigma_{II}}{\sigma_{peierls}}\right)^p\right)^q\right) ; \qquad (2.28)$$

where $A_{peierls}$ is the material constant for Peierls creep ($Pa^{-2}s^{-1}$), σ_{II} is the second invariant of the stress tensor, $\sigma_{peierls}$ is the Peierls stress that limits the strength of the material and corresponds to 9.1 GPa. Exponents p and q depend on the shape and geometry of obstacles that

limit the dislocation motion and are equal to 1 and 2, respectively. The Peierls mechanism is a dominant deformation mechanism of the down-going slab, where the temperature is low and stress is high (e.g. Karato *et al.* , 2001). According to our rheological model, plastic deformation of fluid containing rocks is affected by the fluid pressure factor (P_{fluid}). Because water is also expected to have an effect on viscous deformation, different flow laws are used for dry and fluid containing rocks. As a result, the effective viscosity of rocks at relatively cold temperatures is dominated by the solid pressure and by the weakening effects of fluids. Temperature, solid pressure and deviatoric stress, on the other hand, are dominant factors, controlling the viscosity of hot rocks. n x 10^{16} and n x 10^{25} $Pa\ s$ are the lower and upper cut-off values for viscosity of all types of rocks in our numerical experiments.

2.3 Boundary conditions

For all models presented in this thesis the boundary conditions are set to be periodic on the left and right boundaries, no slip at the bottom and free slip condition is applied at the top of the box (Fig. 2.4). A free slip condition requires that the normal velocity component on the boundary is zero and the other components do not change across the boundary (this condition also implies zero shear strain rates and stresses along the boundary). Therefore, for the top boundary, the free slip condition is formulated as follows:

$$v_z = 0; \tag{2.29}$$

$$\frac{\partial v_x}{\partial z} = 0\,; \tag{2.30}$$

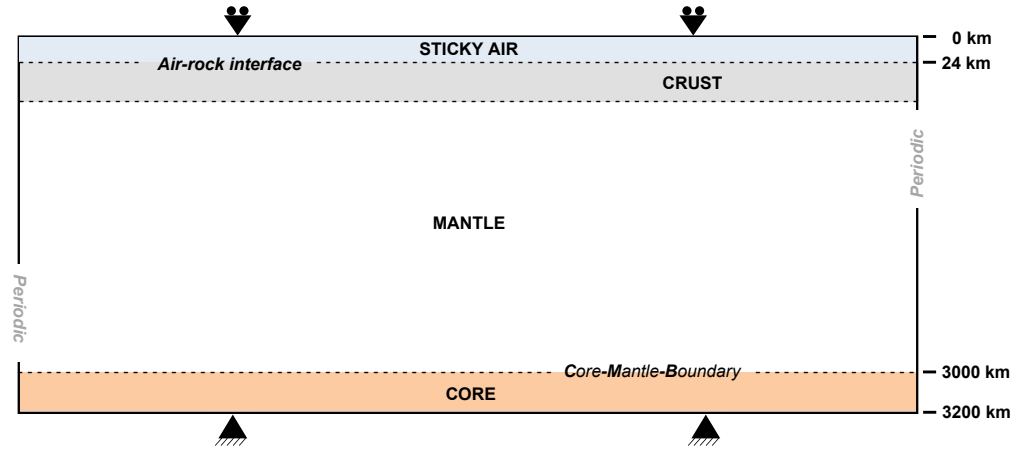

Figure 2.4: Schematic model setup used for standard 2-D experiments in Cartesian geometry.

Additionally, 25 km thick layer of *'sticky air'* (ρ_{air} = 1 kg/m^3, η_{air} = 10^{18} $Pa{\cdot}s$) was utilized in order to mimic the effect of a free surface and the development of topography (Crameri *et al.* , 2012). No slip condition at the bottom of the box requires that all velocity components on the boundary must be equal to zero:

$$v_z = v_x = 0\,; \tag{2.31}$$

Along this boundary, a 200 km thick low viscosity layer is placed at the bottom of the lower mantle to model the outer liquid core (ρ_{core} = 10000 kg/m^3, η_{core} = 10^{18} $Pa{\cdot}s$). Periodic boundary conditions are established on the vertical walls by discretizing the fundamental equations across the boundaries and by prescribing v_x and T unknowns on both sides of each boundary as identical. From a physical point of view, this implies that these two boundaries are open and that flow leaving the model through one boundary immediately re-enters through the opposite side. This condition is very useful in order to simulate the mantle convection of a cylindrical shell in Cartesian coordinates. The air/water-rock interface (Fig. 2.4) between the weak-air/water layer and the underly-

ing crust can be deformed due to erosion and sedimentation processes according to the transport equation (Gerya & Yuen, 2003):

$$\frac{\partial z_{es}}{\partial t} = v_z - v_x \frac{\partial z_{es}}{\partial x} - v_s + v_e \,; \tag{2.32}$$

where z_{es} is the vertical position of the surface as a function of the horizontal distance x. v_z and v_x are the vertical and horizontal components of the material velocity vector at the surface; v_s and v_e are imposed sedimentation and erosion rates, which correspond to the relation:

$$v_s = 0\frac{mm}{y};\ v_e = 0.3\frac{mm}{y};\ when\ z_{es} <\ 25km\,; \tag{2.33}$$

$$v_s = 0.03\frac{mm}{y};\ v_e = 0\frac{mm}{y};\ when\ z_{es} >\ 25km\,; \tag{2.34}$$

enhanced sedimentation rate (up to 1 mm/yr) is used in the trench area to preclude excessive steepening of the continental/arc slope.

2.4 Phase changes

Solid-state phase transitions are crucial phenomena in the Earth's mantle. The interaction of solid-solid phase transitions affects the dynamics of mantle convection due to (1) density changes and (2) latent heating (Schubert *et al.* , 1975). Phase changes are traditionally included in mantle convection models (e.g. Schubert *et al.* , 1975; Tackley *et al.* , 1993) by programming each transition individually. Major phase transitions include olivine-spinel at 410 km depth and spinel-perovskite at 660 km

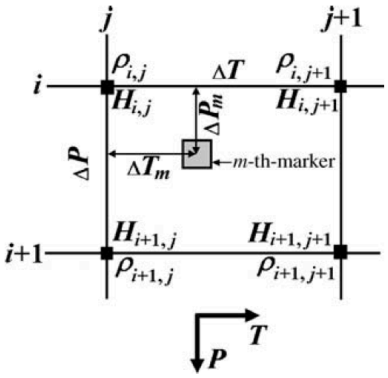

Figure 2.5: Stencil associated with the P-T grid used for the interpolation of physical properties from enthalpy and density look-up tables, to the markers. From Gerya (2010).

depth. These transitions are associated with significant changes in mantle density and seismic wave speeds (Turcotte & Schubert, 2002). However, for realistic mantle compositions, phase transitions involve several minerals of variable composition (so called solid solutions), which makes the traditional approach quite inconvenient. I2VIS uses a petrological - thermomechanical method relatively simple, which includes: (i) phase diagrams ($P-T$ pseudosections) and related density (ρ) and enthalpy (H) maps are first computed for the necessary rock compositions in a relevant range of $P-T$ conditions; (ii) these maps are then used in thermomechanical experiments for computing density (ρ), effective heat capacity incorporating latent heat (Cp_{eft}) and energetic effects (both adiabatic and latent heating) for isothermal (de)compression (H_p) on the material points (markers) based on standard thermodynamic formulas and numerical differentiation in $P-T$ space (Gerya 2010, Fig. 2.5):

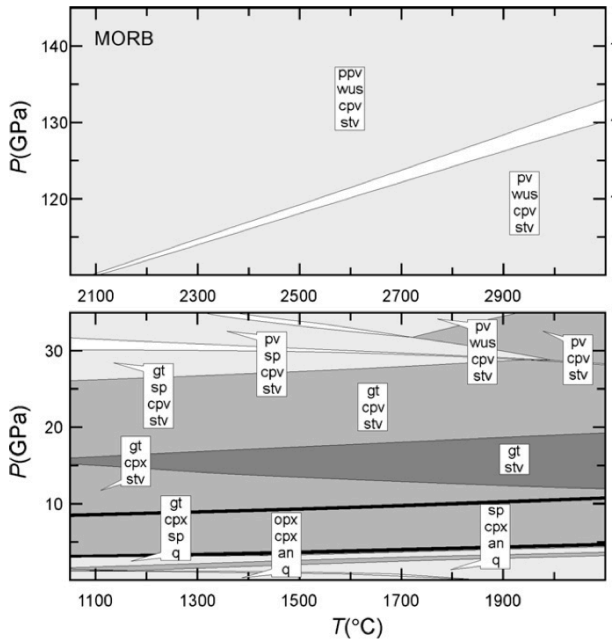

Figure 2.6: Phase relations for the CaO-FeO-MgO-Al_2O_3-SiO_2 pyrolite model computed (Mishin *et al.* , 2008) with the Gibbs free energy minimisation program PerpleX (Connolly, 2005). To permit the resolution of phase relations the diagram is split to exclude the large depth interval between the transition zone and Core-Mantle Boundary in which the model does not predict phase transformations. Composition for the pyrolite model is 3.87 wt % CaO, 8.11 wt % FeO, 3.61 wt % Al_2O_3, 38.59 wt % MgO and 45.82 wt % SiO_2.

$$\rho = \rho_{i,j}\left(1-\frac{\Delta T_m}{\Delta T}\right)\left(1-\frac{\Delta P_m}{\Delta P}\right)+\rho_{i+1,j}\left(1-\frac{\Delta T_m}{\Delta T}\right)\dots \\ \dots\frac{\Delta P_m}{\Delta P}+\rho_{i,j+1}\frac{\Delta T_m}{\Delta T}\left(1-\frac{\Delta P_m}{\Delta P}\right)+\rho_{i+1,j+1}\frac{\Delta T_m}{\Delta T}\frac{\Delta P_m}{\Delta P}\,; \tag{2.35}$$

$$Cp_{eff} = (\frac{dH}{dT})_{P=const.} = \frac{H_{i,j+1}-H_{i,j}}{\Delta T}(1-\frac{\Delta P_m}{\Delta_P})+\dots \\ \dots+\frac{H_{i+1,j+1}-H_{i+1,j}}{\Delta T}(\frac{\Delta P_m}{\Delta P})\,; \tag{2.36}$$

$$\frac{H_p}{DP/Dt} = (1-\rho\frac{dH}{dP})_{T=const.} = 1-\frac{H_{i+1,j}-H_{i,j}}{\Delta P}(1-\frac{\Delta T_m}{\Delta T})\dots \\ \dots\frac{\rho_{i+1,j}-\rho_{i,j}}{2}-\frac{H_{i+1,j+1}-H_{i,j+1}}{\Delta P}(\frac{\Delta T_m}{\Delta T})\frac{\rho_{i+1,j+1}-\rho_{i,j+1}}{2}\,; \tag{2.37}$$

In this way the conservation of energy equation is respectively modified as:

$$\rho Cp_{eff}\left(\frac{\partial T}{\partial t}\right) = -\frac{\partial q_i}{\partial x_i} + H_r + H_s + H_p\,; \tag{2.38}$$

The stable mineralogy and physical properties for the mantle with a pyrolitic composition are computed with PerpleX (Connolly, 2005) through a free energy minimisation approach (Fig. 2.6).

2.5 Computational strategy

The code structure should reflect the physical relations of momentum, continuity, temperature and advection equations (Gerya, 2010). The temperature equation requires values of adiabatic and shear heating that are computed from the velocity, pressure, stress and strain rate fields. Therefore, the temperature equation can only be solved after solving the momentum and continuity equations. On the other hand, the momentum and continuity equations have to be solved simultaneously to obtain values for velocity, that are present in both equations. The advection equation requires a velocity field and should thus also be solved after solving the momentum and continuity equations. The flow chart in Fig. 2.7 gives an example of a structure for a numerical, petro-thermo-mechanical viscous 2D code that uses finite-differences and the marker-in-cell technique (FD+MIC) to solve the momentum, continuity and temperature equations. The principal steps of the algorithm are as follows:

1. Calculating the scalar physical properties (η_m, ρ_m, Cpm, k_m, etc.) for each marker and interpolating these properties, as well as advected temperature from the markers to Eulerian nodes.

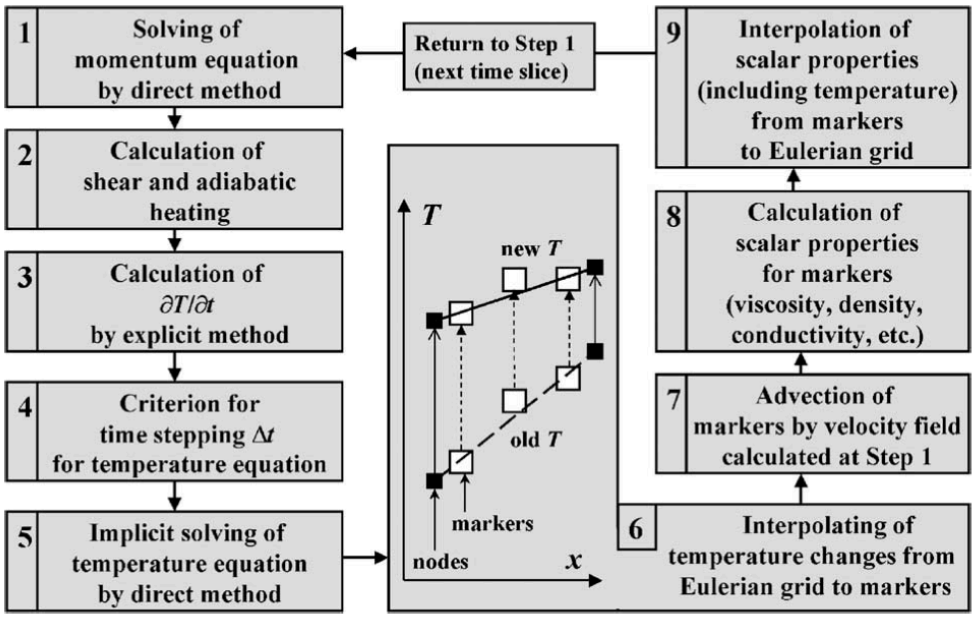

Figure 2.7: Flow chart representing the adopted computational strategy used in the programming of the computer code I2VIS. Panel for Step 6 shows the scheme for interpolating the calculated temperature changes from the Eulerian grid to the moving markers. From Gerya & Yuen, 2003.

2. Solving the 2D continuity and momentum equations with a pressure-velocity formulation on a staggered grid.

3. Defining an optimal displacement time step Δt_m for markers.

4. Calculating the shear and adiabatic heating terms $H_{s(i,j)}$ and $H_{a(i,j)}$ at the Eulerian nodes.

5. Defining an optimal time step Δt for the temperature equation.

6. Solving the temperature equation in a Lagrangian formulation, with implicit time stepping and a direct method.

7. Interpolating the calculated nodal temperature changes from the Eulerian nodes to the markers and calculating new marker temperatures (T_m) taking into account physical diffusion on subgrid

(marker) level.

8. Using a fourth-order explicit Runge-Kutta scheme in space to advect all markers throughout the mesh according to the globally calculated velocity field. Returning to Step 1 to perform the next time step.

Symbol	Meaning
A_D	pre-exponential factor - material constant ($MPa^{-n}s^{-1}$)
$A_{peierls}$	pre-exponential factor - material constant for Peierls creep ($Pa^{-2}\ s^{-1}$)
Cp	isobaric heat capacity ($J/kg/K$)
c	cohesion (Pa)
Ea	activation energy ($KJ\ mol^{-1}$)
g	gravitational acceleration ($m\ s^{-2}$)
H_r, H_a, H_s, H_l	radioactive, adiabatic, shear and latent heat (Wm^{-3})
H_P	adiabatic and latent heating for isothermal (de)compression (Wm^{-3})
H	enthalpy (J)
k	thermal conductivity ($KJ\ mol^{-1}$)
κ	thermal diffusivity ($m^2\ s^{-1}$)
n	stress exponent
P	dynamic pressure (Pa)
P_{fluid}	pore fluid pressure (Pa)
q_x, q_z	horizontal and vertical heat flux (Wm^{-2})
R	gas constant ($J\ mol^{-1}\ K^{-1}$)
t	time (s)
T	temperature ($°C\ or\ K$)
v_x, v_z	horizontal and vertical components of velocity ($m\ s^{-1}$)
v_e, v_s	erosion and sedimentation rates ($m\ s^{-1}$)
Va	activation volume ($J\ MPa^{-1}\ mol^{-1}$)
α	thermal expansion coefficient (K^{-1})
η	viscosity ($Pa \cdot s$)
η_{bulk}	bulk viscosity ($Pa \cdot s$)
λ_{fluid}	pore fluid pressure factor
μ	internal friction coefficient
ρ	material density (kg/m^3)
ε_{ij}	strain tensor
$\dot{\varepsilon_{ij}}$	strain rate tensor (s^{-1})
$\dot{\varepsilon}_{kk}$	bulk strain rate tensor (s^{-1})
$\dot{\varepsilon'}_{ij}$	deviatoric strain rate tensor (s^{-1})
$\dot{\varepsilon}_{II}$	second invariant of the deviatoric strain rate (s^{-1})
φ	internal friction angle (°)
σ_{ij}	stress tensor (Pa)
σ'_{ij}	deviatoric stress tensor (Pa)
σ_{II}	second invariant of the stress tensor (Pa)

Table 2.1: Abbreviations and units

Chapter 3

Continental break-up and drifting-simulations

A first-order characteristic of the solid Earth is the existence of plate tectonics, which exists on no other terrestrial planet in our solar system (Bercovici, 2003). Plate tectonics is a self-organizing global system driven by the negative buoyancy of the upper thermal boundary layer resulting in subduction. Continents slowly drift atop the mantle, sometimes colliding, splitting and aggregating. The evolution of the continent configuration, as well as oceanic plate tectonics, are one of the most important aspect of the solid Earth, closely linked to the flow of the mantle. During the last decades, significant progress has been made to recognize and quantify the forces acting on lithospheric plates (e.g. Forsyth & Uyeda, 1975; Melosh, 1977; Chapple & Tullis, 1977), or to demonstrate a dynamic feedback between the motion of sliding and/or subducting plates and mantle convection (e.g. Lux *et al.* , 1979; Gurnis, 1988). More recently, numerical modeling techniques have made great progress and the subduction processes have been widely studied (Gerya, 2011, for a

full review). Some of these numerical studies have focused on the mantle flow induced by subduction (e.g. Piromallo *et al.* , 2006), by analysing the toroidal vs. poloidal flow components as a function of boundary conditions. Although these studies well-explain how mantle flow can be induced by the descending lithosphere, numerous questions remain regarding the interaction among the induced mantle flow and an overriding continental lithosphere and if such mantle flow is sufficient to trigger the break-up and drifting of the continental plates.
In the present study we use 2-D numerical simulations with compositionally and rheologically -distinct plates floating at the top of the mantle in order to investigate how the mantle flow induced by subduction propagates under the plates, leading eventually to the break-up and drifting of the continental plates. For reference models, we have calculated shear stress, shear stress gradient and the amount of both active (F_{AD}) and passive (F_{PD}) mantle drag along the base of the continental lithosphere, together with the tension (T) generated within it. These data were then compared with the integrated strength (B) and the effective elastic thickness (Te) of the continental plates that were obtained from their yield strength envelopes. Numerical setup and methods are explained in the following section, while Table 3.4, summarizing the forces acting on the continental plate and calculated for the most important simulations, can be found at the end of this chapter.

The principal aspects of the dynamic between mantle convection and continents have been investigated and described through our models. Although few geophysical studies provide a quantitative framework that allows comparison with geological observations and detailed convection

characteristics, the numerical results obtained in this section will be compared with the evolution of some of the Earth's subduction settings in Chapter 5.

In summary, this chapter highlights a substantial relationship between the evolution of continents and their drift during subduction processes, by investigating how and to which extent the continental plates are affected by the mantle flow patterns, which are in turn controlled by descending lithosphere. We have generated a wide database of numerical simulations (>120), quantifying the acting forces and analysing the timescales and the deformation mechanisms of continental break-up and drifting induced by subduction.

3.1 Model setup

Our 2-D petrological-thermo-mechanical numerical model simulates the processes of spontaneous subduction of an oceanic plate beneath a continental plate in a 15000 km x 3200 km lithospheric-whole mantle section (Fig. 3.1-A). The oceanic plate is ~7500 km wide and converges dynamically (i.e., no convergence rate is applied) toward the continent with a velocity that depends on the various models tested (1 to 12 cm/yr for the reference model); the continental plate is ~6500 km wide. The rectangular staggered grid with 751 x 342 nodal points is non-uniform. Along the vertical direction, in the range between 0 km to 40 km grid resolution is 2 km, from 40 km to 90 km the resolution is 5 km and finally the grid spacing is fixed to 10 km till the bottom of the box; horizontal spacing is constant (20 km). The initial thermal structure of both the

oceanic plate and the continental plate are computed according to the semi-infinite half-space cooling model as follows (Turcotte & Schubert, 2002):

$$T = T_1 + (T_0 - T_1)\,(1 - erf(\beta))\,; \tag{3.1}$$

$$\beta = \frac{z}{2\sqrt{\kappa\tau}}\,; \tag{3.2}$$

where T_0 = 273 K and T_1 =1600 K, κ is the thermal diffusivity (10^{-6} m^2 s^{-1}), τ is the age in seconds of the plate and β is the dimensionless similarity variable. As the models do not reproduce dynamic active ridges were oceanic plates are generated, the age of the oceanic lithosphere is set to a constant value of 70 Myr. Starting then from the bottom of the lithosphere, an adiabatic gradient of 0.5 K/km is imposed.

The process of subduction initiation remains enigmatic and controversial, although it is widely accepted that the gravitational instability of old oceanic plates provides the primary driving force for subduction (Davies, 1999). In contrast to the gravitational instabilities that likely drive the subduction initiation process, the bending and shear resistance of the lithosphere acts against subduction initiation and in some cases may impede it altogether (McKenzie, 1977). For these reasons, the initial setup is characterized by a 200 km long slab simulating an incipient phase of oceanic plate subduction below a continent. Subduction is spontaneously driven by the negative buoyancy of this slab (Fig. 3.1-B). Additionally, there is a gap of 100 km thick between the oceanic and continental plates, filled by weak background crust with initial internal friction coefficient (μ_0) of 0.2, which is overlain by a prism of sediments.

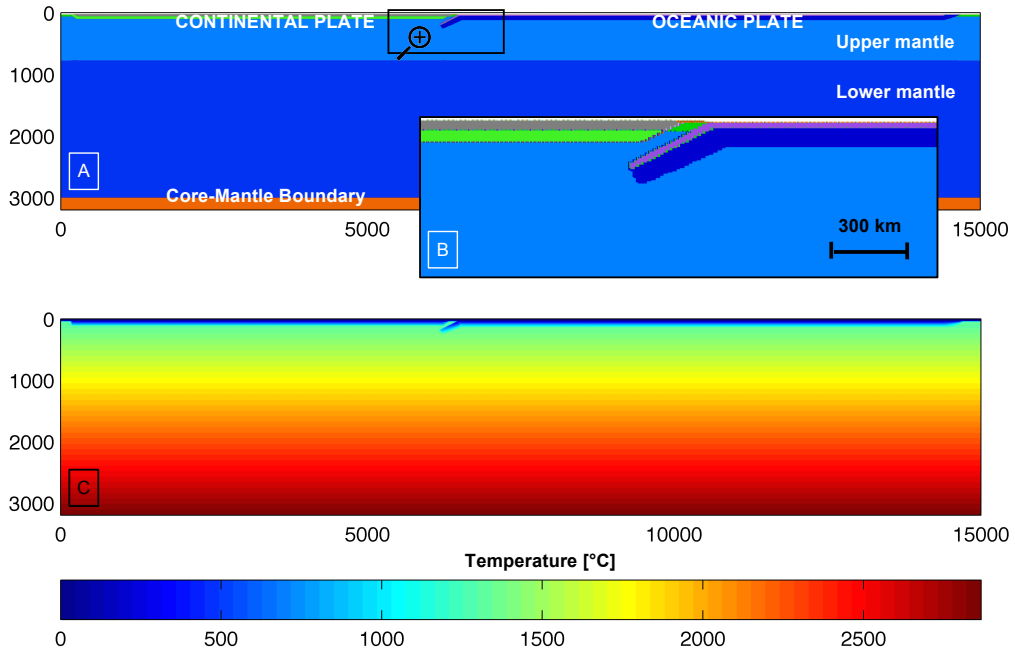

Figure 3.1: Initial configuration of the numerical model (see section 3.2 for details). Colours indicate materials (i.e. rock type, as explained on the table 3.1), which will appear even in subsequent compositional-map figures. Models with 15000 x 3200 Cartesian domain, staggered grid resolution (751 x 342 nodes) and more than 8 million of randomly distributed particles. Figure 3.1-B shows in details the initial geometry around the trench area, while the Figure 3.1-C plots the initial temperature distribution.

Such initial geometry is needed to stimulate the initiation of dynamic subduction.

We began our study with a reference model that reproduces the stable one-sided subduction typical of modern subduction (Gerya *et al.* , 2008) using the following parameters: the continental plate is 76 km thick, with 32 km of crust and 44 km of lithospheric mantle; the oceanic plate is 90 km thick, with 20 km of oceanic crust and 70 km of lithospheric mantle.

Based on this initial model we performed more than 40 numerical ex-

Colour	Rock type	Composition
	Air	
	Water	
	Felsic crust	Wet-quartzite
	Continental lithospheric mantle	Dry-olivine
	Oceanic crust	Wet-basalt
	Oceanic lithospheric mantle	Dry-olivine
	Upper mantle	Dry-olivine
	Lower mantle	Dry-olivine
	Outer core	

Table 3.1: Rock types used for numerical simulations. Composition refers to the flow laws used to model the non-linear viscous behaviour and are taken from Ranalli (1995).

periments, by varying independently:

1. Cartesian domain of the model;
2. Age (β) of the oceanic plate;
3. Viscosity (η) of upper and lower mantle;
4. Thickness of the weak zone between continental and oceanic plates;

5. Yield strength (σ_{yield}) and thickness of the continental plate;

Further numerical simulations tested will be individually taken into account in section 3.4.

Initial models are performed with a domain of 10000 x 2200 km along x and z direction, respectively, and with same initial setup (thickness of the plates, temperature gradient, etc.). After about ten tests, we have preferred to extend the domain (15000 x 3200 km) in order to:

1. avoid interferences of the mantle flow along the periodic boundaries with the subduction dynamics;

2. reproduces the entire and more realistic section of the mantle;

During these first simulations, we have changed also the age of the oceanic plate in a range between 70 Myr and 150 Myr. Although the stiffness and, thus, the dynamic behaviour of the subducting plate may change with time, we have preferred to assume a constant age of the oceanic plate, equal to 70 Myr, that is more representative of the average oceanic lithosphere age.
In order to better control the stresses propagating from the upper mantle to the overlying continental plate, we have initially used constant mantle viscosities. Unfortunately the knowledge of the viscosity of the Earth's mantle still remains elusive and therefore most of the initial numerical simulations have been run to calibrate the viscosity of the upper mantle in order to have realistic sinking velocity of the oceanic plate. From these tests we chose an upper mantle viscosity of $\eta_{UM} = 3 \cdot 10^{20}$ $Pa \cdot s$, that is consistent with the viscosity estimated for the upper man-

tle below cold continents (Carter & Tsenn, 1987), while a different set of constant viscosities of the lower mantle was used to reproduce different subduction styles. For the oceanic and continental lithosphere we have used flow laws taken from Ranalli (1995).

Numerical experiments conducted by Gerya *et al.* (2008) show that the stability, intensity, and mode of subduction depend mainly on slab strength and the amount of weak hydrated rocks present above the slab. Additionally, 2D numerical experiments developed by Faccenda *et al.* (2009) have showed that stress changes induced by the bending oceanic plate produce sub-hydrostatic or even negative pressure gradients along normal faults, favouring downward pumping of fluids. Taking into account these results and given that significant hydration of the oceanic crust occurs at mid-ocean ridges in response to the high porosity and permeability, a hydrated oceanic crust is modelled by setting the pore fluid pressure factor λ_{fluid} = 0.20 to 0.30. Another important assumption of our models is given by oceanic crust thickness, equal to 20 km due to relative low vertical resolution and therefore necessary to ensure a correct functionality of the lubricating layer atop the slab. Finally, the initial gap width and/or the insertion of a thin weak-layer among the plates were also tested in order to investigate which initial setup better enhances the incipient phase of subduction.

Given that our first aim is to study the continental break-up, our numerical investigation starts with a relative thin and weak continental plate (i.e. 76 km). Subsequently, more realistic models characterized by a gradually thicker and, thus, stiffer overriding plates were tested.

Table 3.2 recaps all of these input parameters.

Material	Thickness, [km]	ρ_0, [kg/m^3]	λ_{fluid}, -	σ_{yield}, [Pa]	age, [Myr]	H_r, [Wm^{-3}]	E, [kJ/mol]	n, -	V, [J/(bar)]	A_D, [$Pa\ s$]	C [MPa]	μ_0, μ_1	$\varepsilon_0, \varepsilon_1$	Flow -law *
Background crust	30	2900	1	-	-	$0.25{\cdot}10^{-6}$	154	2.3	1.2	$1.97{\cdot}10^{17}$	1	0.2, 0.1	0.0, 0.5	Plg-An75
Continent plate				($5{\cdot}10^7$;	70									
- crust	32	2750	1	$2{\cdot}10^9$)		$1.0{\cdot}10^{-6}$	154	2.3	0.8	$1.97{\cdot}10^{17}$	1	0.2, 0.1	0.0, 0.05	Wet-Qtz
- lithosphere	44	3300	1			$2.2{\cdot}10^{-8}$	532	3.5	1.2	$3.98{\cdot}10^{16}$	1	0.2, 0.1	0.0, 0.05	Dry-Ol
Oceanic plate				-	70									
- crust	20	3000	(0.2,0.3)			$0.25{\cdot}10^{-6}$	154	2.3	1.2	$1.97{\cdot}10^{17}$	1	0.1, 0.05	0.0, 0.5	Wet-Qtz
- lithosphere	70	3300	1			$2.2{\cdot}10^{-8}$	532	3.5	1.2	$3.98{\cdot}10^{16}$	1	0.6, 0.4	0.5, 1.5	Dry-Ol
Upper mantle	(584;570)	3300	1	-	-	$2.2{\cdot}10^{-8}$	154	3.5	(1.0; -1.2)	$3.98{\cdot}10^{16}$	1	0.6, 0.4	0.5, 1.5	Dry-Ol
Lower mantle	2340	4000	1	-	-	$2.2{\cdot}10^{-8}$	532	3.5	1.2	$3.98{\cdot}10^{16}$	1	0.6, 0.4	0.5, 1.5	Dry-Ol
Outer core	200	10000	1	-	-	-	470	3,5	1.2	$5.01{\cdot}10^{20}$	1	0.0, 0.0	-	Wet-Ol

* Flow law parameters are from Ranalli (1995).

Table 3.2: Parameters used in this study.

3.2 Acting forces, yield strength envelopes and effective elastic thickness

Through the shear stress maps obtained for each timestep, it has been possible to describe the time-evolution the horizontal shear stress at the base of the overriding plate. Such shear stresses are proportional to the upper mantle viscosity and to the velocity gradient along the vertical direction. Below the horizontal continental plate the shear stress are roughly equal to:

$$\sigma_{xy} \approx \eta \frac{1}{2} \frac{\partial vx}{\partial y} ; \tag{3.3}$$

Hence, a fast and viscous upper mantle flowing beneath a relatively stable plate produces high tractions.

The base of the lithosphere has been identified as where the viscosity on the basic Eulerian nodes is approaching that of the upper mantle (i.e. $\eta_{UM} = 3 \cdot 10^{20}\ Pa \cdot s$). Then we have applied a smoothing to the shear stresses profile along this level in order to remove small-scale shear stress oscillations due to depth variations of the base of the lithosphere associated with the initial random marker distribution. Successively, the horizontal gradient of the shear stress was calculated as follows:

$$\frac{\partial \sigma_{xy}}{\partial x} ; \tag{3.4}$$

Subsequently, passive (F_{PD}) and active (F_{AD}) mantle drag were quantified by integrating the shear stress along the base of the continental plate as:

$$F_{PD} = \int_A^B \sigma_{xy} \, \partial x ; \tag{3.5}$$

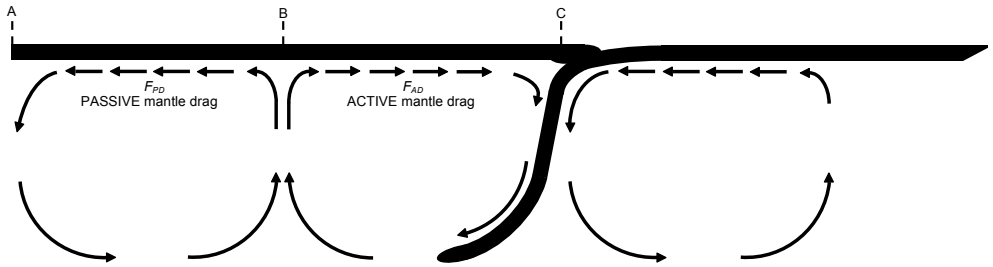

Figure 3.2: Sketch of a generic subduction process that develops both passive and active mantle drag. As the arrows describe, these two forces act with opposite direction. Points A, B and C delimited the finite-length of action of the passive and active mantle drag.

$$F_{AD} = \int_B^C \sigma_{xy}\, \partial x\,; \tag{3.6}$$

where A-B and B-C delimit the finite-length in which active or passive drag acts (Fig. 3.2). With respect to the chosen model geometry, active mantle drag favours continental drift toward the right, and is counteracted by the passive drag force opposite in direction. According to the action-reaction principle (or Newton's third law), tension (T) develops within the continental plate with a magnitude equal to $min(F_{PD}, F_{AD})$, while the difference between active and passive mantle drag determines the direction of plate drifting.

Another important force affecting continental plate break-up and drifting is the trench suction force (F_{TS}). When the slab retreats, the upper plate, if coupled with the lower one, is forced to 'flow' in the same direction because mass continuity does not allow formation of voids. As a result, extensional stresses are generated through the upper plate. Obviously, when the trench is advancing, the upper plate will be in compression. F_{TS} is difficult to be quantified but, as we will see later, it is crucial for the evolution of some models.

In order to calculate the yield strength envelope as well as the total strength of the continental plate, an additional one-dimensional code (i.e. YSE_1D-code) was written in MatLab. Firstly, a 1-D temperature profile for the computation of the differential stress profile is given by the half-space cooling model (cf. eq. 3.1), which provides the initial temperature distribution. The 1-D pressure profile was determined assuming lithostatic conditions. Using the P-T profiles, a one-dimensional strength profile through the continental lithosphere was built. It shows the yield stress, which is the stress above which the rock deforms at a given depth. The plate visco-plastic behaviour is considered by taking the minimum yield stress defined either by the Drucker-Prager/von Mises yield-criteria (cf. eq. 2.23 and 2.24), or by three flow laws that account for diffusion creep:

$$\sigma_d = \frac{A}{\sigma_{ss}^{n-1}} \cdot \dot{\varepsilon}' \cdot exp\left(\frac{E_a + P\,V_a}{RT}\right) ; \tag{3.7}$$

dislocation creep:

$$\sigma_d = \frac{1}{A} \cdot \dot{\varepsilon}' \cdot exp\left(\frac{E_a + P\,V_a}{RT}\right)^{\frac{1}{n}} ; \tag{3.8}$$

and Peierls creep:

$$\sigma_d = 1 - \left(\frac{-R\,T}{E_a + P\,V_a} \cdot log\left(\frac{\dot{\varepsilon}'}{A_p\,(\sigma_d)^2}\right)\right)^{0.5} \cdot \sigma_0 \tag{3.9}$$

where σ_{ss} (= $3 \cdot 10^4$ Pa) is transitional stress, σ_1 (= 10 MPa) the initial stress, σ_0 (= 9.1 GPa) the necessary stress to break one crystal of dry-olivine at zero kelvin, while $\dot{\varepsilon}'$ (= $1 \cdot 10^{-14}$ s^{-1}) is the default strain rate.

For Peierls creep, σ_d must be found by interaction.
Afterwards, the amount of continental strength (i.e. integrated strength, B) is computed as follows:

$$B = \int_0^{Y_L} \sigma_d \, \partial z \, ; \tag{3.10}$$

where Y_L is the thickness of the lithosphere. Given that the coefficient of friction is a function of the strain ($\mu = f(\varepsilon)$), we have computed both initial and final strength-envelopes. By comparing the integrated strength (B) to the tension (T) generated within the continent and given by the minimum value among active and passive mantle drag, we can understand if such tension overcomes the plate strength or if additional forces are needed to trigger the continental break-up.
It is well accepted that the lithosphere exhibits a finite mechanical strength over geological time and space scales, resisting non-lithostatic (deviatoric) stresses. The parameter that characterizes the apparent strength of the lithosphere is the flexural rigidity D, which is commonly expressed through the effective elastic thickness (Te) of the lithosphere. Estimates of Te for oceanic lithosphere approximately follow the depth to a specific isotherm (similar to 600 degrees $^{\circ}C$), which marks the base of the mechanical lithosphere (Burov & Diament, 1995). The physical meaning and significance of the effective elastic thickness for continents are still enigmatic, because for continental lithosphere estimates of Te bear little relation to specific geological or physical boundaries. Although high-observed values of Te (70-90 km for cratons) can be partly explained by the present-day temperature gradients, the low values (10-20 km), in general, cannot. As such, we are interested not only in the composition and distribution of these weak areas, but also on how they respond to

hypothetical loading. Since the Earth's layers near the surface may be approximated as plates, this suggests the definition of an effective elastic thickness as the depth of lithosphere over which the response can be compared to the deformation of a plate under load.

We estimate elastic thickness (*Te*) based directly on the estimated depth-distribution of strength. From the YSE_1D-code, it is possible to define the mechanical thickness of each competent layer as where the yield stress is greater than some pre-defined value (e.g. 10 MPa used in Ranalli, 1994). Therefore, the lithospheric layers are considered decoupled when the strength decreases below this threshold, or welded otherwise. Then, according to Cloetingh & Burov, 1996, when the lithosphere consists of n competent layers decoupled from each other, *Te* is defined as follows (see also Burov & Diament, 1995):

$$T_e^{(n)} = \left(\sum_{i=1}^{n} \Delta\, h_i^3 \right)^{1/3} ; \tag{3.11}$$

where Δh_i is the thickness of the i_{th} competent layer (i.e. crust and lithospheric mantle). Alternatively, if the layers are mechanically coupled, the upper limit of *Te* is estimated as total thickness of the competent layers:

$$T_e^{(n)} = \left(\sum_{i=1}^{n} \Delta\, h_i \right) ; \tag{3.12}$$

Summarizing, **YSE_1D** code is able to output the lithospheric yield strength profile, the integrated strength and the effective elastic thickness by using the same thermal structure and rheological parameters as in the $I2VIS$ simulations.

The 1-D MatLab code **YSE_1D** can be found in the Appendix A.

3.3 Results

Subduction starts spontaneously due to negative buoyancy of the slab, being driven solely by the gravity force. During this first phase, the gap between the two plates progressively is consumed by erosion of the intra-plate material and by the drifting of the continent toward the trench (owing to active mantle drag and trench suction forces), thereby leading to an increase of the plates coupling. Simultaneously, slab-dip grows as a result of the dual effect given by slab pull and friction between the two plates that produces a resistance to sliding. In most of our simulations, the initial sinking of the oceanic lithosphere is accompanied by trench retreat. The viscous mantle drag at bottom of the horizontal portion of the oceanic lithosphere impedes plate advance, promoting trench retreat. When the slab encounters the 660 km discontinuity, different modes of subduction occur as a function of the viscosity contrast between the upper and lower mantle. While maintaining constant the upper mantle viscosity ($\eta_{UM} = 3 \cdot 10^{20}\ Pa \cdot s$), we have progressively increased the viscosity of lower mantle. The first observation is that, as the viscosity contrast increases, three main subduction styles can be defined:

1. **Penetrating slab**, when the slab sinks into the lower mantle;
2. **Slab avalanche**, where the slab penetrates after an initial stagnation over the 660 km discontinuity;
3. **Stagnant slab**, which occurs if the slab lies above the 660 km discontinuity.

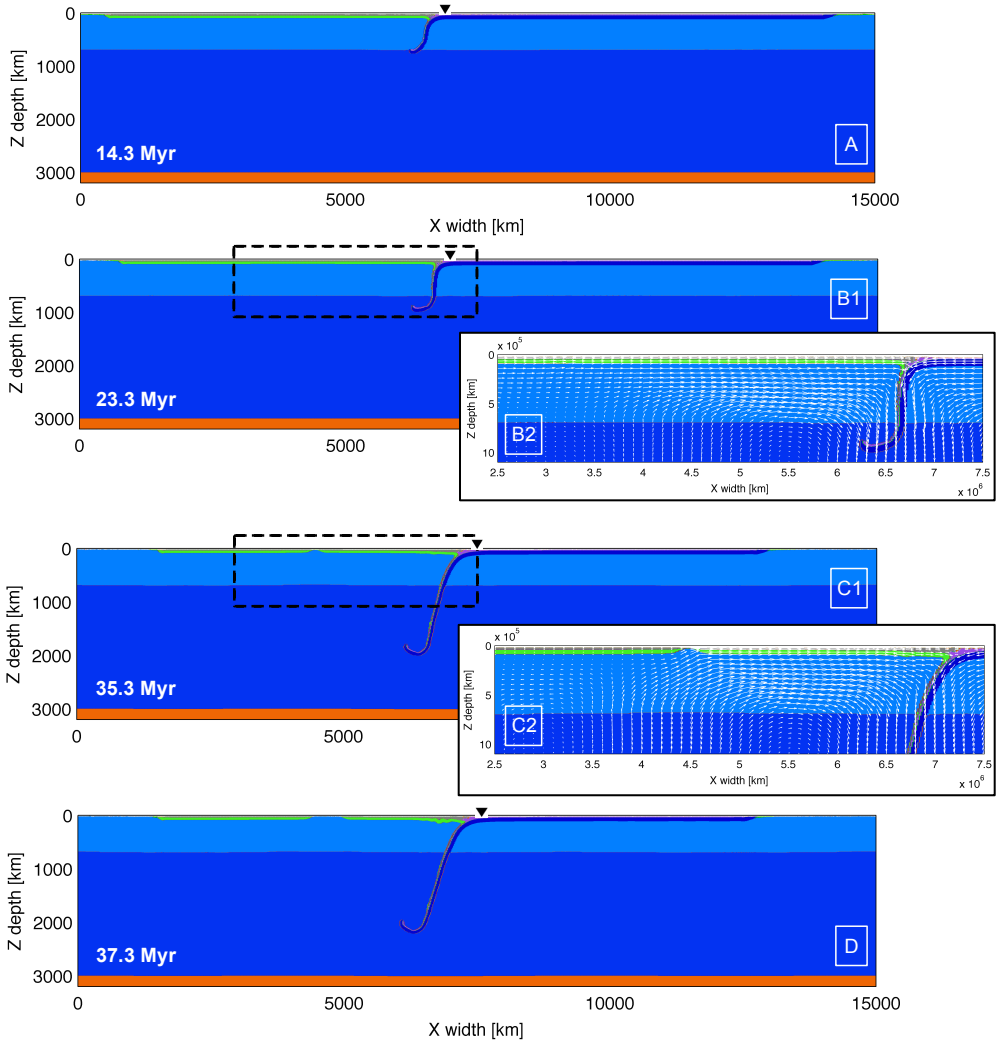

Figure 3.3: Snapshots of the reference model with penetrating slab. [A] Slab bends at upper-lower mantle transition, due to resistance to penetration into the lower mantle. [B1] After penetration, slab vertically moves downward and trench retreat increases. [B2] Compositional map with velocity field superimposed shows how whole-mantle convective system is activated. [C1] Mantle flow induced by descending lithosphere drives the break-up of the continent. [C2] Shown in detail the divergent flow and the break-up point. [D] After break-up, right part of the continent strongly coupled with subducting plate follows the backwards motion of the trench, triggering the drifting-phase. Solid triangles show trench position.

3.3.1 Penetrating slab

Our models assume that the age as well as the thermal structure of the oceanic plate is constant, although viscosity of the lower mantle pro-

gressively increases in the various simulations. Within a range of the viscosity contrast from 1 to 50, a penetrating slab style of subduction establishes showing the same non-steady-state evolution, although with different velocity of convergence (i.e. velocity of subduction decreases as the viscosity contrast increases). The first observation is that, when the oceanic lithosphere penetrates into the lower mantle, whole mantle convection is activated, while maintaining an aspect ratio (width/height) of ~1 (Fig. 3.4-B1-B2). The slab sinking velocity progressively increases, aiding to more vigorous mantle convection. Under this condition, poloidal mantle flow moves upward and diverges when reaches the base of the continental plate; details of the divergent flow may be observed in the (Fig. 3.3-B2). The induced mantle flow moves horizontally toward the trench producing active mantle drag (acting roughly below the right half of the continent) and drifting of the entire plate toward the trench. Drifting is resisted by passive mantle drag acting on the left half of the continent, thus partially counterbalancing the active mantle viscous drag. As a result, tension (T) is generated within the continental plate. Because continental drift is toward the trench, $F_{AD} > F_{PD}$ and tension (T) is equal to F_{PD}. From this moment, a steady-state deformation regime establishes, till the break-up of the continent. When break-up occurs (Fig. 3.3-C2), the velocity of convergence of the oceanic plate is equal to ~10 cm/yr and the plate portion along the trench-side continues to drift in the direction of trench retreat, while the horizontal velocity of the continent on the left of the break-up point sharply decreases to zero. (Fig. 3.3-D). From the beginning of the experiments, the oceanic plate is underthrusted under the continental plate, which is also dragged toward the trench by the flow in the underlying upper mantle, altogether

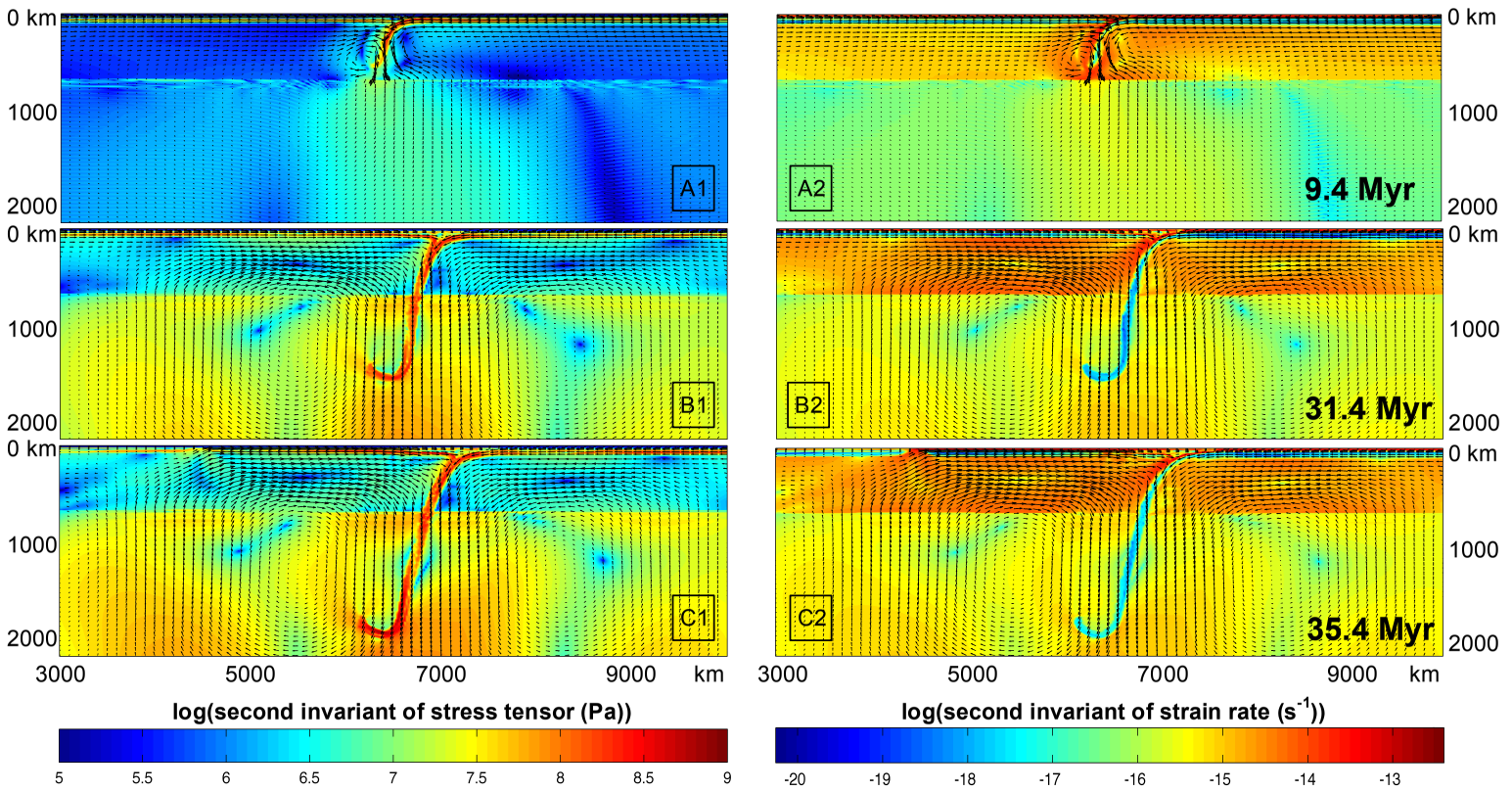

Figure 3.4: Evolution of the reference numerical experiment of penetrating slab. Left column shows the second invariant of deviatoric stress tensor and right column the second invariant of strain rate, both on a logarithmic scale. [A1; A2] Incipient stage of subduction: subducting slab develops a narrow poloidal flow confined in the upper mantle. [B1; B2] Penetrating slab activates whole-mantle convective system and slab-dip progressively becomes vertical. [C1; C3] Break-up phase: active mantle drag of the poloidal flow triggers the break-up of continental plate.

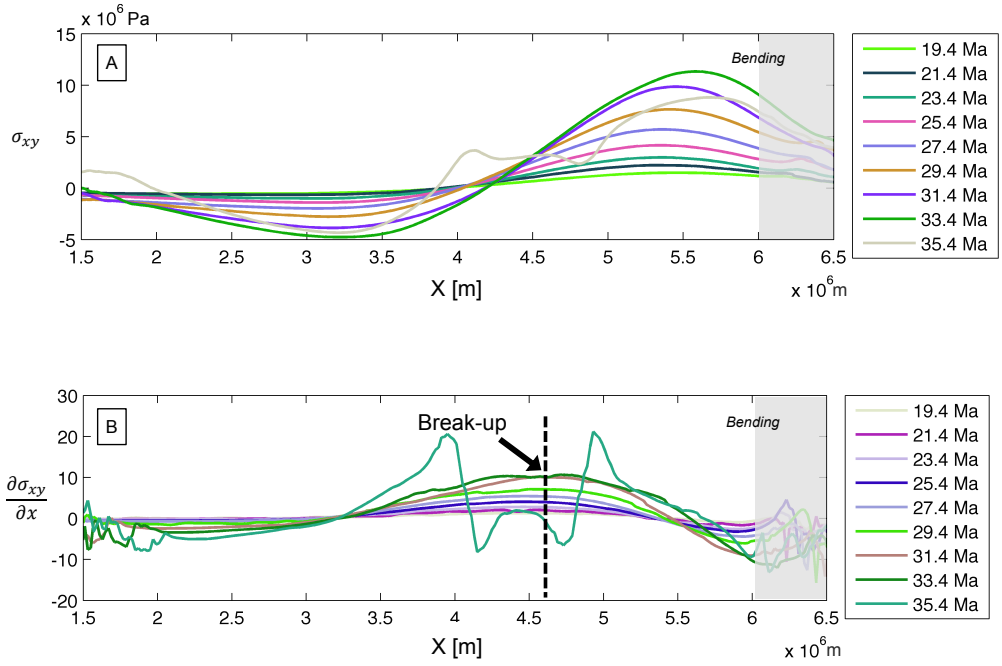

Figure 3.5: Profiles of shear stress [A] and shear stress gradient [B]. These profiles were obtained during the simulation of a penetrating slab subduction style along the base of the continental lithosphere and show the most important timesteps.

producing buckling of the overriding plate; details of the continental buckling may be observed in the (Fig. 3.3-D). The dynamic evolution of the reference model can be also examined through the Figure 3.4, which shows on a logarithmic scale both the second invariant of the deviatoric stress and the second invariant of the strain rate. It is worth to note that maximum strain rate values are reached within the upper mantle layer, which corresponds to lower viscosity and stress values. In addition, the same convective cell developing under the overriding plate can be found also under the oceanic plate, thus forming a quasi-symmetric flow pattern.

The reference model of penetrating slab was also used to measure the shear stress profiles at different timestep, in order to observe how trac-

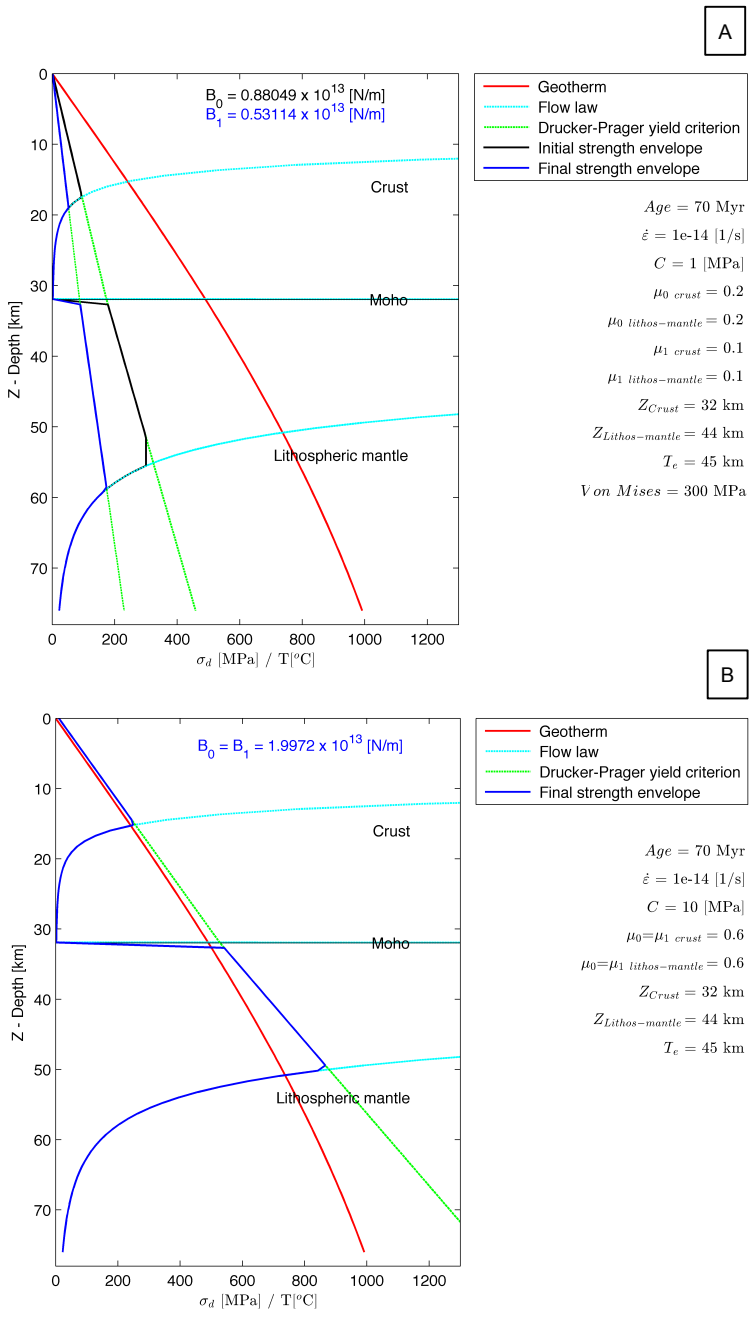

Figure 3.6: 'Christmas trees' yield envelopes. [A] Reference model shows two yield strength envelopes, which are function of different coefficients of friction (μ_0 (black line) and μ_1 (blue line)), while [B] describes a stiffer continental plate (i.e. without Von Mises yield criterion, $C = 10$ MPa and $\mu_0 = \mu_1 = 0.6$). Each figure shows the geotherm profile (red), flow laws (light blue) and the Drucker-Prager yield criterion (green). B_0 and B_1 are the initial and final integrated strength, respectively, Te - effective elastic thickness and $\dot{\varepsilon}'$ is the default strain rate.

tion evolves with time along the bottom surface of the continental plate in the range between 1500 km and 6500 km (Fig. 3.5). The first observation is that the absolute value of the shear stress increases progressively in two opposite directions and takes a value equal to zero at ~4200 km (Fig. 3.5-A), corresponding to the area where mantle flow is diverging. As shear stress increases, the profile curves become more asymmetric because the positive shear stresses on the right side of the profiles (i.e. F_{AD} - active mantle drag) increases more than the negative shear stresses on left side of the profiles (i.e. F_{PD} - passive mantle drag), reaching an absolute shear stress peak of ~12 MPa between 29 Myr and 35 Myr. Such increments are associated with the increase of the sinking velocity. If instead we take the shear stress gradient profiles (Fig. 3.5-B), we can observe a similar evolution but with some peculiar differences. The shear stress gradient assumes a value equal to zero at ~3200 km and ~5500 km, which obviously corresponds to the minimum and maximum values of the shear stress. On the other hand, the maximum value of the shear stress gradient is at ~4600 km (Fig. 3.5-B dashed line), where the shear stress curves have their inflection point. The most important thing about this is that, when sufficient tension (T) is available to overcome the continent strength, break-up occurs in correspondence of the maximum value of the shear stress gradient (Fig. 3.5-B), and not where the absolute value of shear stress is reached. In other words, the break-up occurs in correspondence of the maximum variation of the horizontal shear stress. On the contrary, a uniform distribution of the shear stress would produce homogeneous (i.e., not localized) deformation. We suggest that the asymmetric curves may explain the entire movement of the continental plate before the break-up, because active mantle drag (F_{AD}) along the

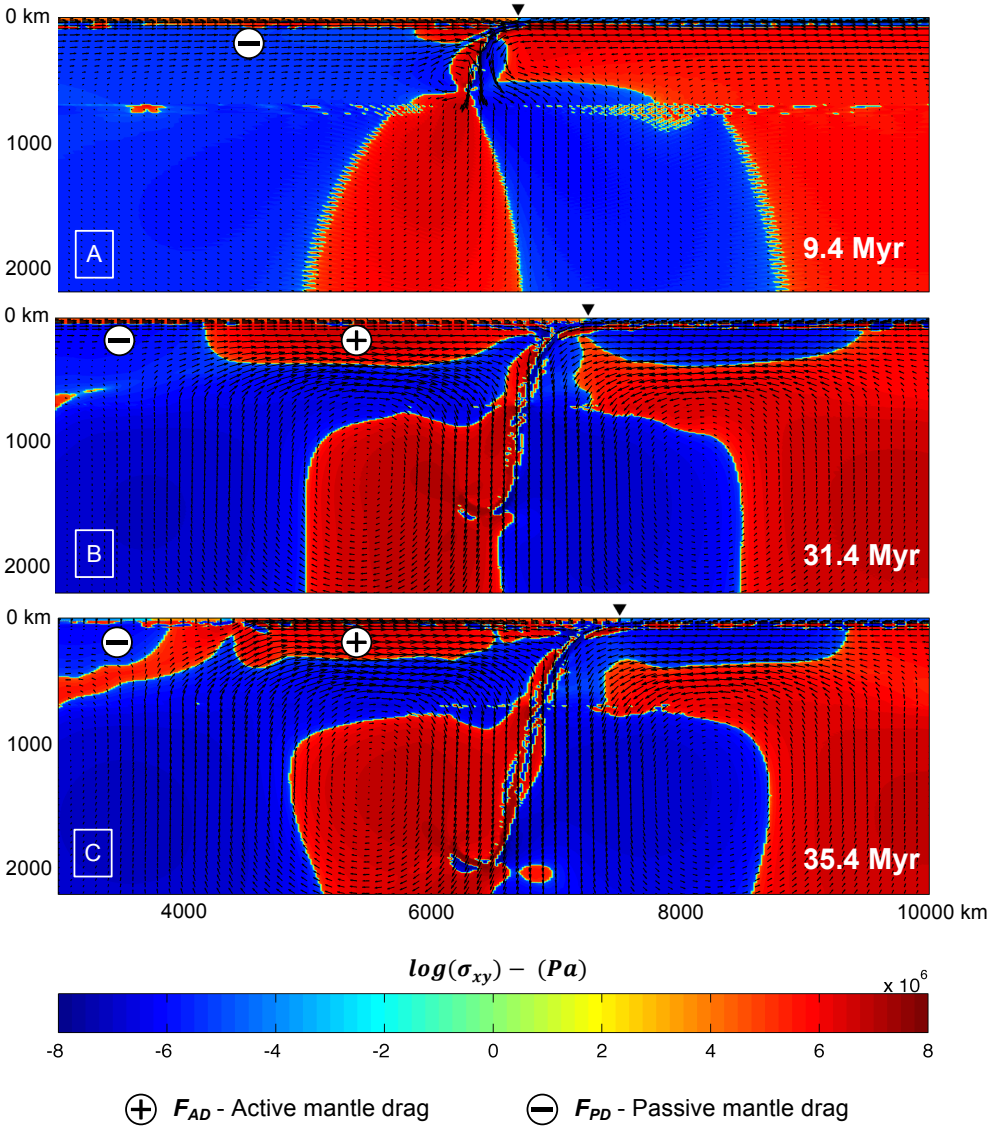

Figure 3.7: Map of the shear stress distribution with superimposed the velocity field of the reference model. The snapshots show typical dynamic of the penetrating subduction model that produces below the upper plate an active mantle drag (+) counterbalanced by passive viscous drag (−) of the mantle. Solid triangles show trench position.

trench-side overcomes passive mantle drag (F_{PD}) and the differences between these two forces may promote the entire movement toward right, coupled with trench retreat. Indeed, we have obtained an active mantle drag F_{AD} = 1,74 $\cdot$ 10^{13} N/m and a corresponding passive mantle drag F_{PD} = 0,75 $\cdot$ 10^{13} N/m. Therefore, the tension within the plate is T = 0,75 $\cdot$ 10^{13} N/m, which produces an average stress through the 76 km thick continent of about 100 MPa. The final integrated strength of the continent obtained from the yield strength envelope (Fig. 3.6-A) is B_1 = 0,53 $\cdot$ 10^{13} N/m, i.e., it is lower than the plate internal tension, explaining why the break-up occurs (cf. Table 3.4 - Test 044). Worthy of note is another test with the same geometry as the reference model but with a stiffer continental plate (Fig. 3.6-B). In this case the break-up occurs anyway, although the internal tension (T = 1,46 $\cdot$ 10^{13} N/m) is smaller than the plate integrated strength B_1 = 1,99 $\cdot$ 10^{13} N/m. Therefore, we suggest that, in addition to mantle drag forces, trench suction forces F_{TS} of at least 0.53 $\cdot$ 10^{13} N/m and due to trench retreat produce significant tension within the upper plate, aiding the continental break-up process (cf. Table 3.4 - Test 118).

Figure 3.7 shows three fundamental snapshots of the shear stress map with superimposed the velocity field of the penetrating slab reference model. Figure 3.7-A describes the initial-phase of subduction, in which the slab has not yet reached the 660 km discontinuity and the induced mantle flow is confined on the upper mantle layer. Beneath the overriding plate and except near the trench, the upper mantle resists flow induced by the overlain drifting continent (– sign). Whole mantle convective is then activated (Fig. 3.7-B) by the descending lithosphere into the lower mantle and a wide lens of active mantle drag (+ sign) develops.

At this stage, equilibrium of forces is maintained as long as break-up occurs (Fig. 3.7-C). It is worth to note that a quasi-symmetric structure is also reproduced under the oceanic plate.

3.3.2 Slab avalanche

Following the same approach adopted for the penetration slab models, we have tested a series of numerical simulations progressively increasing the lower mantle viscosity (η_{LM}). The main difference with respect to penetrating slab models is given by time during which slab stagnation occurs, that strictly depends on viscosity contrast (if we assume the same thermal structure).

The snapshots of the Figure 3.8 are relate to a reference model of slab avalanche with viscosity contrast of 150, in which the upper mantle viscosity is equal to $3 \cdot 10^{20}\ Pa \cdot s$ and that of the lower mantle is increased to $= 4.5 \cdot 10^{22}\ Pa \cdot s$ (150 x η_{UM}). Initially, subduction starts spontaneously and the slab sinks vertically downward until it encounters the 660 km discontinuity (Fig. 3.8-A1). In the range between 3 Myr and 14 Myr, velocity field of the subducting plate sharply increases due to the downward movement of the slab, which induces a mantle flow limited to upper mantle. The resistance to penetration at the upper-lower mantle boundary causes the bending of the slab that flattens along the boundary. From this moment, slab retreat increases, with the slab dip being sub-vertical through the upper mantle and with the ~500 km long slab-tip that is flattened and well supported along the discontinuity (Fig. 3.8-B). Before the slab avalanche, a transitional condition of stagnation is maintained by the slab above the 660 km discontinuity and with variable interval time that in our models is typically between 6 Myr and 12 Myr.

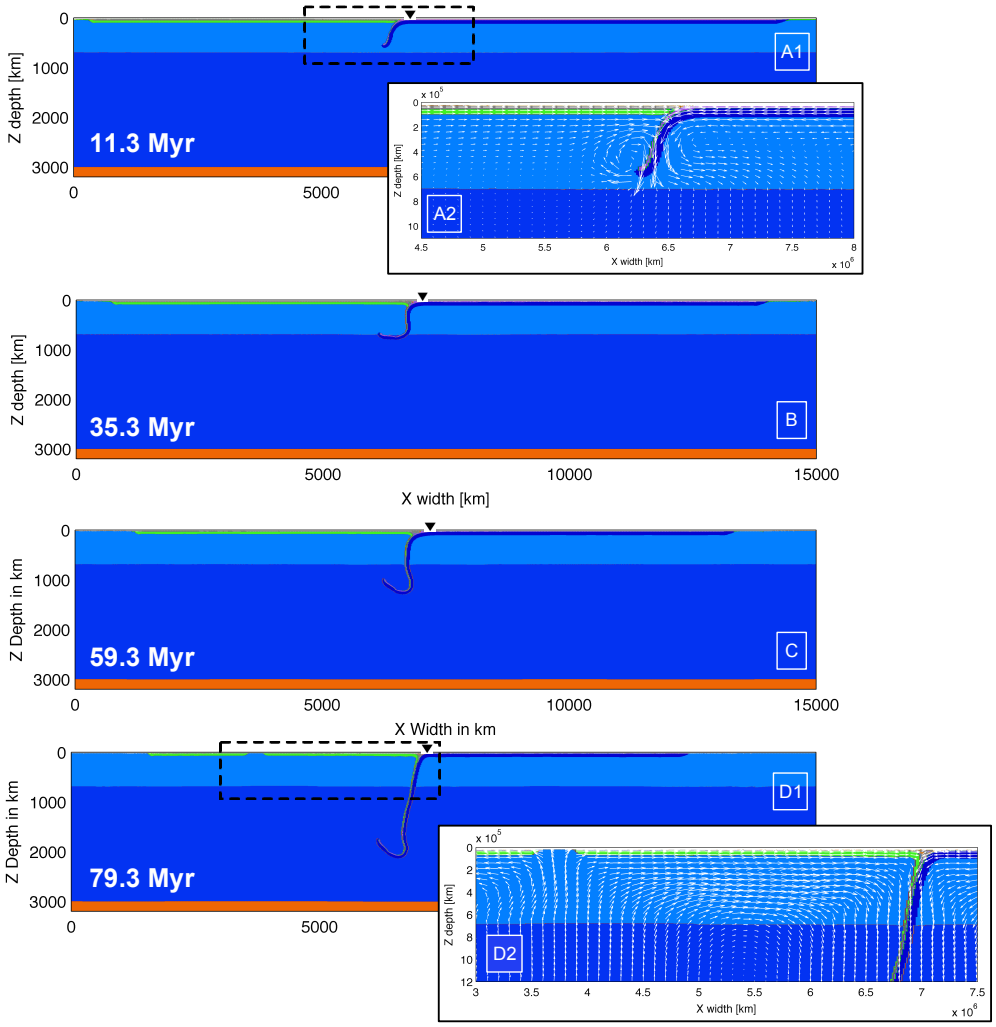

Figure 3.8: Snapshots of the reference model of slab avalanche. The subduction has a dynamic comparable with penetrating slab, although differ on stagnation time above lower mantle. [A1] Slab sinks into the upper mantle. [A2] Velocity field superimposed on compositional map shows the initial narrow convective cell. [B] Slab bends due to resistance to penetration. [C] Slab falls down through the lower mantle. [D1] Mantle flow induced by descending lithosphere produces the continental break-up. [D2] After break-up, continental plate portion near the trench follows the trench retreat under the mantle flow traction. Solid triangles show trench position.

On the one hand, with subduction the slab negative buoyancy progressively increases, favouring penetration. Additionally, during stagnation the flat slab progressively warms up so that decomposition of the spinel

into perovskite and magnesiowüstite can occur. These two processes altogether lead to the collapse of the slab into the lower mantle (Fig. 3.8-C). Slab avalanche is then accompanied by significant amount of underthrusting of the oceanic plate under the continental plate and by trench retreat. During this phase, whole mantle convection system is activated and positive tractions at the base of the overriding plate are induced by the large-scale poloidal cell. The width of the convective cell grows by increasing the rheology contrast between the upper and lower mantle, whereas the height is limited by the finite distance between CMB (i.e. Core-Mantle Boundary) and base of the plates lying at the surface. As such, the convective cell aspect ratio is larger than 1. With the same deformation mechanism previously described, the upper plate is subject to active mantle drag F_{AD} closer to the trench counterbalanced by passive mantle drag on the opposite side of the future break-up point, causing thus a irreversible stretching that culminates with break-up of the continental plate (Fig. 3.8-D1). After break-up, the right part of the continent strongly coupled with subducting plate follows the backwards motion of the trench, leading to the drifting of the continent (Fig. 3.8-D2). For this model we have found an amount of active mantle drag F_{AD} = 1,17 $\cdot$ 10^{13} N/m and passive drag F_{PD} = 0,55 $\cdot$ 10^{13} N/m, and consequently a plate internal tension greater than the integrated strength B_1 = 0,53 $\cdot$ 10^{13} N/m (cf. Fig. 3.6-A); all of these values are summarized in Table 3.4 - Test 047.

3.3.3 Stagnant slab

If the lower mantle viscosity exceeds >150 times that of the upper mantle, a different output during our numerical simulations is obtained,

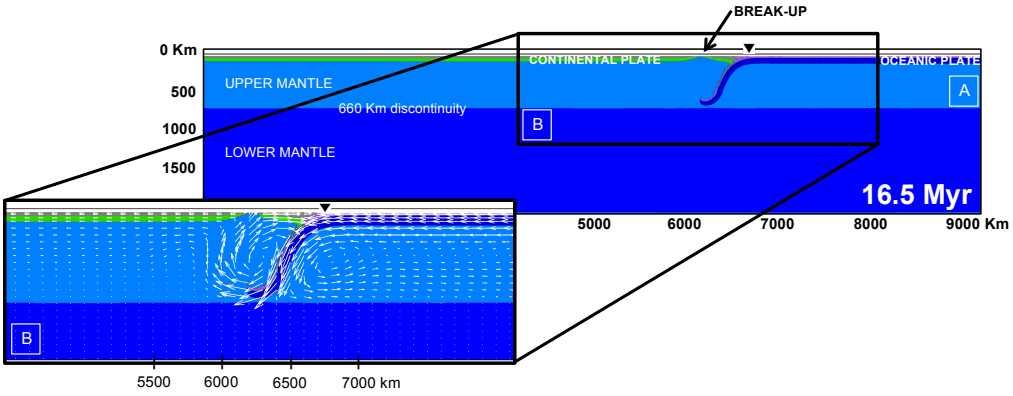

Figure 3.9: Snapshot of the stagnant slab style of subduction. [A] Shows the large-scale subduction and [B] superimposes the velocity field to display how the narrow active mantle drag leads to the break-up of the microcontinent. Solid triangles show trench position.

which defines a third style of subduction characterized by a stagnant slab (Fukao *et al.* , 1992). For these cases, slabs tend to be deflected or flattened in a depth range corresponding to the upper-lower mantle transition. Unlike the slab avalanche model, the slab is not reaching the lower mantle and subduction-induced convection is thus confined in the upper mantle. Consequently, positive tractions affect only a narrow portion of the continental plate that does not exceed 500 km of length, while the rest of the overriding plate resists drifting strongly aided by trench suction forces. Figure 3.9-A illustrates the dynamic of the stagnant slab model. The oceanic lithosphere sinks vertically and induces a relatively small convective cell with aspect ratio of ~1 and ~600 km wide (comparable to the thickness of the sub-lithospheric upper mantle). Flow diverges at ~750 km from the trench (Fig. 3.9-B) and therefore a narrow portion of the continental plate is affected by active mantle drag. On the opposite side from the point of flow divergence, mantle resists continent drifting with a passive viscous drag, thus promoting the extensional deformation. When the slab is bending at 660 km the poloidal velocity

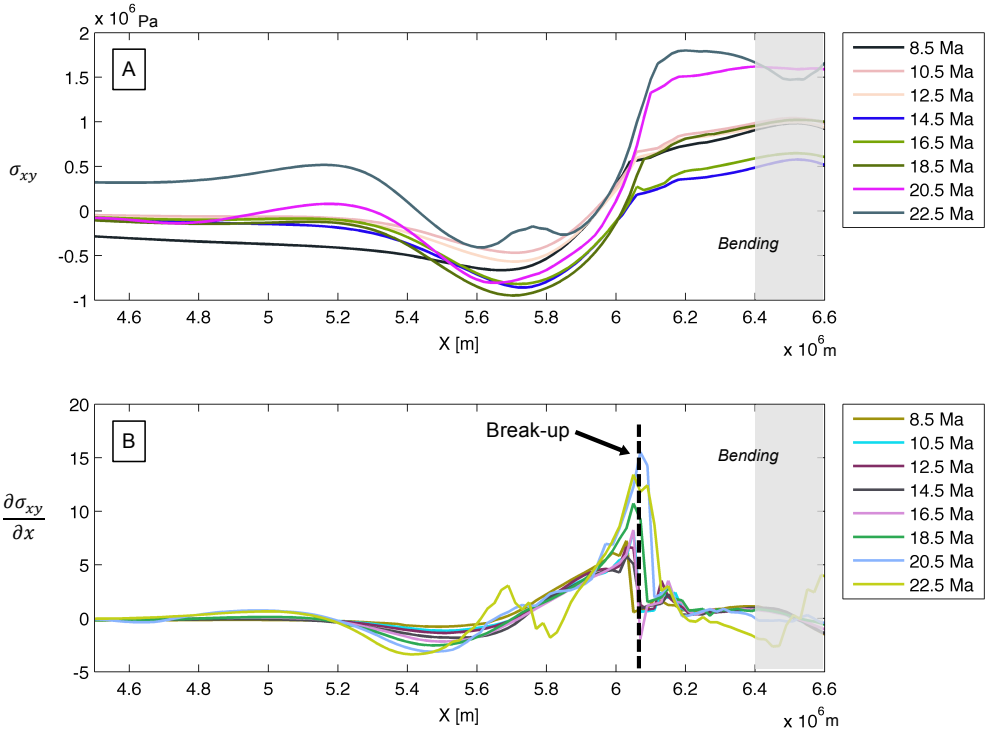

Figure 3.10: Profiles of shear stress [A] and shear stress gradient [B]. These profiles are referred to the reference model of stagnant slab and are taken along the base of the continental lithosphere for the most important timesteps.

field sharply decrease and active mantle drag loses its intensity. Indeed, our stagnant slab models develop the break-up during the first phase of subduction, before the slab encounters the bottom of upper mantle. Successively, slab retreat drives the drift of the microcontinent. Following the method previously described, we have taken the reference model of stagnant slab and through a series of shear stress profiles under the overriding plate we have analysed how the horizontal shear stress evolves over time. Given that in stagnant slab models mantle drag forces are stronger near the trench, we have plotted a series of shear stress profiles at different timestep in the range from X = 4500 km to 6600 km (Fig. 3.10-A and -B). First of all, appreciable values of shear stress (Fig.

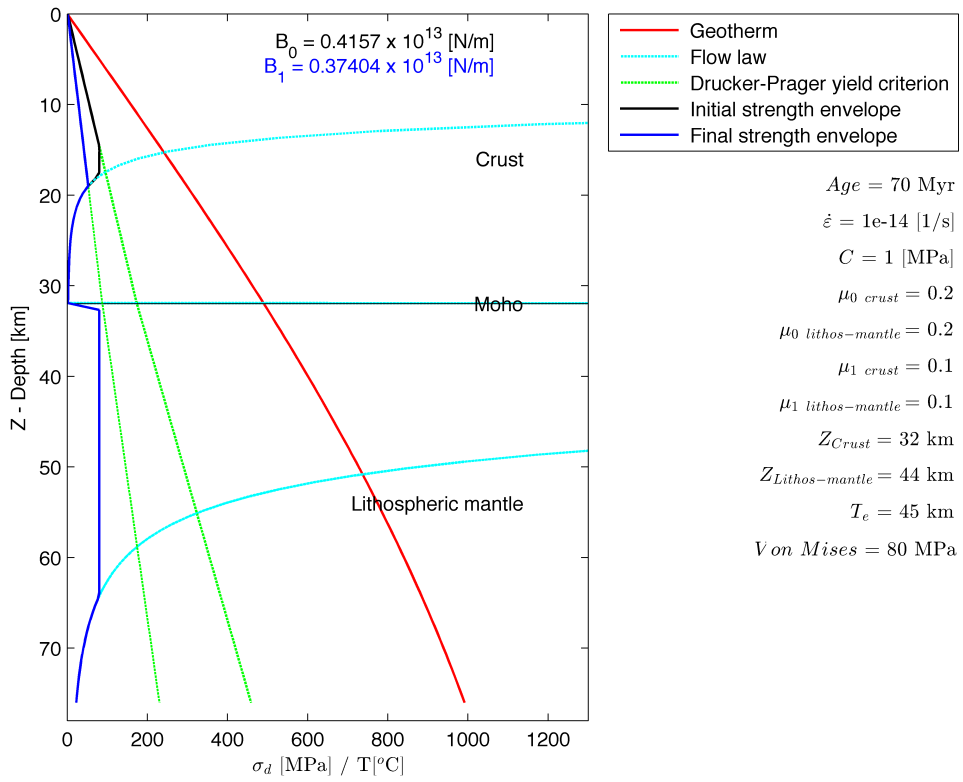

Figure 3.11: Yield strength envelope of the stagnant slab reference model. Thickness of crust and lithospheric mantle, cohesion and coefficients of friction, are parameters that we have similarly used in the previously simulations, but with a Von Mises yield criterion of 80 MPa.

3.10-A) can be found starting from X~5200 km, where significant F_{PD} develops as indicated by a series of parables with upward concavity. On the other hand, as these profiles get closer to the trench, the shear stress values become positive and reach a peak at ~6200 km, that is ~500 km from the trench. Unlike the penetration slab model, the shear stress gradient profiles vary more sharply and in a narrower range (Fig. 3.10-B), especially in the range from ~5900 to ~6200 km. Because the convective cell induced by the sinking of the slab is confined in the upper mantle, the positive values of the shear stress gradient are very near the trench

and the continental break-up is thus localized at the peak of ~6100 km (Fig. 3.10-B dashed line).

Unlike subduction models characterized by slab penetration into the lower mantle, stagnant slab develops both an active and passive mantle drags that are one order of magnitude smaller (i.e. F_{AD} = 0,06 · 10^{13} N/m; F_{PD} = 0,04 · 10^{13} N/m; cf. Table 3.4 - Test 021). To trigger the continental break-up, we were forced to impose the Von Mises yield criterion of to 80 MPa (Fig. 3.11). Break-up occurs although the integrated strength (B_1 = 0,37 · 10^{13} N/m) is higher than the passive mantle drag F_{PD}. As already seen in other models, we suggest that suction forces ($\geq$ 0.33 · 10^{13} N/m) associated with trench retreat are here crucial for the break-up of the continent.

3.3.4 Point of break-up vs. viscosity contrast

Through analysis of several numerical simulations, we have noted that point of break-up changes for each model as the viscosity contrast increases. Therefore, we have dedicated nine numerical experiments in order to understand the relationship between the point of break-up and viscosity contrast; Table 3.3 shows in detail the parameters chosen for these numerical simulations.

We have measured the distance from the break-up point to the trench and then we have plotted these values against the viscosity contrast between upper and lower mantle (Fig. 3.12). In the range of viscosity contrast from 1 to 150, which encloses the penetrating and avalanche slab style of subduction, we have measured distances among trench and break-up point ranging from 2850 km to 3590 km. Higher values of viscosity contrast could not be tested because stagnant slab style of

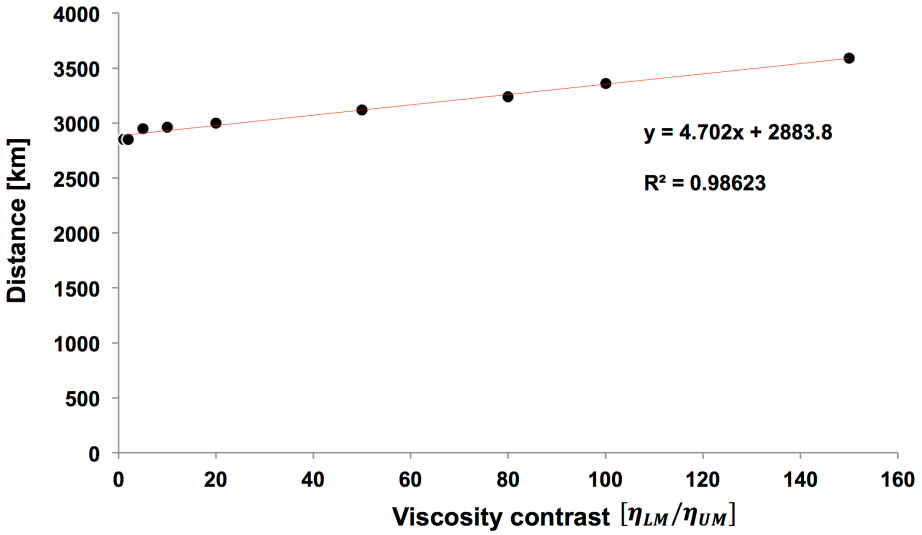

Test	η LM / η UM
L_050	1
L_051	2
L_052	5
L_053	10
L_054	20
L_044*	50
L_055	80
L_041	100
L_047*	150
*reference model	

d2: distance from zero to trench; **d1**: distance from zero to break-up point;

		d = d2 - d1
d2 [km]	d1 [km]	d [km]
6800	3950	2850
6750	3900	2850
7150	4200	2950
7160	4200	2960
7200	4200	3000
7420	4300	3120
7440	4200	3240
7340	3980	3360
7240	3650	3590

Figure 3.12: Scatterplot that correlates upper-lower mantle viscosity ratios (i.e. viscosity contrast) and point of break-up (i.e. distance from trench to break-up point).

Mantle viscosity $(Pa \cdot s)$			**reference models*
	upper mantle	*lower mantle*	*viscosity contrast*
Tag	η_{UM}	η_{LM}	η_{LM}/η_{UM}
			Penetrating slab
Test_50	$3 \cdot 10^{20}$	$3 \cdot 10^{20}$	1
Test_51	$3 \cdot 10^{20}$	$6 \cdot 10^{20}$	2
Test_52	$3 \cdot 10^{20}$	$1.5 \cdot 10^{21}$	5
Test_53	$3 \cdot 10^{20}$	$3 \cdot 10^{21}$	10
Test_54	$3 \cdot 10^{20}$	$6 \cdot 10^{21}$	20
Test_44*	$3 \cdot 10^{20}$	$1.5 \cdot 10^{22}$	50
Test_55	$3 \cdot 10^{20}$	$2.4 \cdot 10^{22}$	80
			Slab avalanche
Test_41	$3 \cdot 10^{20}$	$3 \cdot 10^{22}$	100
Test_47*	$3 \cdot 10^{20}$	$4.5 \cdot 10^{22}$	150

Table 3.3: Viscosity values chosen for numerical simulations run to understand the relationship between the point of break-up and viscosity contrast.

subduction develops. Nevertheless, we interpret the resulting linear relationship as due to the widening of the poloidal cell in response to the linearly increasing viscosity contrast between the two mantle layers. This aspect of the numerical simulations will be further discussed in Chapter 4.

3.4 Further numerical simulations

The effect of continents on the evolution of mantle flow and plate tectonics is the central aspect of this thesis. Our reference models refer to the break-up and drifting of the continental plate assuming three different subduction styles: penetrating slab, slab avalanche and stagnant slab. In this part of the thesis we present a set of further numerical simulations,

where we have tested different rheological models of the:

1. upper mantle, by imposing either a more realistic non-Newtonian rheology or a low-viscosity channel simulating a weak asthenospheric layer at the base of the tectonic plates;

2. continental lithosphere, by increasing the plate thickness (i.e., strength) and by imposing lateral variations of the plate strength.

3.4.1 Low-viscosity channel

There are a number of evidences that support the hypothesis of significant variations of viscosity in the uppermost mantle. If solid rocks beneath the lithosphere are sufficiently hot, a thin layer with different rheological properties may be formed below the lithosphere. This layer is known as asthenosphere. The lithosphere slides over the asthenosphere with relatively little resistance. The coupling/decoupling between the lithosphere and asthenosphere has significant implications for understanding many important aspects of plate tectonics and geodynamics (Doglioni *et al.* , 2011). To drive plate motion, mantle convection requires coupling at the lithosphere-asthenosphere interface.
Important information on the fluid behaviour of the Earth's mantle comes from studies of the dynamic response of the mantle to loading and unloading at the surface. The growth and melting of ice sheets, occur sufficiently fast so that dynamic effects are important in the adjustment of the mantle to the changing surface load (Turcotte & Schubert, 2002). The rate of rebound due to growth and melting of ice sheets has been used in order to determine the solid-state viscosity of the mantle. Taking into account a lithosphere thickness of 100 km, the dynamic vis-

cosity was defined as $4 \cdot 10^{19}\ Pa \cdot s$ for a 75 km thick asthenospheric layer. Other studies suggest that this value is representative of the asthenospheric viscosity beneath oceanic plates, while a value of $\sim n\ x\ 10^{20}$ is normally inferred for the colder sub-continental asthenosphere (Doglioni *et al.* , 2011).

In addition, Earth's models based on seismic P- and S-waves tomography show that the asthenosphere is stratified and laterally heterogeneous (e.g. Panza *et al.* , 2010). In its uppermost part, between 90 and 200 km of depth, the asthenosphere (or also called the low-velocity anisotropic layer, Anderson, 2010) contains a well-developed low-velocity zone, LVZ (e.g. Dziewonski & Anderson, 1981), where the velocity decrease of S-waves is larger than that of P-waves, possibly indicating the presence of a small amount of melt that would lower the asthenosphere viscosity.

Here we have tested the presence of the asthenosphere that has been implemented by imposing in the reference model a low-viscosity channel ($\eta_{ast} = 3 \cdot 10^{19}\ Pa \cdot s$) in the 90-200 km depth range in order to test whether or not the break-up and drifting of the continental plate occurs. Figure 3.13-A illustrates the chosen values of viscosity as well as the viscosity distribution.

By comparing this numerical simulation with the reference model (i.e. without asthenosphere, Fig. 3.3), we can note that: (1) the subduction velocity of the oceanic plate is slightly higher due to the lower viscous resistance arising from the weak asthenospheric mantle, yielding a greater plate advance (Fig. 3.13-C) and (2) the angle of subduction becomes vertical. When the break-up occurs, the velocity of convergence of the oceanic plate is equal to ~14 cm/yr, ~4 cm/yr higher than the refer-

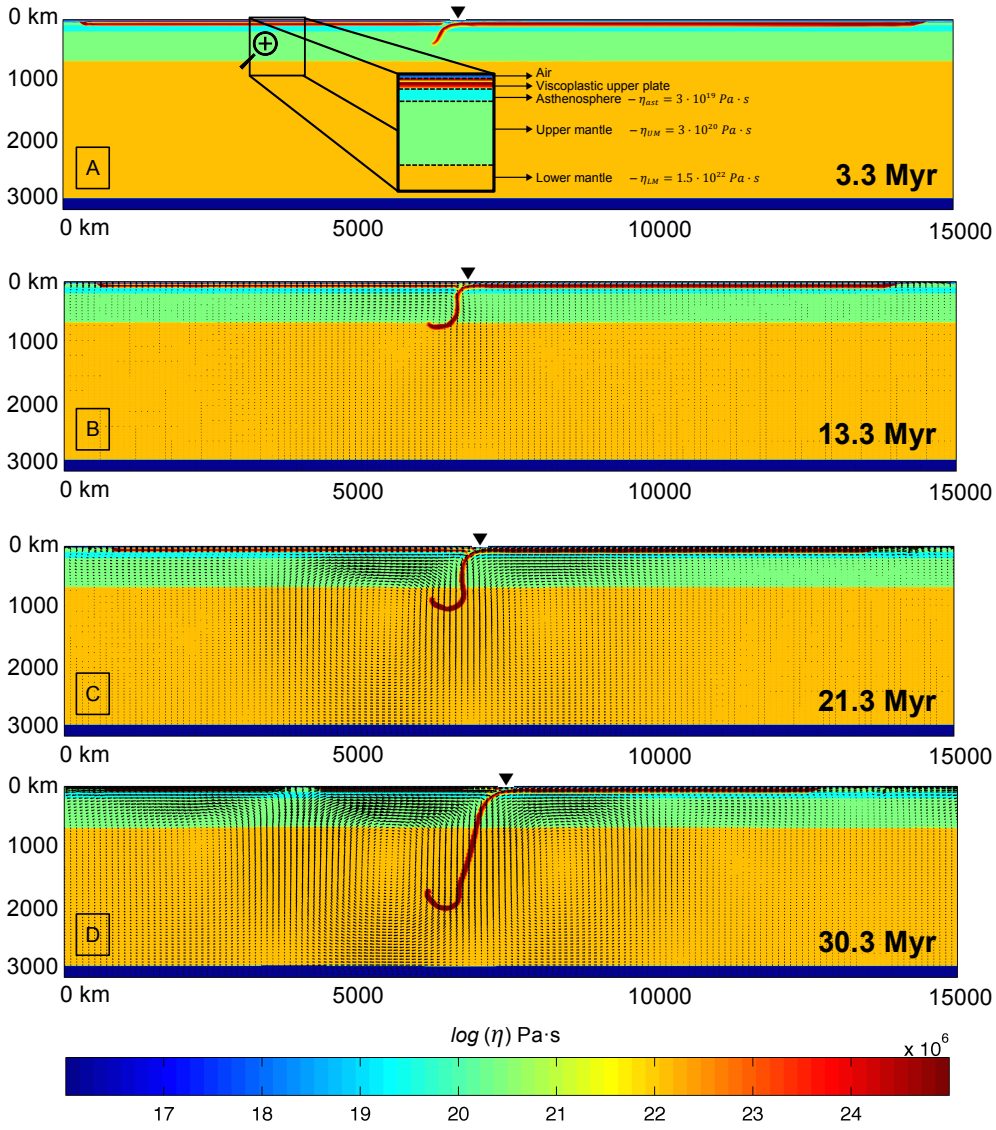

Figure 3.13: Viscosity maps of key snapshots showing the evolution of a penetrating slab model with implemented a thin low-viscosity asthenospheric layer. [A] Initial viscosity distribution. [B] Slab-tip bends at upper-lower mantle boundary. [C] Slab sinks into the lower mantle. [D] Continental plate undergoes the break-up due to active mantle induced by subduction. Solid triangles show trench position.

ence model without asthenosphere (i.e. Test 044). Break-up occurs with the same modality discussed previously, although at a greater distance from the trench (Fig. 3.13-D) than for the reference model without low-viscosity channel. Indeed, we have measured a difference of 180 km, since it occurs at 3300 km from the trench in this model and at 3120 km in the reference model (Test 044). Unlike the model without asthenosphere, during the drifting phase the continental plate near the trench suffers lesser buckling.

Bearing in mind that, except for the asthenospheric layer, the input rheological parameters are the same to the reference model of penetrating slab, we have compared the active and passive mantle drag values with yield strength envelope and integrated strength previously obtained (cf. Fig. 3.6-A). The results indicate that F_{AD} = 0,95 $\cdot$ 10^{13} N/m and F_{PD} = 0,51 $\cdot$ 10^{13} N/m are lower than for the reference model, with F_{PD} being very close to the continent integrated strength B_1 = 0,53 $\cdot$ 10^{13} N/m; values are also schematised in Table 3.4 - Test 046.

3.4.2 Non-Newtonian upper mantle

It is well known that rock deformation at high temperatures and pressures takes place by two fundamental mechanisms: diffusion creep and dislocation creep. However, we do not know perfectly which of these mechanisms governs flow in the mantle. If diffusion creep dominates, the upper mantle behaves as a Newtonian fluid. If conversely dislocation creep is active, the upper mantle is a power-law fluid with stress exponent (n) approximately of 3, i.e. equal to olivine, the most abundant and weakest mineral of the upper mantle.

Laboratory experiments have predicted that the olivine deforms by a

combination of diffusion (Newtonian) and dislocation (non-Newtonian) creep, with non-Newtonian response that dominates in regions of relatively high stress and grain size (Karato & Wu, 1993).

The effect of an upper mantle non-Newtonian viscosity on the deformation of the continental plate during subduction is analysed for a series of models where we varied the yield strength of the continental plate.

During the early stages of subduction, the wedge corner is subject to high stresses as the slab-tip sinks into the upper mantle and a constricted corner flow develops above the slab. In models with non-Newtonian viscosity these stresses act to decrease the wedge-corner viscosity. In addition, the decrease in viscosity surrounding the slab partially decouples the slab from the upper mantle, thus increasing the sinking of the slab owing to a lower resistance to penetration. Nevertheless, if we consider a penetrating slab style of subduction, break-up occurs at 42,4 Myr, ~8 Myr later than the same model with constant mantle rheology.

Moreover, worthy of note is the aspect ratio of the convective cell that grows and becomes ~1.3 (Fig. 3.14-A2). We suggest that the combined effects of (1) a lower slab-dip with respect to the reference model with constant viscosity together with (2) a wide bent-slab tip supply a further horizontal component of flow. As such, mantle flow diverges at a greater distance from the trench and therefore the continental portion being subjected to active mantle drag is widened. Break-up occurs with the same mechanical modality as for the reference model with constant viscosity (Fig. 3.14-B1 and -B2). Afterwards, the oceanic plate retreat and subduction drives the drifting of the overriding plate, while the continental plate portion away from the trench is abruptly slowed and then pushed in the opposite direction by mantle counterflow under it. It is

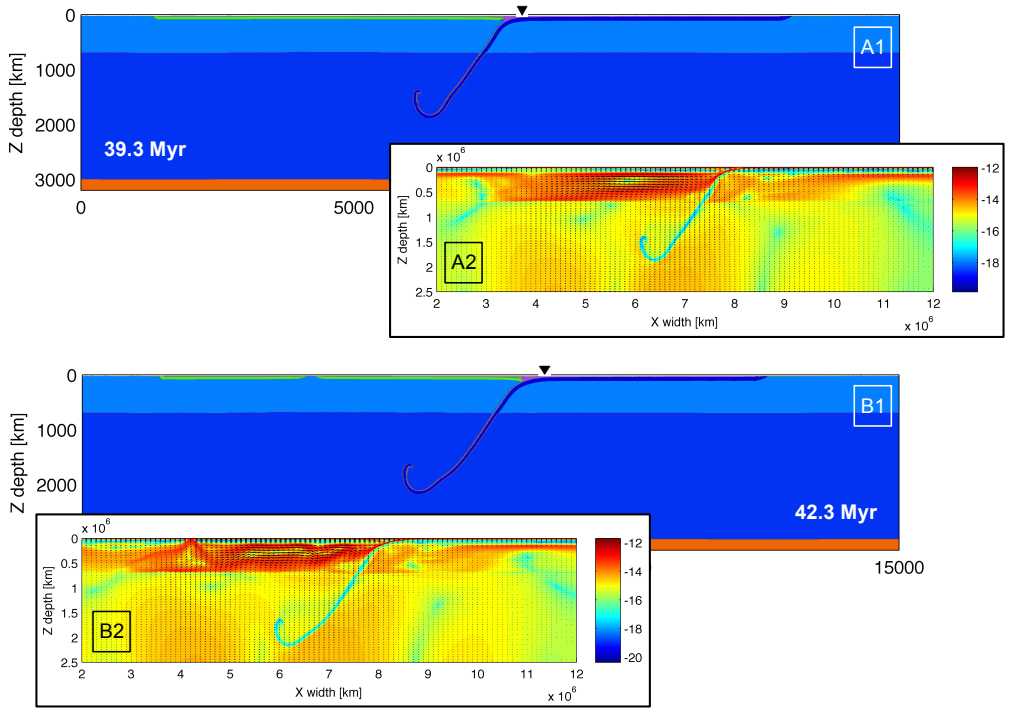

Figure 3.14: Compositional map and second invariant of strain rate of a penetrating slab model with implemented a more realistic non-Newtonian upper mantle. Both snapshots [A1] and [B1] well show a different slab-dip that produces a poloidal flow with aspect ratio of ~1.3. Solid triangles show trench position.

important to note that, similarly to simulations with low-velocity channel (Fig. 3.13) and differently from the reference model (Fig. 3.3), in this experiment no continental buckling develops near the trench area, owing to different basal tractions.

Active and passive mantle drag values are indeed lower (i.e. F_{AD} = 0,78 $\cdot$ 10^{13} N/m; F_{PD} = 0,51 $\cdot$ 10^{13} N/m;) compared to those of the reference penetrating slab model with a higher upper mantle viscosity. However, the plate internal tension given by passive mantle drag F_{PD} is comparable to the corresponding integrated strength (B_1 = 0,53 $\cdot$ 10^{13} N/m) and therefore the continental break-up occurs (cf. also Table 3.4 - Test 061).

3.4.3 Vertical profiles of horizontal velocity

The analysis of the horizontal velocity profiles across the entire vertical section of the model gives insight into the distribution of mantle flow as a function of the different rheological model implemented. We have chosen three different models representative of the main upper mantle rheological structures and behaviours analysed in this study: constant viscosity with (Test 044) and without (Test 046) the asthenospheric layer, and non-Newtonian viscosity (Test 061). Vertical profiles were shown at X = 5800 km because mantle flow of the convective cell at that point becomes horizontal through the entire profile. In addition, velocity profiles are shown one timesteps before the break-up; Figure 3.15 shows these profiles.

If we focus on the upper mantle segment of the profile, we can observe vigorous flow delimited by the upper boundary of lower mantle and by lithospheric plate overlying it. Firstly, it is important to keep in mind that viscosity of both diffusion creep and dislocation creep are directly proportional to the exponential of the inverse absolute of temperature. Thus, the viscosity of the mantle has this strong temperature dependence. In addition, if dislocation creep is the dominant mechanism, the effective viscosity of the mantle will be stress dependent as well. It is important then to consider how the strong temperature dependence and possible stress dependence of mantle viscosity influence convection and shear flow in the mantle.

As explained by Turcotte & Schubert (2002), the simplest fluid is Newtonian, because rate of strain or velocity gradient is directly proportional to the stress applied; upon a pressure gradient, this fluid develops a type flow known as Couette flow, in which the velocity profile is a parabola

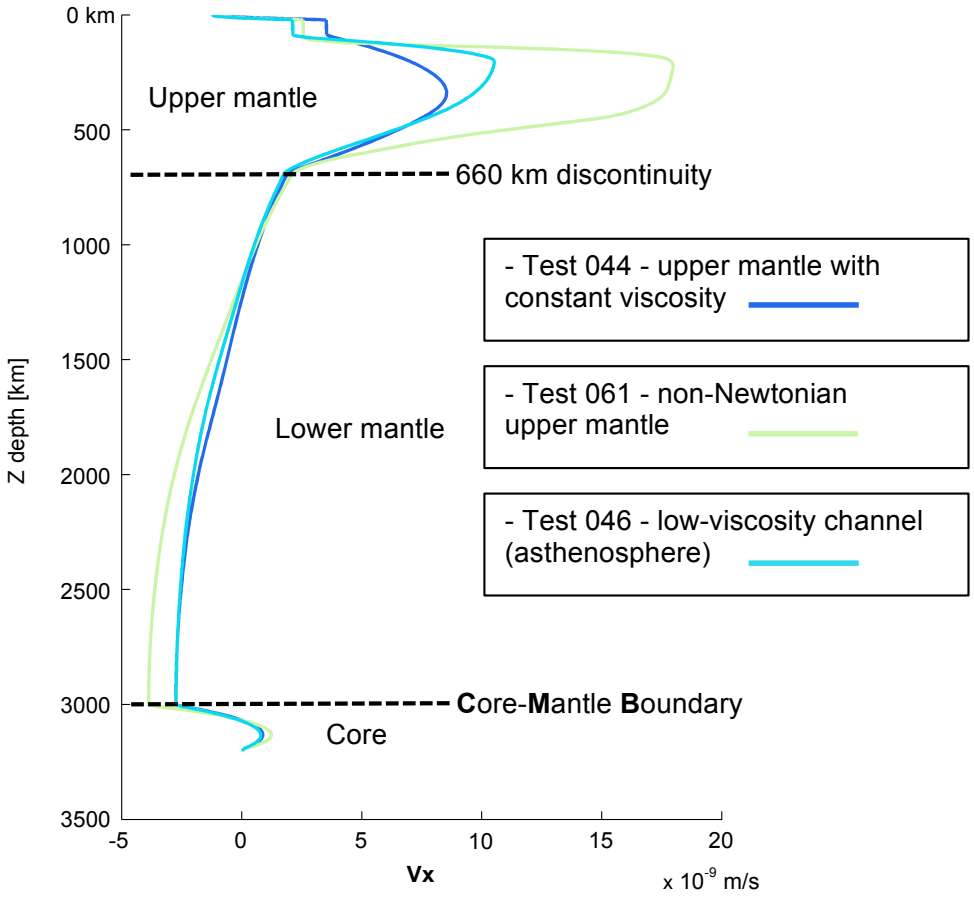

Figure 3.15: Vertical profiles of the horizontal velocity component. These profiles were taken one timesteps before the break-up at 5800 km from zero. Their shapes well-describe the upper mantle behaviour according to the rheology assumed.

that is quasi-symmetric about the half-height of the layer (in this case, the upper mantle; Fig. 3.15, blue line). Similar but more asymmetric is the vertical profile calculated for the asthenospheric-layer model (light blue line). Indeed, owing to low viscosity channel, the horizontal velocity reaches its peak just below the lithospheric plate, though the overriding plate moves more slowly than the model without asthenosphere.
On the other hand, the vertical profile of the Non-Newtonian upper mantle is a typical example of non-linear deformation known as power-

law creep. For stress exponents >1, the viscosity is high where shear stress is small and low where shear stress is large. Because shear stress is small in the center of the channel, the fluid is highly viscous there. Near the walls where shear stress is high, effective viscosity is low, and the velocity gradients are large. As a result, plug-flow establishes within the Non-Newtonian upper mantle (green line).

3.4.4 Cratonic keel

The episodic nature of Earth's internal dynamics has long been recognized, even before plate tectonics became a paradigm (Sutton, 1963). The Wilson cycle, which describes the alternating opening and closing of an ocean basin between two continents, is a famous example (Wilson, 1966) and the episodic clustering and subsequent dispersal of continents in the course of the supercontinent cycle is its global manifestation. For the last 200 - 250 Myr of Earth's history the preserved ocean floor provides sufficient data to reconstruct the kinematic motion of Earth's tectonic plates (e.g. Seton *et al.* , 2012), revealing the aggregation of the latest supercontinent, Pangaea, as already proposed by Alfred Wegener about a hundred years ago, and its break-up at ~180 Ma.

The common view is that significant portions of Archean crust have been stabilized by cratonization. Cratons with a strong and cold root can develop a continental thickness of 250 km (e.g. Gung *et al.* , 2003). The detailed mechanisms of craton formation are not well-known yet, but are likely to be either related to high-degree melting in very hot plume heads, or to the accretion of oceanic or arc lithosphere, or to continental collision, or to a combination of these (Gerya, 2014). Cratons are often

depleted in volatiles (Pollack, 1986) and relatively dehydrated, which has been proposed to cause their high strength as well as their strong resistance to deformation and their tectonic quiescence (Karato, 2010). Continents can be formed by a single or several cratons connected by relatively weak lithospheric portions (aborted rift zones, old collision zones, etc.). For these reasons, we have run further numerical simulations with a continental plate characterized by a cratonic keel.

Our model builds on the one previously described. However, in the present study we allow for a somewhat more complex continental structure, such that continents consist in a laterally different thermal structure, namely a strong interior (representing the craton and cratonic keel), which is surrounded by weaker continental margins. Age varies laterally from 70 Myr (for both side, ~300 km length) to 150 Myr into the central body according to the half-space cooling model. Rheology of whole mantle is constant and the initial thickness of the cratonic keel is 150 km and both lateral terminations remains are 76 km thick; Figure 3.16 shows the initial setup (Fig. 3.16-A) and the evolution of this model. Results indicate that stronger plates generally delay or do not produces break-up, but also they seem to generate stronger poloidal flow in 2-D, which enhances drifting of continents and the coupling between plates due to longer delamination and shallow subduction.

Initially, the slab descends into the upper mantle down to the top of the lower mantle, while slab-dip progressively increases and becomes vertical (Fig. 3.16-B). When the slab passes through the 660 km discontinuity, both rates of subduction and trench retreat increase, slab-dip becomes shallower and underthrusting under the overriding plate enhances the

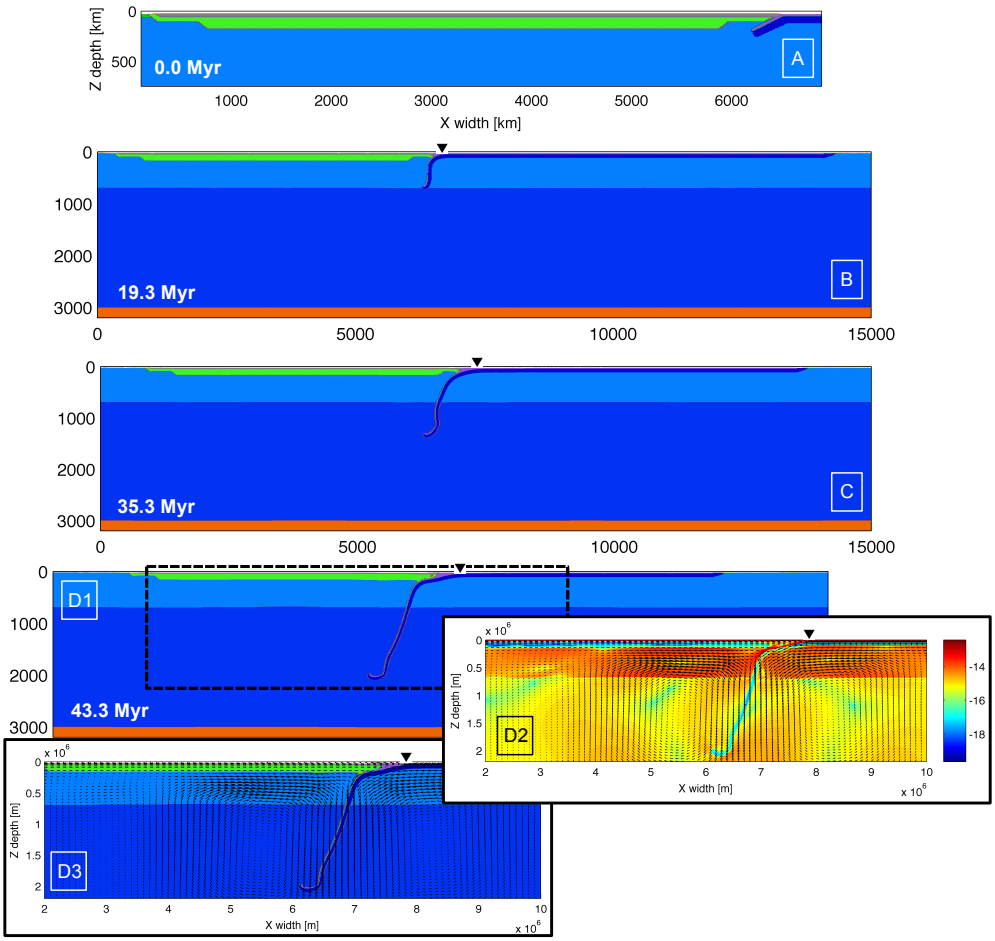

Figure 3.16: Snapshots of the reference model of the penetrating slab with implemented a continental cratonic keel. The model develops a one-sided oceanic-continental subduction with a dynamic of penetrating subduction into the lower mantle. [A] Initial setup of the cratonic keel. [B] Slab sinks into the upper mantle until to bend as soon as the upper-lower mantle transition is encountered due to resistance to penetration of the lower mantle. [C] After penetration, slab vertically moves downward, the subduction becomes shallower at the contact among the plates and trench retreat increases. [D1] Final-state of subduction. [D2] Logarithm of the second invariant of the strain rate with velocity field superimposed shows the deformation rate distribution and the point under the continental plate where the deformation localizes, but without triggering any continental break-up. [D3] Compositional map with velocity field superimposed shows how whole-mantle convective system is activated.

coupling between the plates (Fig. 3.16-C).

At ~43 Myr shallow subduction takes place and slab retreat slows down, leading the accretion of continental lithosphere above the wedge-corner flow region (Fig. 3.16-D). Given that penetration into the lower mantle enhances the slab pull, the slab-dip sharply increases and becomes nearly vertical; this triggers a poloidal cell with aspect ratio of ~1.

Tension generated by active and passive mantle drags slightly deform the continental plate, but without causing the break-up. Indeed, although active and passive mantle drags reach very high values (i.e. F_{AD} = 3,03 $\cdot$ 10^{13} N/m; F_{PD} = 1,52 $\cdot$ 10^{13} N/m), break-up does not occur because the integrated strength (B_1 = 3,95 $\cdot$ 10^{13} N/m, Fig. 3.17) is greater than the internal tension (cf. Table 3.4 - Test 086).

3.4.5 Intracontinental weak-zones

Lateral variations in lithospheric strength have been adopted often in flexural modeling (both 2-D and 3-D) to better fit the basement deflections caused by (orogenic) loading of the lithosphere, typically supported by gravity data. This approach provides essentially a 'snapshot' of the role of lithosphere strength in determining the present day geometry.

As explained by Wilson cycle (Wilson, 1966), the second stage of continent splitting is the formation of a seafloor-spreading center, or ocean ridge. The normal faults associated with the margins of the rift valley form the margins of a new ocean. The margins of the opening ocean are known as passive continental margins and correspond to zones of weakness. As the ocean basin adjacent to a continent grows older, it con-

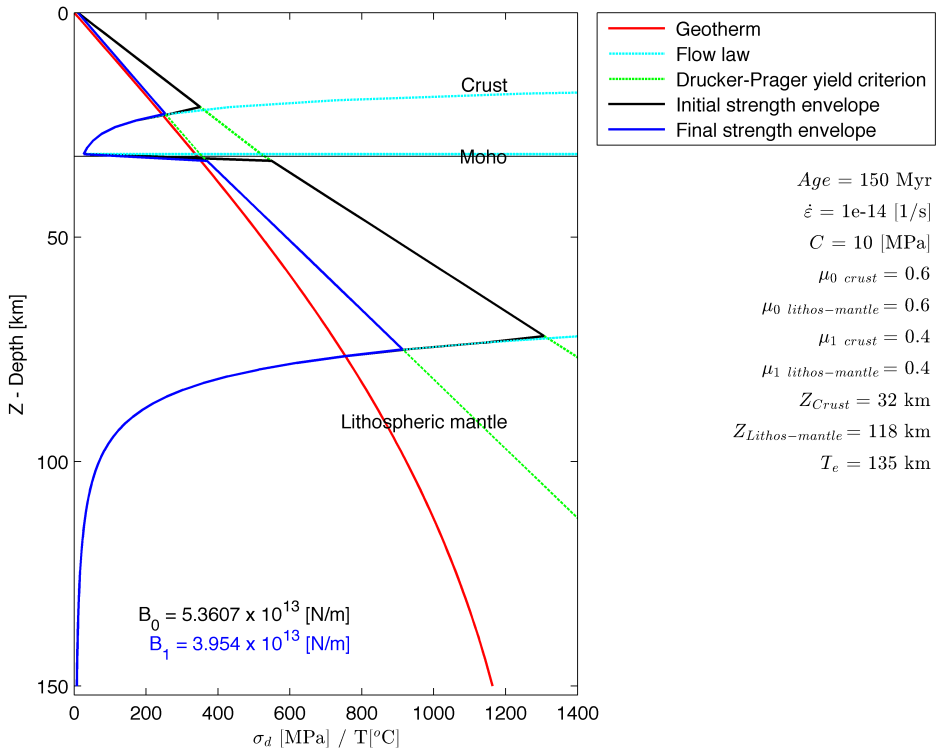

Figure 3.17: Yield strength envelope of the model with a cratonic keel. Due to the thick lithosphere and high values of cohesion and coefficient of friction, the integrated strength is high.

tinues to subside relative to the continent. This differential subsidence is accommodated on the normal faults associated with the continental margin. Normal faults inherently are zones of weakness, and they may play a key role in the formation of new ocean trenches, when a passive continental margin is converted to an active continental margin. Even more important, when subduction takes place, these weakness zones may trigger large-scale deformation mechanisms.

In order to simulate a more realistic laterally heterogeneous continental lithosphere, we have inserted one or more weak-zones within the upper plate. The weak-zones are 20-40 km wide, they extend through the

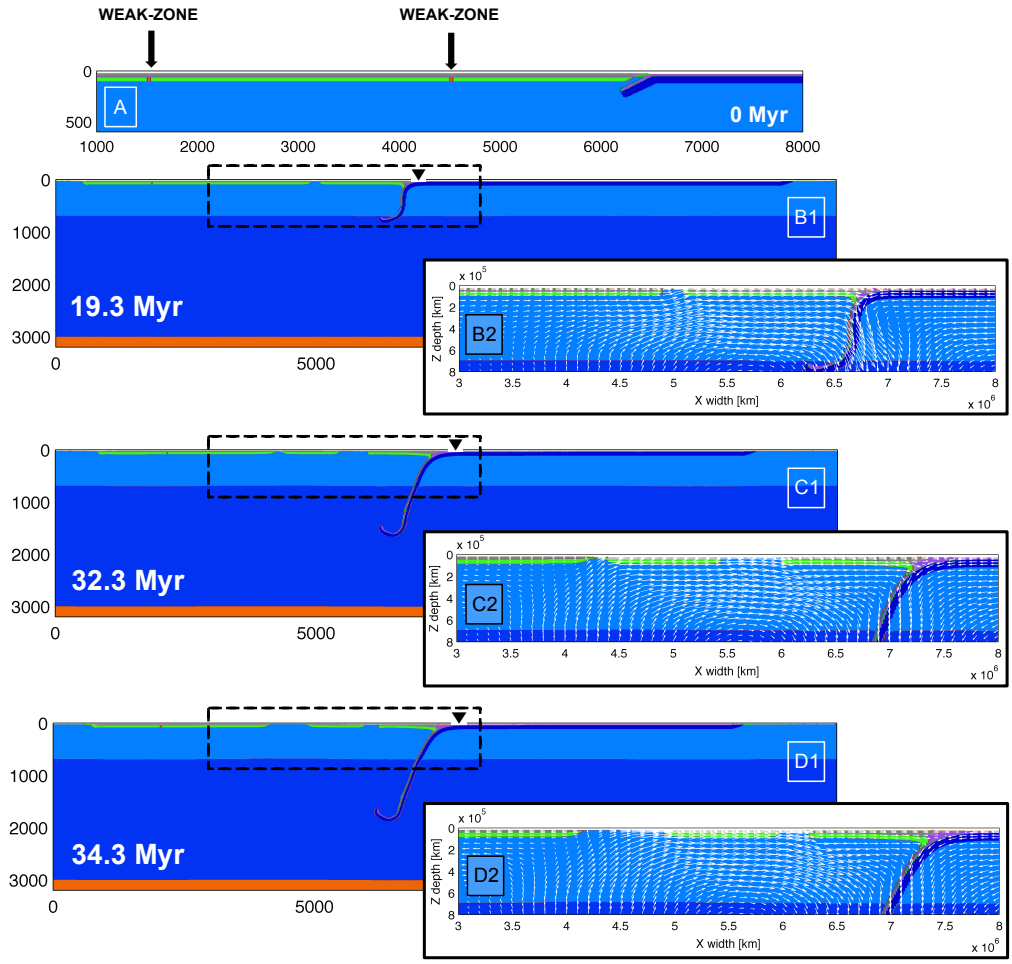

Figure 3.18: Evolution of a penetrating slab subduction style with implemented two weak-zones within the continental lithosphere. [A] Illustrates the initial setup. [B1; C1 and D1] show the subduction sequence and their corresponding zoom images [B2; C2 and D2] help to analyse how active mantle drag propagates below the continental lithosphere. Solid triangles show trench position.

whole continental lithosphere and they are defined by a low maximum (von Mises) yield strength (from 10 to 20 MPa). Finally, constant viscosities for both the upper and lower mantle were defined.

For the case analogous to the reference model with penetrating slab and whole mantle convection, we have inserted two weak-zones at X = 1500

and 4500 km of 20 km length and 10 MPa of yield strength; Figure 3.18 reproduces key snapshots of this simulation.
After 10 Myr, the upper plate starts to deform at the weak-zone nearer to the trench, thus triggering a first break-up (Fig. 3.18-B1). Indeed, due to very low integrated strength (B_1 = 0,07 $\cdot$ 10^{13} N/m), as soon as subduction initiates the break-up can be triggered by either trench suction forces or by the tractions acting at the bottom of the upper plate (F_{AD} = 0,10 $\cdot$ 10^{13} N/m; F_{PD} = 0,33 $\cdot$ 10^{13} N/m; cf. Table 3.4 - Test 063).
At about 32 Myr, after slab penetration, a second break-up phase affects the upper plate, thus separating the lithosphere into three smaller continents (Fig. 3.18-C1 and -C2). The two continents closer to the trench follow the backward motion of trench retreat, driving them adrift (Fig. 3.18-D1 and -D2).

Numerical simulations of stagnant slab (e.g., Test 109) have been set with a different distribution of weak-zones, while maintaining the same Von Mises yield criterion of the weak-zones (i.e. 10 MPa) and constant viscosity of both the upper and lower mantle. Since poloidal mantle flow is narrow near wedge-corner flow, we have inserted several weak-zones spaced 100 km, between X = 4800 km and 6200 km and with 40 km length; Figure 3.19, shows the sequence of the zoom area near the trench. As slab sinks into the upper mantle, mantle flow develops the typical convective cell and a microcontinent, which does not exceed ~500 km length, irreversibly deforms in correspondence of the weak zones that lie above the area where the flow is diverging (Fig. 3.19-B2). Also in this case, we suggest that the combined effect given by the active mantle drag (F_{AD}) and the trench suction force (F_{TS}) play a fun-

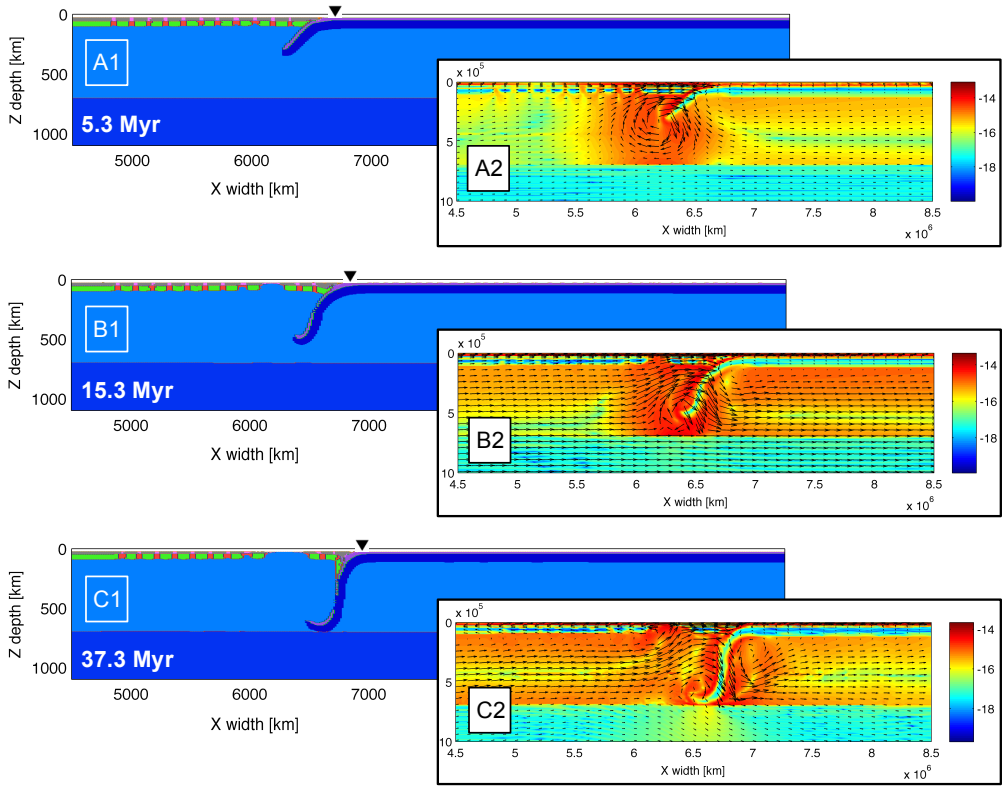

Figure 3.19: Zoom snapshots of the stagnant slab with implemented a series of weak-zones and with non-Newtonian rheology of the upper mantle. Compositional maps [A1-B1-C1] show the evolution of the typical stagnant slab, while zoom images of the second invariant of strain rate [A2-B2-C2] with superimposed the velocity field describe the strain rate distribution and the shape of the convective cell induced by subduction. Solid triangles show trench position.

damental role with respect to the break-up and subsequent drift of the microcontinent (Fig. 3.19-C1 and -C2). Given that the deformation of the continental plate develops as soon as slab sinks into the upper mantle, suction forces due to trench retreat are likely to be the most important for this case. In any case, the passive mantle drag is equal to $F_{PD} = 0{,}15 \cdot 10^{13}$ N/m, while the active mantle drag reaches values of $F_{AD} = 0{,}11 \cdot 10^{13}$ N/m and therefore greater than to integrated strength of the weak-zones ($B_1 = 0{,}07 \cdot 10^{13}$ N/m); see Table 3.4 - Test 109.

Through these results, three interesting hypotheses can be formulated:

1. The interaction among plates resists to trench motions.
2. When active mantle drag propagates below a wide portion of the overriding plate, break-up occurs regardless of the weak-zones.
3. Trench suction due to slab retreat drives drift of the microcontinent, even when active mantle drag loses its intensity.

Test	Subduction -style	Plate thickness [km]	Age [Myr]	$\mu_0; \mu_1$	Cohesion [MPa]	Von Mises [MPa]	Init-strength (B_0) x 10^{13} [N/m]	Final-strength (B_1) x 10^{13} [N/m]	Passive drag (F_{PD}) x 10^{13} [N/m]	Active drag (F_{AD}) x 10^{13} [N/m]	Tension (T) x10^{13} [N/m]	Break-up
021	stagnant	76	70	0.2; 0.1	1	80	0.41	0.37	0.04	0.06	0.04	yes
044	penetrating	76	70	0.2; 0.1	1	300	0.88	0.53	0.75	1.17	0.75	yes
046	penetrating	76	70	0.2; 0.1	1	300	0.88	0.53	0.51	0.95	0.51	yes
047	avalanche	76	70	0.2; 0.1	1	160	0.88	0.53	0.55	1.17	0.55	yes
061	penetrating	76	70	0.2; 0.1	1	300	0.88	0.53	0.51	0.78	0.51	yes
063	penetrating	76	70	0.2; 0.1	1	10	0.07	0.07	0.33	0.10	0.10	yes
086	penetrating	150	150	0.6; 0.4	10	/	5.36	3.95	1.50	3.03	1.50	no
109	stagnant	76	70	0.2; 0.1	1	10	0.07	0.07	0.15	0.11	0.11	yes
118	penetrating	76	70	0.6; 0.6	10	/	1.99	1.99	1.46	3.53	1.46	yes
119	penetrating	150	150	0.2; 0.1	1	/	2.29	1.36	3.62	1.79	1.79	yes
120	penetrating	150	150	0.6; 0.4	1	/	5.30	3.89	3.58	2.35	2.35	no

Table 3.4: Table that recaps, for the most important tests, parameters of both active (F_{AD}) and passive (F_{PD}) mantle drag from which we defined the effective tension (T); initial (B_0) and final (B_1) integrated strength; eventual Von Mises (i.e. cut-off) yield criterion; age of the continental plate and input rheological parameters.

Chapter 4

Is mantle flow pattern a function of the viscosity contrast?

Starting from the 60's, insights into the relationship between plates' motion and related mantle flow pattern have been gained by predictions based on numerical modeling techniques. Initially, this problem has been considered by Pan & Acrivos (1967), whose primary aim was an experimental investigation of the flow pattern in the Reynolds number range from 20 to 4000. Using similar models, other simulations have explored the fluid motion driven by the combined effects of a moving wall and natural mantle convection (Torrance *et al.* , 1972) inside a rectangular cavity with different height/width ratios. Again via viscous flow in a cavity Davies, 1977, and Lux *et al.* , 1979, have showed some simple solutions that indicate the relationship among plates' motion and flow patterns in the Earth's mantle. Through all of these studies, the most important results suggest that (1) viscous flow entrained by the larger lithospheric plates may activate the whole mantle convective system if its properties are fairly uniform; (2) secondary circulation cells are gen-

erated under stationary plates by the flow entrained by an adjacent moving plate and, in particular, these secondary cells are of opposite sense to the adjacent cells. Finally, (3) the flow under a convergent margin between a stationary and a moving plate tends to dip obliquely under the stationary plate.

Taking into account the results described in Chapter 3, the coupling between a rigid lithospheric plate and the mantle flow induced by either the dynamic vertical sinking of a rigid-slab or by the movement kinematically imposed on the lateral boundary on the computational domain is investigated using a simple two-dimensional numerical model. We have adopted a simplistic approach using elementary mechanical simulations that yield a clearer framework for the problem. Instantaneous velocity field and stream function solutions are examined, focusing on the poloidal mantle flow as a function of boundary conditions and viscosity contrast between upper and lower mantle.

The 2-D MatLab code **SINDRICO** can be found in the Appendix B.

4.1 Model setup

Our intention here is to study the coupled tectonics of the mantle-continents system. We start by considering a first-order point of view of that problem: vertical sinking of cold and dense subducting plates can affect the flow pattern of the Earth's mantle, which in turn propagates under the continental plates. Hence, to investigate how and to which extent the mantle flow evolves under the continental plate, a convection model that generates mantle- and plate-like behaviour it was defined. The two-

dimensional simulations are performed using a mechanical code with a viscous rheology, which is written in MatLab using finite differences method and marker-in-cell technique. The 2-D code was already used for previous studies and successfully tested. The physical model consists of a rigid upper plate and two weak-bearings along the boundaries to allow the plate lateral movement, an upper and a lower mantle that make up a 9000 km wide and 3000 km deep Cartesian domain.
The standard 2-D model consists of 91 (horizontal direction) and 31 (vertical direction) Eulerian grid points, which are uniformly allocated. Lagrangian particles are 364 x 124 along x and y respectively and randomly distributed. Continuity equation is solved assuming an incompressible material. Boundaries condition are set to free slip on the top, bottom and left side, while the right-boundary has a kinematic setup through a constant velocity gradient along boundary, according to following condition:

$$vy_{i,j} - \frac{1}{3} vy_{i-1,j} = \frac{2}{3}\,; \tag{4.1}$$

All physical variables were scaled through scaling factors initially defined as follow:

$$D^{'} = 3000\,km\,; \;\; \eta^{'} = 1 \cdot 10^{20}\,Pa \cdot s\,; \;\; v^{'} = 5\,cm/yr\,; \tag{4.2}$$

from which we have determined the following characteristic scaling factors:

$$t' = \frac{D^{'}}{v^{'}}\,; \tag{4.3}$$

$$\sigma' = \frac{(v')^2}{D'}\,; \tag{4.4}$$

$$\rho' = \frac{\eta'}{v'D'}\,; \tag{4.5}$$

$$a = \frac{(v')^2}{D'}\,; \tag{4.6}$$

Hence, results are presented as a function of adimensional variables. Figure 4.1 shows an initial model setup and Table 4.1 summarized the scaling values of thicknesses, density and viscosity of the rock types used.

In order to represent the trajectories of particles in a steady flow and given that the model assumed an incompressible material, we have calculated the volumetric rate flow, also called stream function (ψ):

$$(\frac{\partial^2\psi}{\partial x\partial y}) - (\frac{\partial^2\psi}{\partial y\partial x}) = 0\,; \tag{4.7}$$

simplifying to:

$$\frac{\partial}{\partial x}(\frac{\partial\psi}{\partial y}) + \frac{\partial}{\partial y}(-\frac{\partial\psi}{\partial x}) = 0\,; \tag{4.8}$$

and if considering that:

$$\frac{\partial\psi}{\partial y} = -vx\,;\ \ \frac{\partial\psi}{\partial x} = vy\,; \tag{4.9}$$

a stream function $\psi_{i,j}$ is one that satisfies:

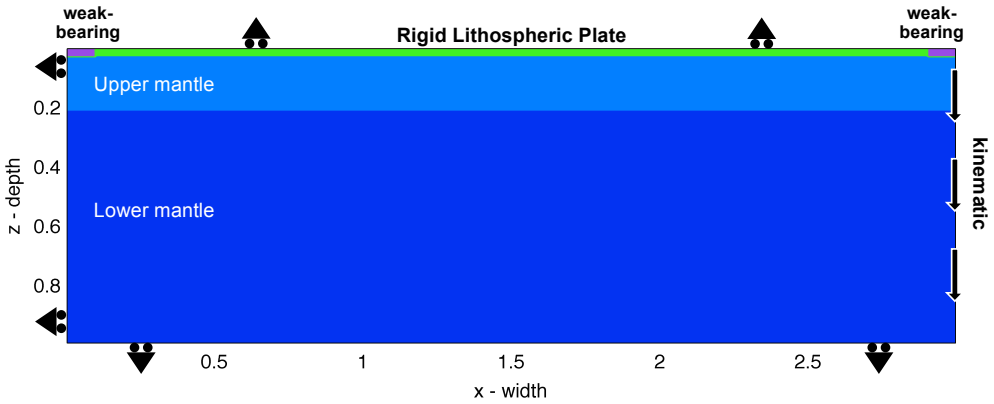

Figure 4.1: Initial setup of the scaling model. 1 of depth, 3 of width; 91 x 31 nodes along x and y, respectively; a rigid lithospheric plate confined by two weak-bearings to allow the horizontal movement. Top, bottom and left side boundary conditions are set to free slip, while for the right-side a constant velocity gradient was defined.

Rock type	Width [km]	Thickness [km]	ρ [kg/m^3]	η [Pa s]
Rigid Lithospheric Plate	8400	100	2800	$3 \cdot 10^{24}$
Weak bearings	300 x 2	100	2700	$3 \cdot 10^{19}$
Upper mantle	9000	560	3300	$3 \cdot 10^{20}$
Lower mantle	9000	2340	4000	$1.5 \cdot 10^{22}$

Table 4.1: Main parameters defined for these numerical simulations.

$$\psi_{i,j} = \left[\psi_{i-1,j} + (vy_{i-1,j} \cdot dx)\right] + \left[\psi_{i,j-1} + (vx_{i,j-1} \cdot dy)\right] ; \qquad (4.10)$$

4.2 Results

Initially, through the kinematic model we focused on the effects of viscosity contrast between upper and lower mantle. While maintaining a constant upper-mantle viscosity (i.e. $\eta_{UM} = 3 \cdot 10^{20}\ Pa \cdot s$), it was increased that of the lower mantle through three steps (i.e. $\eta_{LM} = (1^{st})$

$1.5 \cdot 10^{22}\ Pa \cdot s$; $\eta_{LM} = (2^{nd})\ 3 \cdot 10^{22}\ Pa \cdot s$; $\eta_{LM} = (3^{rd})\ 4.5 \cdot 10^{22}\ Pa \cdot s$) in order to obtain a viscosity contrast of 50, 100 and 150. Subsequently, for each step compositional map with superimposed the stream functions distribution were defined; Figure 4.2 shows the results.

The three simulations have similar flow patterns: the mantle flows vertically downward along right boundary and starting from bottom side, it expands toward left with horizontal movement and the upward until it encounters the upper-lower mantle transition; finally, mantle flows are sharply deflected toward right dragging the upper plate toward the right boundary.

The most important thing of these three tests is the lateral expansion: the larger the viscosity contrast, the greater is the lateral expansion of the mantle flow activated by the movement imposed on the right boundary. The aspect ratios are 1.3, 1.6 and 1.8 respectively for viscosity contrast of 50, 100 and 150.

In addition to the variations in lateral expansion, the horizontal velocity also changes. Figure 4.2-B displays vertical profiles of horizontal velocity, taken at $x = 2.0$. Through these three profiles we can observe that, as the viscosity contrast increases, greater will be the horizontal velocity field along mantle section. Therefore, such an increase of the velocity field below the rigid lithospheric plate has a repercussion on the amount of the shear stress developed at the lower surface of rigid lithospheric plate. These variations of the velocity profiles occur because the counterflow toward right is concentrated in a layer (i.e. upper mantle) thinner than the lower mantle layer where the horizontal velocity gradient is distributed over a greater depth. At the end, however, the amount of material flowing towards the left into the lower mantle corresponds to

that flowing to the right within both the upper mantle and the rigid lithospheric plate. On the other hand, it is worth to note that these three vertical profiles also depend on the fixed horizontal position where they were taken (i.e. $x = 2.0$). Indeed, the larger the viscosity contrast, the greater is the width of the convective cell, therefore every vertical profile has selected innermost or outermost velocity field of the convective cell.

Following the same technique used in the Chapter 3, we have measured the shear stress and shear stress gradient on the base of the rigid lithospheric plate. As significant deformation affects the lateral weak-bearing disturbing the stress field, the profiles were confined in the range from 0.5 to 2.7; Figure 4.3 shows both shear stress and shear stress gradient profiles obtained.

The three shear stress profiles appear clear and well defined (Fig. 4.3-A); shear stress peak increases as the viscosity contrast rises. On the other hand, the shear stress gradient profiles (Fig. 4.3-B) show the peaks with a comparable absolute value, although with different horizontal position. Indeed, as viscosity contrast increases the shear stress peaks move toward left (see coloured arrows in the Figure 4.3-B). As already seen through the comparison of the stream functions distribution (Fig. 4.2-A), lateral expansion of mantle flow pattern induced by movement of right boundary is exclusively a function of the viscosity contrast. For this reason, we suggest that lateral translation of shear stress gradient peak is due to increase of the lower mantle viscosity, which produces a higher shear stress peak and a shift of the maximum value of the shear stress gradient. It is important to note that, with respect to the profiles obtained by the I2VIS code in Chapter 3, these profiles are quasi-devoid of a significant amount of opposite (i.e. negative) shear stress.

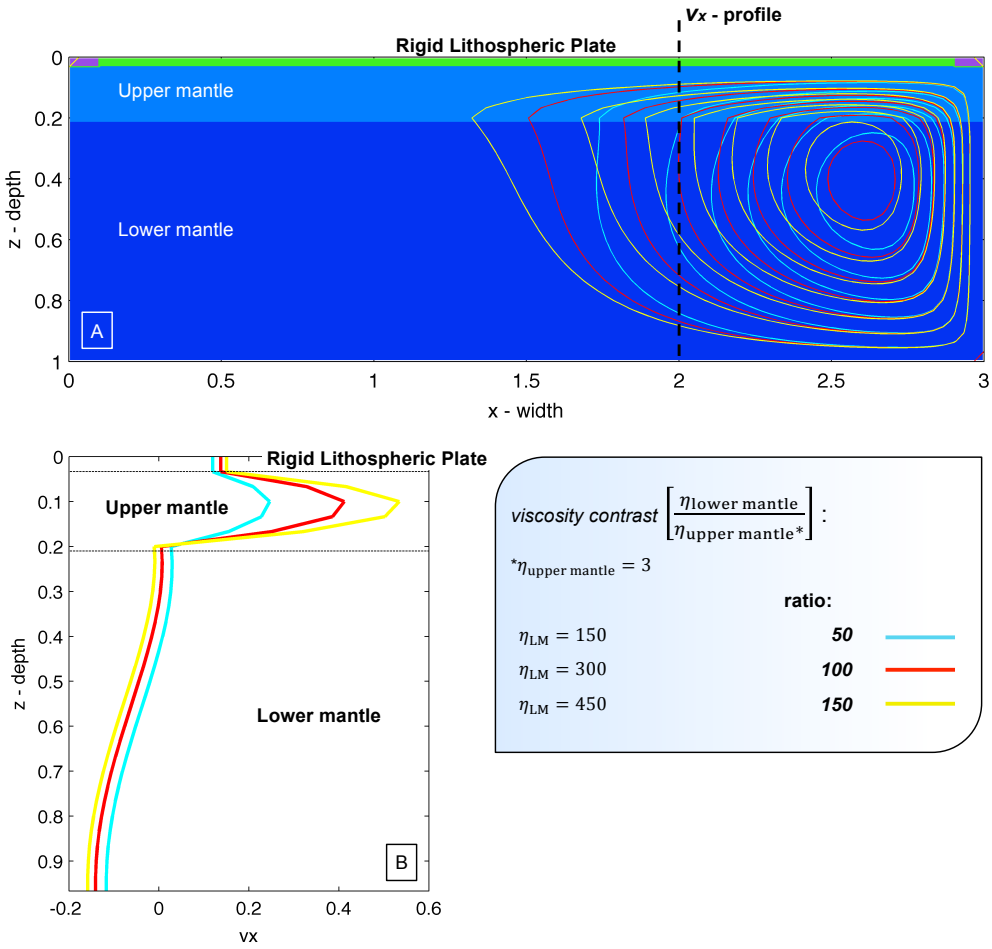

Figure 4.2: Kinematic-model. [A] Compositional map with superimposed stream functions of three different viscosity contrasts between upper and lower mantle (i.e. 50, cyan; 100, red; 150, yellow). The upper mantle viscosity is constant (i.e. $\eta_{UM} = 3 \cdot 10^{20}\ Pa \cdot s$), while lower mantle viscosity progressively is increased on the following values: $1.5 \cdot 10^{22}$, $3 \cdot 10^{22}$ and $4.5 \cdot 10^{22}\ Pa \cdot s$. Stream functions help to define the lateral expansion toward left of mantle flow pattern, which is a directly proportional function of the viscosity contrast. [B] Vertical profile of the horizontal velocity (Vx), taken to 2.0 along x-axis (Fig. 4.2-A, dashed black line). Similarly to the Figure 4.2-A, the three different colours define the viscosity ratio chosen (i.e. 50, cyan; 100, red; 150, yellow). Even if the velocity fields are similar on the lower mantle section, across upper mantle portion there are three different distributions that well-delineate the change in the horizontal velocity according to increase of the viscosity ratio.

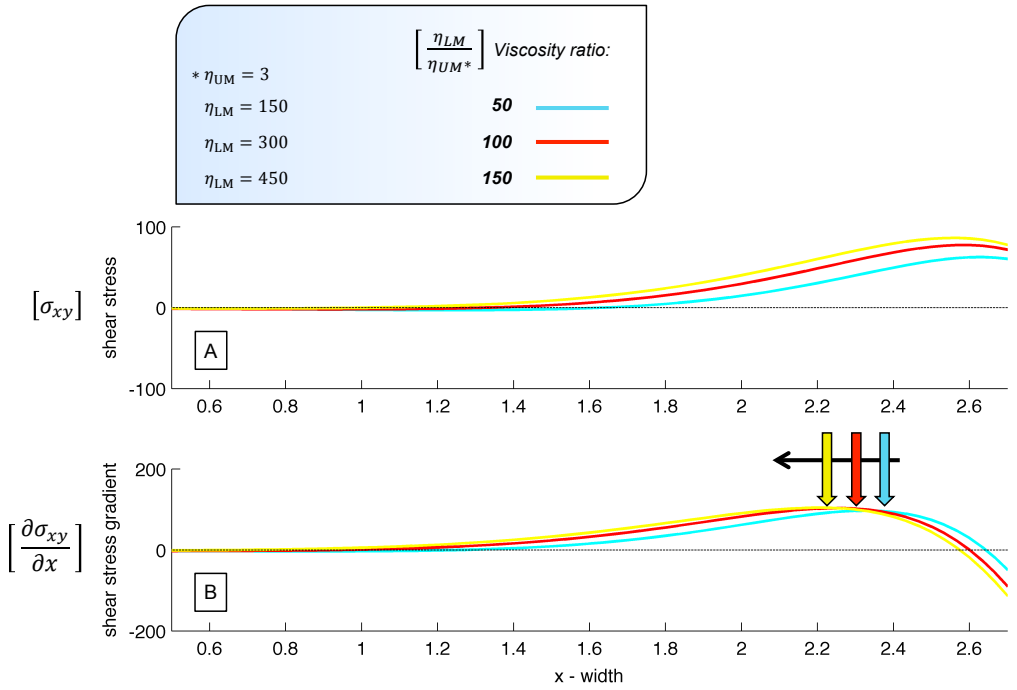

Figure 4.3: Shear stress and shear stress gradient profiles. These profiles are referred to the kinematic model and are taken along the lower surface of the rigid lithospheric plate. [A] Shear stress profiles on base of the viscosity contrasts initially setup; as viscosity contrast increase, greater is the shear stress peak. [B] Shear stress gradient computed by the same shear stress values of the previously figure. Although the peaks have the same absolute value, the horizontal position changed for more viscosity contrasts; coloured arrows lie at the corresponding peak value of the shear stress gradient.

We have interpreted this difference strictly connected with the fact that the SINDRICO code runs for only one timestep and, given that lateral displacement of the rigid lithospheric plate is confined, the response of the passive mantle drag is only partial.

Thanks to the results obtained via comparison of the three models with different viscosity contrasts, a certain relationship between the peak of the shear stress gradient beneath the rigid lithospheric plate and viscosity ratio among upper and lower mantle was highlighted. In order to understand that relationship, we have followed the same method previously used for three simple cases of viscosity contrast and through a

Viscosity ratio	*Distance* [Km]
1	200
2	200
3	1000
5	1200
10	1400
20	1600
40	1800
80	2100
100	2100
120	2200
150	2300
200	2400
400	2600
600	2700
800	2800
1000	2800
1200	2900
1400	2900
2000	3000

Table 4.2: Viscosity ratio between upper and lower mantle vs. distance among peaks of the shear stress gradient and right boundary of the model.

detailed and schematic assessment, it was possible to define how these two variables are related.

Starting from the same viscosity value (i.e. $\eta_{UM} = \eta_{LM} = 3 \cdot 10^{20}\ Pa \cdot s$) viscosity of the lower mantle is progressively increased in order to obtain a range of viscosity ratios from 1 to 2000. On the other hand, the peaks of shear stress gradient were measured from the distance to the right wall. Finally, to compare the results with I2VIS outputs, the horizontal distances have been converted to kilometres. Results, listed in table 4.2 and plotted in Figure 4.4, clearly define a correlation on logarithm scale.

Taking into account the relationship discovered through I2VIS simulations (Chapter 3), which related point of break-up (that corresponds to the peak of shear stress gradient) and trench position (cf. 3.12 Fig. chapter 3), we tried to see how these two trendlines are correlated in the

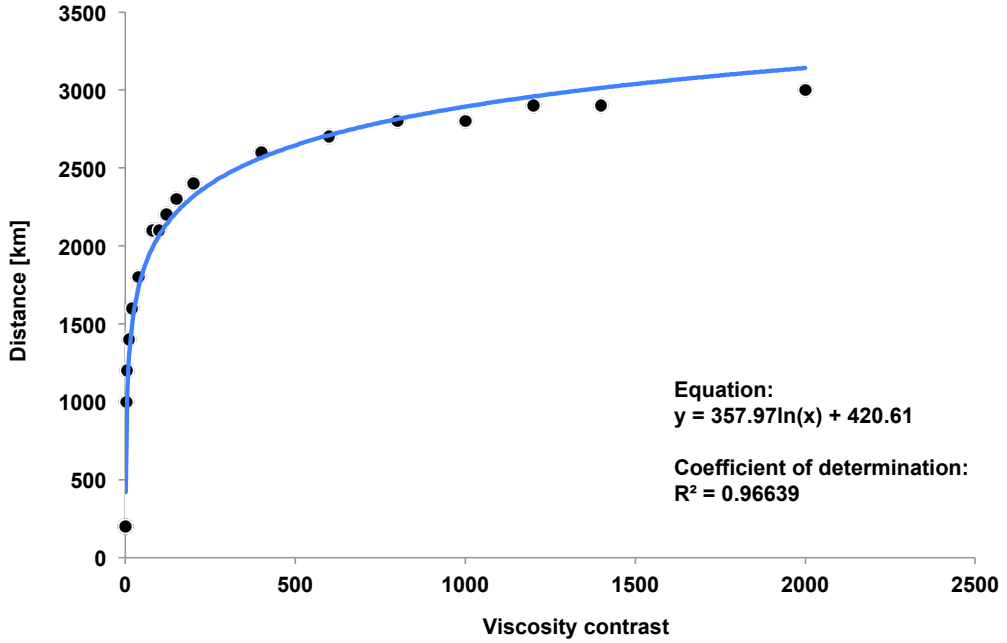

Figure 4.4: Scatterplot that relates the value summarized on Table 4.2. Blue-line is the trendline that shows a good-relationship of the two variables on logarithmic scale.

viscosity ratio range covered by the I2VIS simulations (i.e. from 20 to 150; cf. Fig. 4.5). In both cases the points follow a linear relationship and, surprisingly, the lines are nearly parallel to each other. However, there are 1323 km of vertical displacement between the two y-intercepts. We suggest that this displacement is strictly connected with dip-angle of subduction. Indeed, the simulations run with the SINDRICO code develop a mantle flow through a perfectly vertical movement of the right wall, while I2VIS simulations are characterized by more realistic subduction geometries, with slab dips varying from 30° to 90°. When the slab sinks into the lower mantle with an angle that differs from the vertical, the convective cell induced by subduction will have an aspect ratio that will depend on the viscosity contrast and, additionally, on the dip-angle of subduction. In this way, the dip-angle of subduction helps to grow

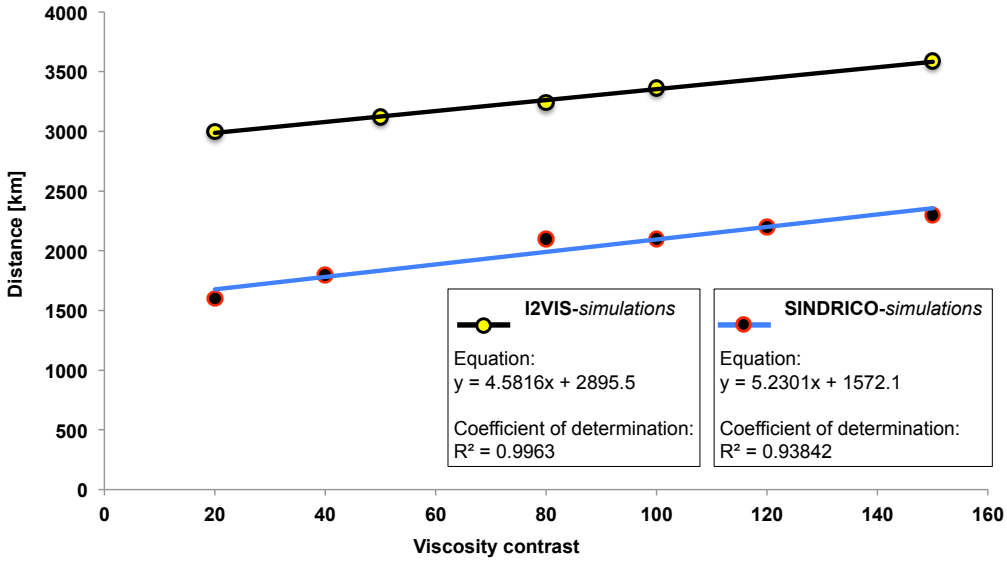

Figure 4.5: Scatterplot that relates both I2VIS and SINDRICO simulation. X-axis shows the viscosity contrast between upper and lower mantle. Y-axis describes the distance from the peak of shear stress gradient to trench (I2VIS) or to right boundary (SINDRICO).

the convective cell even more, by shifting the point in which mantle diverges beneath the continental flow and therefore the peak of shear stress gradient will be more away.

Chapter 5

Discussion

The aim of this study is to investigate how the subducting plates affect mantle flow patterns as well as how and to which extent the subduction-induced mantle flow may trigger the break-up and drifting of the continental plates on timescales similar to those suggested for the Earth. Realistic geometries and distributions of rheological properties at the lithosphere-scale were widely tested by means of two-dimension simulations. Through three different subduction styles (i.e. stagnant slab, slab avalanche and penetrating slab), it was possible to reproduce two scenarios of Earth's mantle convection, whole- and layered-convective system, which have a different impact on the continental plates due to the different size of the induced convective cells, that translates into different wavelength and shear stress magnitude of both active and passive mantle drag forces.

In this chapter we want to compare our results with geophysical measurements and geological observations from real convergent margins, to achieve a better understanding of the behaviour of the Earth's mantle and continental plates during the subduction processes and to put

constraints on the rheology of the lithosphere. The evolution of oceanic tectonic plates at the surface is well known from the analysis of magnetic patterns on the ocean floor, in combination with geological observations on overriding plates. However, the evolution of these plates after their subduction is much less well known and is only inferred indirectly from tomographic images of the present seismic structure of Earth's mantle and from numerical and laboratory experiments. For this reason, seismic tomography data and plates reconstruction are analysed here in order to compare our numerical outputs with real subductions as well as amount and rate of trench migration and the evolution of the continental plates both before and after the break-up. In particular, we have analysed the evolution of the oceanic Farallon plate beneath North America, of the Pacific plate beneath the Japan arc and the opening of the Western Mediterranean, in order to cover subduction cases that involve stagnant or penetrating subducting styles. It is important to note that the evolution of these convergent margins has been or still is characterized by subduction and retreat of a wide oceanic plate that was mostly accommodated by poloidal mantle flow in the inner portions of the subduction zone, and thus it is suitable for comparison with our 2D simulations.

Through our models presented here, a further step towards a geodynamic model of mantle convection consistent with global tectonic evolution of the past and present-day can be defined.

5.1 The subduction of the Farallon plate and westward drift of the North and South America plates

Since at least Cretaceous time, the western margin of North and South America has been a continuous convergent boundary where the Farallon plate subducted into the mantle (Seton *et al.* , 2012). After more than 100 million years of subduction, only small parts of the Farallon plate are still subducting below western North and South America today. The largest of these remnants are the Juan de Fuca, Cocos and Nazca plates, while the Pacific plate now borders most of the North American west coast. With the arrival of part of the Farallon ridge at the trench about 30 Ma ago, subduction was replaced by Pacific-North America transform motion (i.e., San Andreas fault system). This led to the formation of a window in the subducted slab (Dickinson & Snyder, 1979). The final stages of subduction were accompanied by a decreasing age of the subducting Farallon plate and decreasing subduction velocities (Stock & Hodges, 1989; Fig. 5.1).

According to the global plate reconstruction model of Seton *et al.* (2012), subduction of the Farallon plate started at ~170 Ma, when there was an accelerated growth of the Pacific plate at the expense of the Izanagi, Farallon and Phoenix plates. When the subduction occurred, the trench of the ~15000 km wide Farallon plate started to converge toward both North and South American Plates. Continental rifting followed by slow westward drifting of the North American plate relative to the Eurasian plate started at 200-180 Ma, with seafloor spreading appearing in the

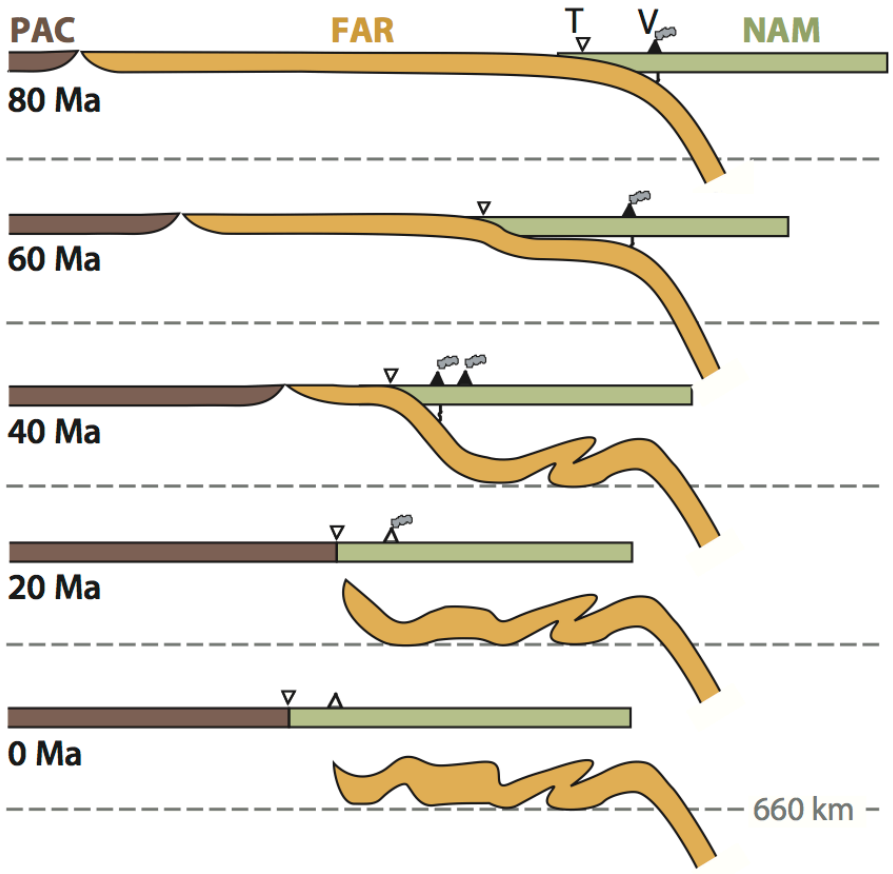

Figure 5.1: Schematic interpretation of the Farallon slab history to the south of Juan de Fuca plate. The sequence involves slab penetration into the lower mantle, slab stagnation above the 660 km discontinuity and slab detachment from the surface by ridge subduction. Today the remnant slab of the Farallon plate is stagnant in the transition zone, which is detached to the west from the Earth's surface but continues to the east down to the mid and lower mantle. PAC, Pacific plate; FAR, Farallon plate; NAM, North American plate; T, trench; V, volcanic arc. Reproduced from Schmid *et al.* (2002) and modified from Fukao *et al.* (2009).

central Atlantic at 180 Ma and only at ~80-60 Ma in the north Atlantic. Rifting in the southern South Atlantic initiated ~132 Ma and coincided with a peak of magmatism (Parana-Etendeka Large Igneous Province). Seafloor spreading then propagated northward and connected with seafloor spreading in the central Atlantic, yielding a continuous oceanic ridge by 120-110 Ma (Seton *et al.* , 2012).

Given its complexity and crucial role for the American plate evolution, the Farallon slab has been the subject of deep and multidisciplinary studies to understand the thermal state of the slab and the penetration depth into the Earth's mantle. Through three-dimensional kinematic thermal model, Schmid *et al.* (2002) have concluded that Farallon fragments that subducted since 50 to 60 Ma are still residing in the upper mantle and must be heavily deformed (cf. Fig. 5.1). The deformation of the slab in the transition zone is probably caused by the same mechanisms that were responsible for flat subduction around 60 Ma. In addition, a qualitative comparison of tomographic images with the plate tectonic history of the Farallon plate subducting beneath the North American plate has enabled rough estimates of which part of the subducted plate is at which position in the mantle today (e.g. Grand, 1994; van der Lee & Nolet, 1997).

Two high-resolution models of the P-wave and S-wave seismic structure of the mantle were derived independently by citedgrand1997global using different inversion techniques and different data sets. High-velocity anomalies in the mid-mantle are dominated by long, thin structures associated with the subduction of the Farallon Plate. The most likely interpretation is that these structures are slabs penetrating to at least 1600 km depth. In some regions there is evidence for downwelling to even

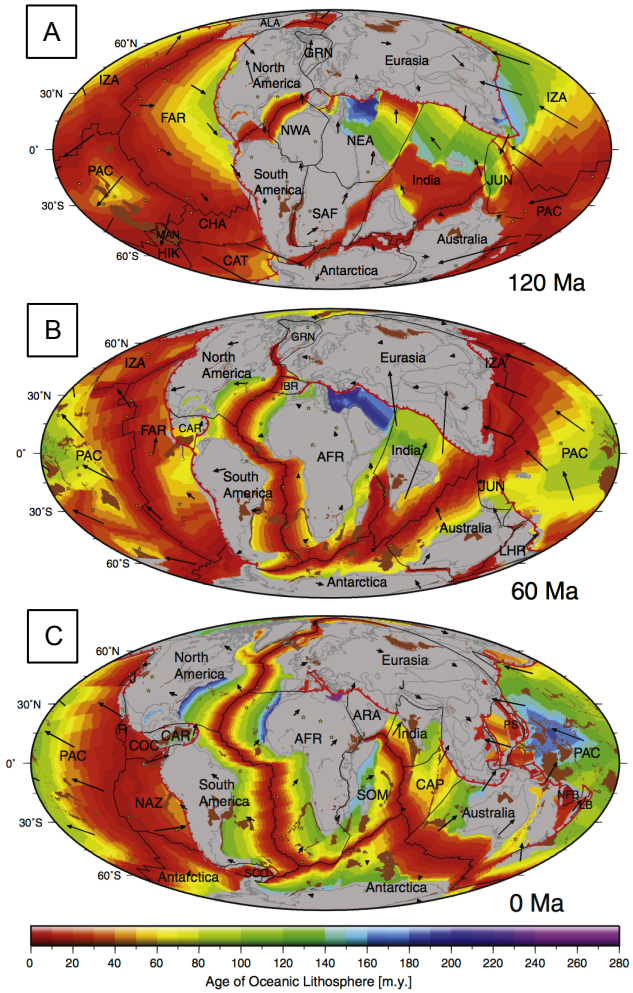

Figure 5.2: Global plate reconstructions from 120 Ma to the present day in 60 million year time intervals. Basemap shows the age-area distribution of oceanic lithosphere at the time of formation. Red lines denote subduction zones; black lines denote mid-ocean ridges and transform faults. Brown polygons indicate products of plume-related excessive volcanism. Yellow stars are present day hotspot locations. Absolute plate velocity vectors are denoted as black arrows. Additional abbreviations include: AFR = Africa, ALA = Alaska, ARA = Arabia, CAP = Capricorn, CAR = Caribbean, CAT = Catequil, COC = Cocos, FAR = Farallon, GRN = Greenland, IBR = Iberian plate, IZA = Izanagi, HIK = Hikurangi plate, J = Juan de Fuca, JUN = Junction, LHR = Lord Howe Rise plate, MAN = Manihiki, NAZ = Nazca, NFB = North Fiji Basin, NWA = Northwest Africa, PAC = Pacific; PS = Philippine Sea, R = Rivera/Guadalope, SAF = South Africa, SCO = Scotia Sea, LB = South Loyalty Basin, SOM = Somalia. From Seton *et al.* (2012)

greater depth.

To have a wider framework of the Farallon subduction, more recently Ren *et al.* (2007) have computed the past positions of both North and South American active margins for the last 120 Myr. In particular, through tomographic inversion of a large number of P and S wave traveltimes the geometries of the subducted plates were derived; finally they have used plate reconstructions to help identify the slab fragments in the tomographic model. Coloured lines on the Figure 5.3 represent past boundary positions between Pacific seafloor and American continents since 120 Myr and well show the trench retreat of both North and South American plates, which moved toward the northwest prior to ~70-80 Myr, and that more recently North America moved toward the west and South America toward the northwest. On the northern cross-section (path A-A'), the large anomaly dipping toward the west may be Juan de Fuca plate in the upper part and the Kula plate in its deeper part. Farther east, we may see the Farallon plate down to about 1700 km. The two cross sections farther south (paths B-B' and C-C') show the Kula and Farallon plates down to the Core-Mantle Boundary, with structural complexity in the upper mantle transition zone. In the section across Central America (path D-D') we infer the Farallon plate on the left and the Atlantic plate on the right. Finally, beneath South America (path E-E') we infer the Nazca/Farallon plate down to about 1500 km depth but not deeper.

Our simulations of both penetrating slab and slab avalanche are close fitting with geometries of high-velocity bodies given by seismic tomography data of the subducting Farallon plate beneath North American plate. Obviously, time of stagnation of the slab strongly depend from

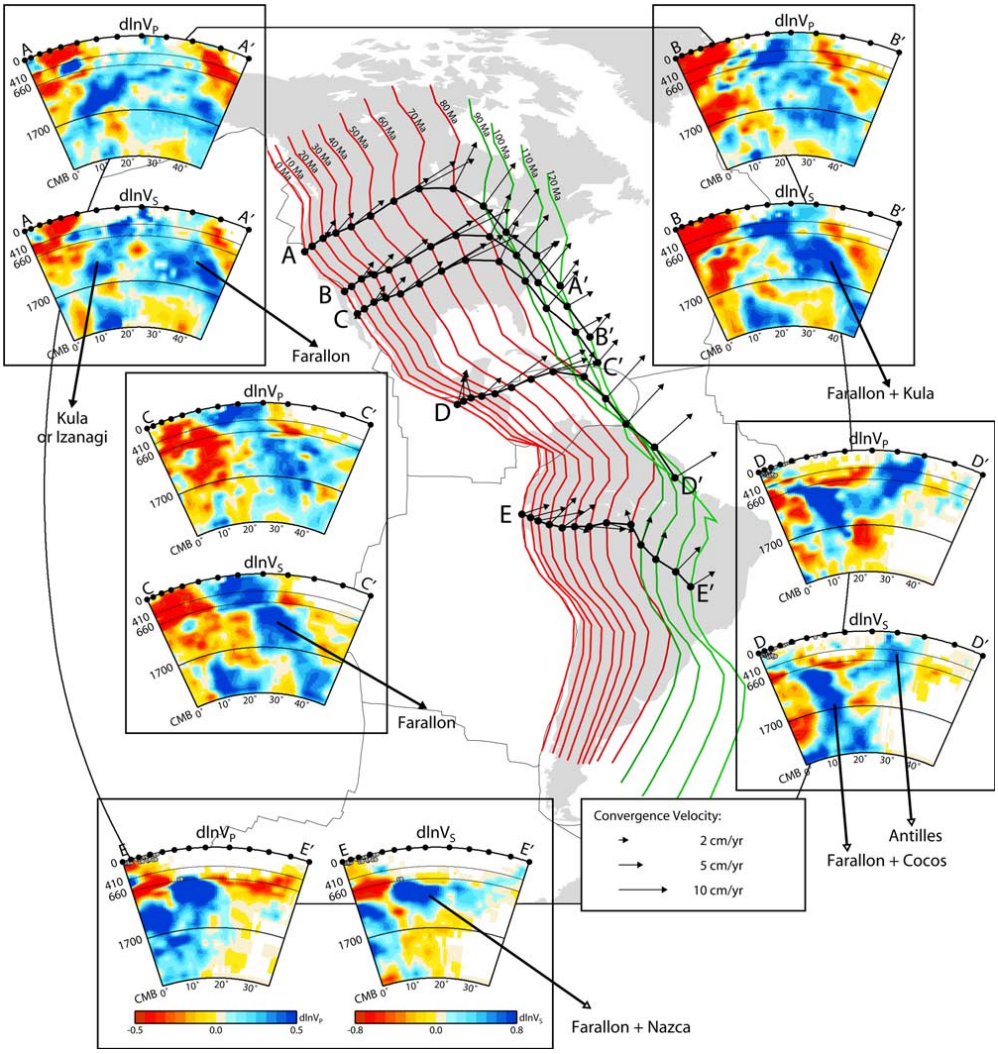

Figure 5.3: Cross sections through the model for P and S wave velocities. Red and green lines represent past boundary positions between Pacific seafloor and American continents since 120 Myr (computed from present boundary positions with rotation poles data in the hot spots reference frame). Black lines represent different cross sections made in our VP and VS models; different points along the lines represent past margin positions between 120 Myr and 0 Myr ago for given points in the present-day. Arrows represent velocities and directions of convergence at different ages, computed in the hot spots reference frame. From Ren *et al.* (2007).

many physical parameters, such as thermal state (function of the slab age and sinking velocity) and amount of slab-pull force, which is opposed to penetration resistance when the slab bends horizontally in the transitional zone (Forsyth & Uyeda, 1975).

According to our models, the transient stagnation-phase of the slab before sinking into the lower mantle produces two distinct mantle flow regimes that impact differently on the continental plate; if on the one hand, slab sinks into the upper mantle during early phase, mantle flow induced by descending lithosphere responds with a layered convective system. On the other hand, when the slab penetrates into the lower mantle, the entire Earth's mantle flows forming a whole convective system. North American seismic tomography images (cf. Fig. 5.3, path B-B') and the schematic interpretation of the Farallon Plate subduction in Figure 5.1 describe the Farallon slab as stagnant in the transition zone, which is detached to the west from the Earth's surface but continues to the east down to the mid and lower mantle. It is likely that an involvement of each layered- and whole-convective system may occurred as the slab is recycled into the mantle. Indeed, the continuity of long, narrow high-velocity zones from the upper mantle to depths in excess of 1500 km in regions of ancient subduction is a convincing evidence for large-scale mantle flow of subducted slabs into the deep mantle (Grand *et al.* , 1997). Assuming that the mid-mantle fast anomalies are slabs implies that, upon reaching about 700 km depth, slabs sink nearly vertically through the lower mantle. Using these results and plate reconstructions, one can estimate slab-sinking rates.

According to our reference models of penetrating-slab, more than 33 Ma of subduction are initially spent for sinking both into the upper and

lower mantle, without triggering any continental break-up. During this phase, we have measured an amount of trench retreat and drift of the entire continent higher than ~1000 km. Although the passive mantle drag (F_{PD}) opposes the motion given by slab rollback, the combined effects of active mantle drag (F_{AD}) and trench suction (F_{TS}) pull the continental lithosphere trenchward. When the break-up happens, the drifting-phase is able to drag the coupling continent with the subducting plate for more than 2000-3000 km. Of course the length of the oceanic plate available to subduct defines the amount of trench retreat. For example, during the subduction of the Farallon plate beneath the North-American Plates, with the arrival of the mid-ocean ridge at the trench as of 30 Ma, the subduction was accompanied by a decreasing of the subduction velocities (Stock & Hodges, 1989). Figure 5.3, taken from Ren *et al.* (2007) shows past convergence margins as a function of time in a hotspot reference frame. Note that in the past, the Farallon plate was subducting farther east and that the current trench position is similar to that of 30 Ma. Such evidence suggests that the subduction has played a crucial role in regulating both the amount and the rate of the continental drift. Considering that the appearance of large igneous provinces coincided with continental rifting phases, mantle plumes underplating beneath the present-day Atlantic Ocean likely favoured continental break-up and the establishment of seafloor spreading of the Atlantic rift. Nevertheless, we suggest that the retreat and mantle flow induced by subduction of the Farallon plate were crucial in driving the drift-phase of North and South American plates.

It is important to keep in mind that, although the two-dimensional seismic tomography data presented so far constitute one of the most am-

bitious models ever built to obtain understandable resolutions of the Earth's mantle on global scale, there are still some gaps in data coverage, but the ability to produce independent models that agree in such detail for large volumes of the mantle marks a milestone in imaging the effects of dynamic processes in the earth (Grand *et al.* , 1997). At present-day, seismic tomography data show still gaps in the understanding of the subducted slab within the lower mantle, such as how slabs continue to the Core-Mantle Boundary, or the cause for the apparent difference in P and S velocity structure in the deepest mantle.

5.2 Japan arc

In Japan, thousands of islands are arranged in several arc-shaped chains. The Japanese Islands are emerged parts of volcanic island arcs, extending for about 3000 km. From the geodynamic point of view, the Japanese Islands lie at the junction of four major tectonic plates: the Pacific and the Philippine Sea oceanic plates and the North American and the Eurasian continental plates. The Pacific Plate moves towards the WNW at a rate of about 8-10 cm/year and is subducted beneath the Kuril arc, Japan arc and the Izu-Bonin arc (Fig. 5.4). The current outline of the Japanese Islands took shape during the period between 30 Ma and 15-14 Ma, accompanied by the spreading of the Japan Sea. The present rate and pattern of movement of the major plates established around 2 Ma.

A distinct picture of the tectonic history of the Japanese Islands can be traced back for about 30 Ma, although the geological history, as reflected by the presence of much older rocks, clearly extends much further back in time. The four main steps of the tectonic evolution can be summa-

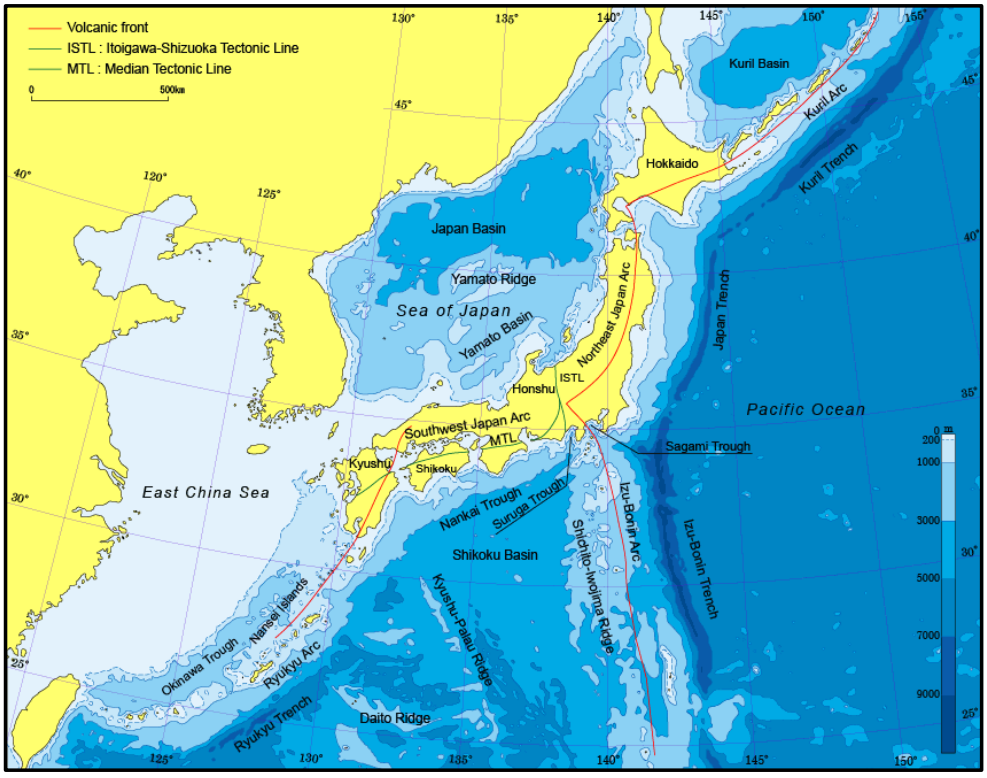

Figure 5.4: Topographic map around the Japan arc. The Japanese Islands consist of three main island arcs, in the order from the north: the Kuril arc, Japan arc and the Izu-Bonin, which have the corresponding trenches toward Pacific plate side that subduct towards the WNW at a rate of about 8-10 cm/year. From GLGArcs.net.

rized as follow:

- **30 Ma -** Start of an amagmatic rifting-phase at the eastern margin of the Eurasian Plate. Before spreading of the Japan Sea was initiated, the Japanese Islands were attached to the coastal region of the eastern margin of the Eurasian continent. At the same time, the Pacific Plate was moving towards the WNW (Jolivet *et al.* , 1994b).

- **20 Ma -** Start of spreading of the Japan Sea, the Kuril Basin and the Shikoku Basin, along with anti-clockwise rotation of the NE Japan

arc.

- **15-14 Ma -** Completion of rotation of NE and SW Japan arcs, spreading of the Japan Sea, the Kuril Basin and the Shikoku Basin, and start of the Izu-Bonin arc collision. Subsequent to rotation of the NE Japan arc, the SW Japan arc began to rotate clockwise (Jolivet *et al.* , 1994b). The subduction zone of the Pacific Plate was located in almost its present location by around 17 Ma.

- **1.8 Ma-present-day -** Start of collision of the Kuril fore-arc, tectonic events at the eastern margin of the Japan Sea, spreading of the Okinawa Trough and Izu-Bonin Back-arc Basins. Along the eastern margin of the Japan Sea, the Eurasian Plate began to form a convergent boundary against NE Japan (i.e. North American Plate).

The Euler poles data were used from Miller & Kennett (2006) in to reconstruct the position of the plates back to the late Miocene (Figure 5.5). The interpreted motions of the plates in northwest Pacific are consistent with recent tectonics, geologic data, and interpreted slab morphology from tomographic images.

Near-horizontal deflection of subducted slab was first detected from a traveltime analysis by Okino *et al.* (1989) and imaged in the transition zone beneath Japan by van der Hilst & Seno (1993) and Fukao *et al.* (1992), through their P-wave traveltime tomography. From these studies, they started to refer to slabs with this tendency as 'stagnant slabs'. Wide review recently proposed from Fukao *et al.* (2009) suggests that

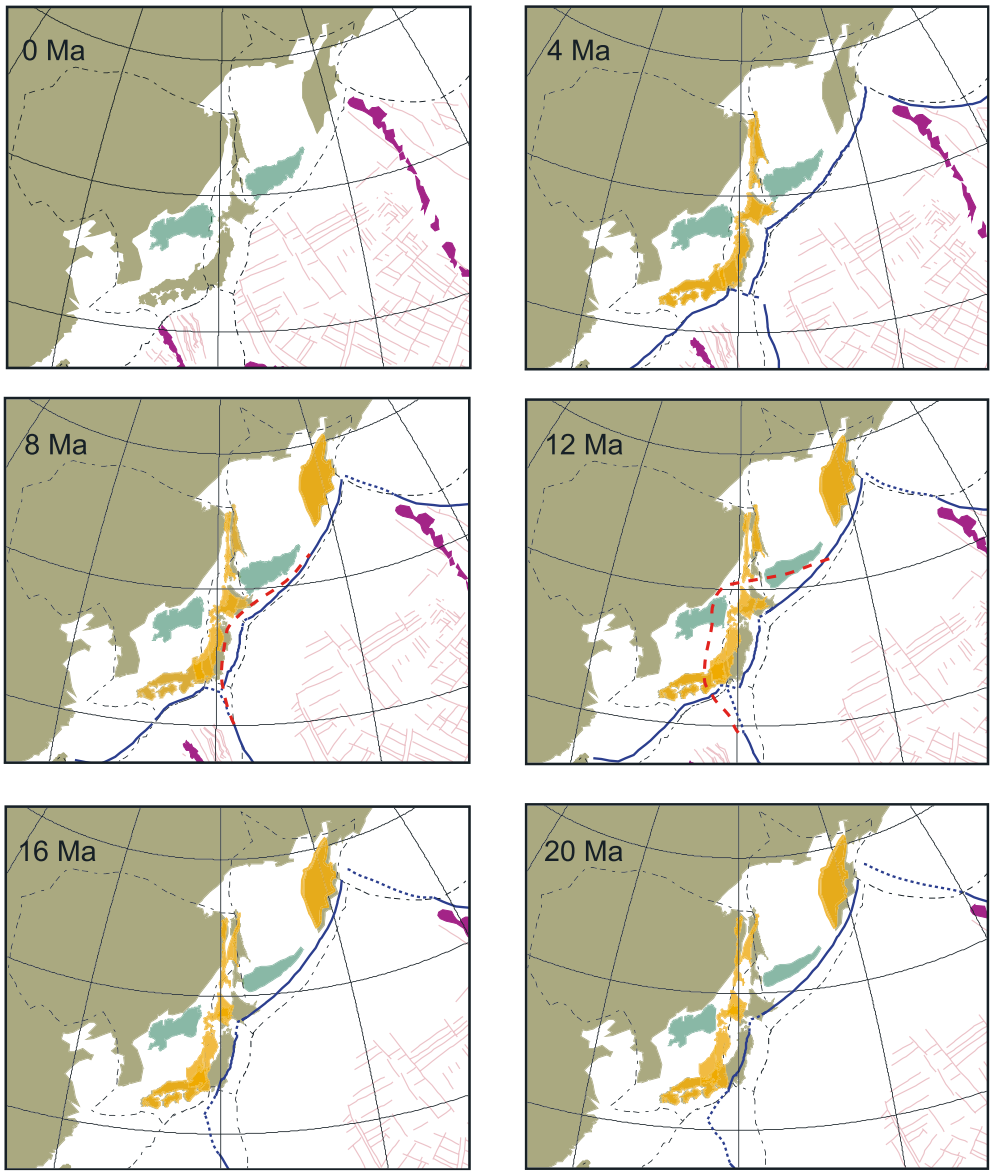

Figure 5.5: Paleogeographic reconstruction of the northwest Pacific from the mid-Miocene based on new slip vector based Euler poles. Current coastlines are grey, paleogeographic coastlines are orange, pink lines are magnetic anomalies, blue lines are interpreted paleoplate boundaries with dashed portions for the inferred extensions, green objects are basins, and purple objects are oceanic plateaus or aseismic ridges. The thick red dashed lines are the interpreted paleoboundaries for depths of 220 and 520 km, which represent the maximum extend of plausible rollback of the Pacific plate for these ages. Note that the Ryukyu arc is not shown for 16 and 20 Ma because there are no evidence of a subducted slab corresponding to that age/depth. From Miller & Kennett (2006).

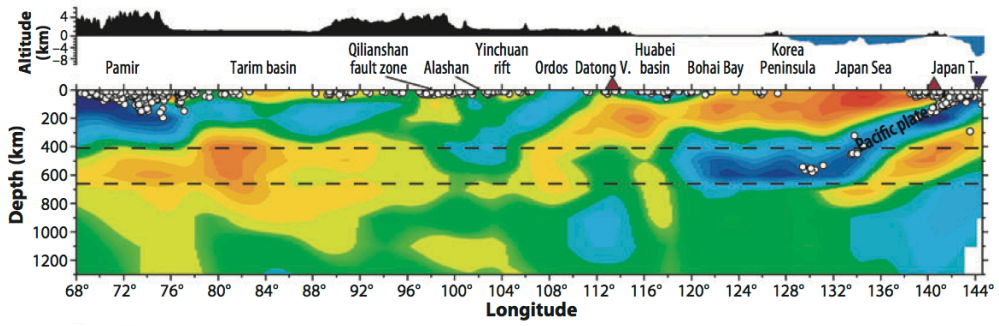

Figure 5.6: Figure shows the east-west vertical cross section of P-wave velocity perturbations along latitude 39°. Starting from right side, fast anomalies associated with the subducted slab is well-defined, which is sharply deflected to horizontal when it hits the bottom of the upper mantle. The uppermost mantle above slab-deflected is significantly slow and lies beneath the Japan Sea. Altitude profile highlights low topographic points given by Japan Trench and seafloor of the Japan Sea, with a high-altitude point in the Japan Sea that corresponds to Japan arc. From Fukao *et al.* (2009).

the subduction of the Pacific plate at Japan Trench is an evident-case of stagnant slab (cf. Fig. 5.6). The horizontal slab extends over a distance of 800 to 1000 km in the transition zone along the 660 km discontinuity. On the other hand, the uppermost mantle is significantly slow not only directly above the inclined Wadati-Benioff zone but also below the Asian continent, all the way above the horizontally deflected slab. Lei & Zhao (2005) and Huang & Zhao (2006) called this extensive low-velocity zone a 'big wedge mantle' and emphasized its significance on surface tectonics, including intraplate seismicity and volcanism in eastern China.

Our stagnating slab model display several similarities with the evolution of the Japan arc. Indeed, the reference models show fragmentation and drifting of a microcontinent that has dimension similar to those suggested for Japan arc. Evolution of stagnant-slab subduction below continental plate occurs on shortest timescales and leads to the immediate effects of break-up. Each stagnant-slab models proposed here have in common two crucial episodes: (1) active mantle drag given by sink-

ing of the subducting plate is activated from the beginning, but mantle flow sharply decreases as soon as the slab reaches the transition zone. On the other hand, (2) slab retreat characterizes the second episode because when the slab bending occurs above lower mantle, slab retreat and drifting of the microcontinent are promoted. If the break-up does not occur during first episode, our simulations do not recorded any fragmentation. We suggest that these models include some shortcomings, the most important is given by 2-D setup that limited the real mantle flow that commonly develops during this processes.

5.3 Calabrian arc: the Ionian subduction

The present geodynamic state of the Alpine Mediterranean region is inherited from its past history. Continental collision has been part of geodynamic analyses of the Mediterranean for many decades (e.g. Argand, 1924), although originally in the context of the Africa-Europe collision in the Alps. On the other hand, essential studies have been conducted to understand the extensional geodynamic setting that led to the present-day configuration. Among these, Alvarez (1974) have proposed the reconstruction of the positions of Western-Mediterranean micro-plates in the Oligocene that led to recognize a formerly continuous Alpine orogenic belt. They have documented four episodes of movements that fragmented from Miocene to Quaternary the Alpine belt: (1) first episode involved the initial rotation of the Corsica-Sardinia-Calabria micro-plates (Oligocene). (2) The second episode took place in the early Burdigalian, when Corsica was unable to rotate further and Sardinia-Calabria microplate broke away from Corsica and continued to rotate, forming the rest

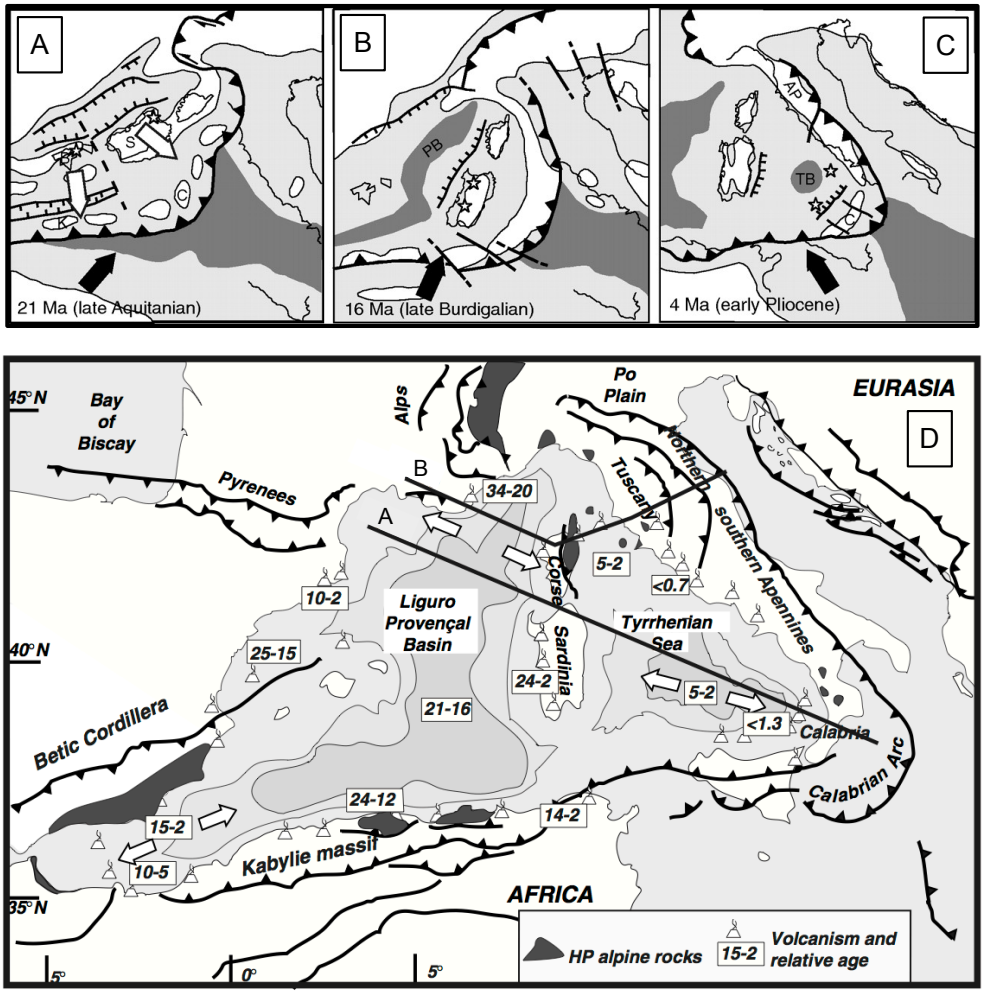

Figure 5.7: Schematic reconstruction of paleotectonic structures and present-day geodynamic setting of the Western-Mediterranean. [A-B-C] paleogeographic sketch maps for the Western-Central Mediterranean. AP-Apennines; B-Balearic Islands; C-Calabria; K-Kabilides; PB-Provencal Basin; S-Sardinia; TB-Tyrrhenian Basin (from Cavazza & Barone, 2010). [D] Tectonic map of the central Mediterranean simplified. Shown are the distribution of HP alpine metamorphism, the average ages and the distribution of volcanism. Are also indicated are profiles A and B, along which we reconstruct the extensional geological record (cf. Fig. 5.8). From Faccenna *et al.* (2001).

of Ligurian Sea. (3) After collision with Tunisia the Sardinian part of the drifting micro-plate was no longer free to move and the third episode began with separation of Calabria from Sardinia (Middle Miocene). (4) Finally, from Pliocene to the recent, with Calabria moving ESE to its present position; the three snapshots (A, B and C) in Figure 5.7 (from Faccenna *et al.* (2001)) schematically summarize this sequence.

Although many authors well described the extensional setting occurred in Provençal and Tyrrhenian Basin, none of them have satisfactorily explained the dynamic relationship between extension in the Tyrrhenian and compression in the Apennines. Malinverno & Ryan (1986) first have suggested a model that explains both extensional and shortening around Apennines area, as result of arc migration driven by sinking of the lithosphere. In a subduction system like the present-day Central-Western Mediterranean, where the trench migrates outward due to a sinking of the underthrusting plate, the formation of the back-arc and/or internal basin (i.e. Provençal and Tyrrhenian Basin) takes place if the motion of the overriding plate does not compensate for the retreat of the subduction zone. More recently, Carminati *et al.* (2012) have published a geodynamic reconstruction of the Central-Western Mediterranean and neighbouring areas during the last 50 Ma, including tectonic observations. They emphasize how different styles of evolution have interested this area during both Alpine and Appenninic subduction. If the subduction zone has a double vergent subduction hinge that moves towards the upper plate (i.e., Alps), higher elevation and deeper decollements affect the continental plate; on the other hand, if the subduction zone together with the subduction hinge migrates away from the upper plate (i.e., Apennines), a back-arc basin occurs. Finally, it is worth to comment

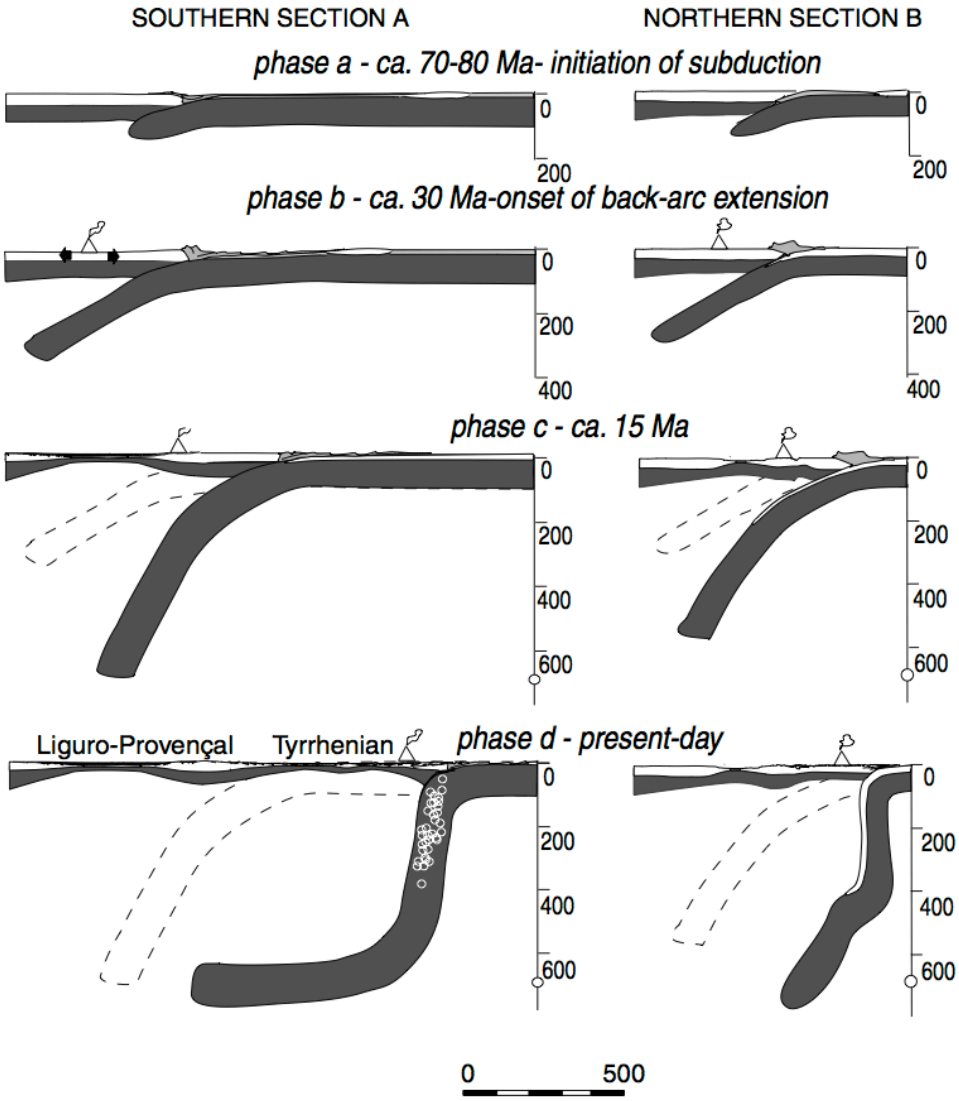

Figure 5.8: Four-phase reconstruction of the subduction process along the cross-sections A and B (cf. Fig. 5.7-D). Tectonic reconstruction of subduction and back-arc extension in the Mediterranean; from Faccenna *et al.* (2001).

the contribution given by Jolivet & Faccenna (2000), which have further advanced the understanding of the regional evolution by pointing out the contemporaneity of the start of the extension in the Mediterranean and the role of the decrease in absolute velocity of the African plate in causing acceleration in slab retreat. Figure 5.8 show the reconstruction of the evolution process along the two cross-sections A and B (cf. Fig. 5.7-D), from Faccenna *et al.* (2001). As convergence is considered negligible, the amount of back-arc extension shown is directly related to the amount of subduction. Phases b and c in Fig. 5.8 show the slab configuration at the beginning of the Tyrrhenian and Liguro-Provençal rifting, respectively. Note that the deep dip of the slab during phase c is only inferred. A crucial study of the upper mantle P wave velocity structure below Mediterranean area through the seismic travel time tomography was developed by Piromallo & Morelli (2003), down to 1000 km depth. Main results indicate that the mantle dynamics of Western-Central Europe is dominated by blockage of subducted slabs at the 660 km discontinuity and ponding of seismically fast material in the transition zone. In particular, cross section 'E-e' (cf. Fig. 5.9) shows below the Calabrian arc a high velocity structure, lying horizontal in the Ionian domain, steeply dipping to the NW in the mantle and then bending to almost horizontal in the transition zone. A pronounced shallow slow anomaly is detected on the Tyrrhenian side, in correspondence of the back arc region, interpreted as the evidence of an asthenospheric wedge (Mele *et al.* , 1998). While in the Calabrian portion the subducted lithosphere is imaged with continuity by the vast majority of tomographic models (e.g. Piromallo & Morelli, 2003), vertical continuity of the slab in its shallow portion below the Apenninic belt is instead a point of dis-

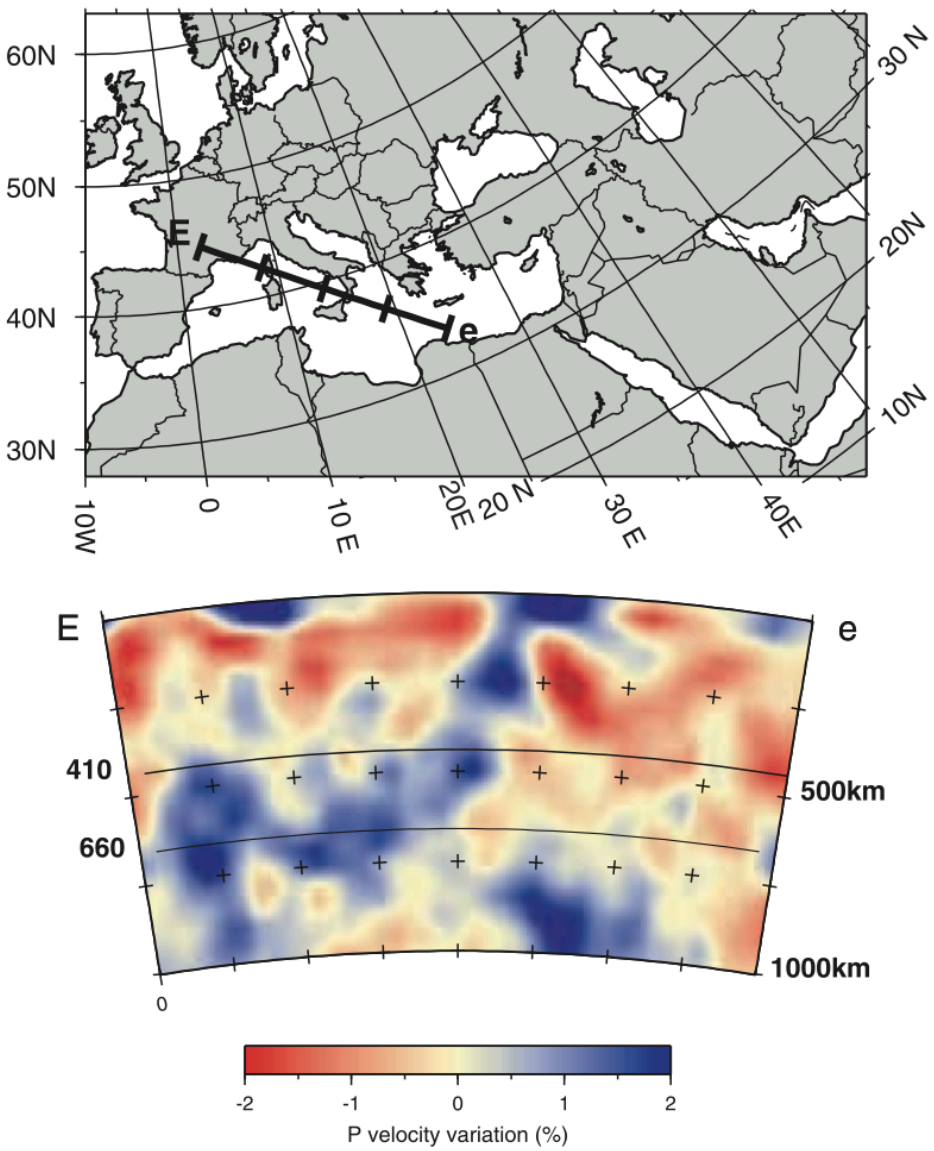

Figure 5.9: Cross section extrapolated from Piromallo & Morelli (2003). The top map illustrates the section location. Cross section has the length of approximately 20° along a great circle and its vertical extent reaches the bottom of the model. Ticks along the line segment indicate the distance from the extremities by 5° intervals. The 410 and 660 km discontinuities are indicated as thin and thick lines, respectively. Cross section 'Ee' shows a high velocity anomaly on the Ionian side of the Calabrian arc connected to the fast structure steeply dipping below the arc into the mantle and bending horizontally in the transition zone.

crepancy.

Unlike the Japan arc, the surrounding regions the Western-Mediterranean reflected a complex geodynamic setting active in this area. Alpine orogeny, the multifragmentation of the Corsica-Sardinia-Calabria micro-plates as well as the geographic closeness between lithospheric thinning given by slab retreat and continental shortening on the Adriatic side due to Apennine orogeny are some of the many aspects that make this area unique. Nonetheless, a clear and fundamental aspect can be taken into account: if trenches move away from the upper plate (i.e. slab rollback; (e.g. Dewey *et al.* , 1989)) large-scale extension produces thinning and stretching of the upper plate and/or of the previously accreted units (Jolivet *et al.* , 1994a). Although our two-dimensional models cannot reproduce the rotation of the Corsica-Sardinia-Calabria micro-plates, continental multifragmentation can be modelled using intraplate weak-zones. Through this technique, regimes of localized deformation may be reproduced leading to the break-up of microcontinents. This might imply that pre-existing zones of weakness were present in the southern margin of the European continent, favouring the subsequent break-up. Nevertheless, what matters is that when stagnant-slab subduction occurs, the wavelength of the active mantle drag is limited and therefore the microcontinent affected by break-up does not exceed ~500 km length.

Chapter 6

Conclusions

The principal goal of this thesis has been to shed light on the role of subducting plates in the dynamic evolution of the Earth's mantle and its surface expressions associated with deformation and motion of continental plates. This has been done by investigating the coupled dynamics of mantle convection, plate tectonics, continental break-up and drift with large-scale numerical models. The research presented in the different chapters of this thesis revealed a number of interesting observations, which have not been made before and gives new insight into some unresolved questions of geodynamics.

We have systematically studied the influences of the subduction processes, either characterized by stagnant or penetrating slab regime on the continental break-up and subsequent drifting. The most important results indicated that:

1. Three different styles of subduction can be defined by increasing the viscosity contrast between upper and lower mantle: penetrating slab, slab avalanche and stagnant slab.

2. The subduction of the oceanic plate induces a poloidal mantle flow that propagates on the base of the upper plate. The aspect ratio (width/height) of the induced poloidal cell depends on the viscosity contrast among upper and lower mantle.

3. The active mantle drag (F_{AD}) generated by the poloidal mantle flow is counterbalanced by passive mantle drag (F_{PD}) away from it and therefore a distensive tectonic regime affects the continental plate. According to the Newton's third law (i.e. action-reaction principle), tension (T) developed within the continental plate has a magnitude equal to $min(F_{AD}, F_{PD})$, while the difference between active and passive mantle drag determines the direction of plate drifting.

4. The stagnant slab subduction style develops a low active mantle drag (F_{AD}) and therefore the break-up does not always occur, unless a relatively low yield strength of the overriding plate is initially imposed. This may explain why the back-arc basins do not always occur.

5. Our shear stress profiles indicate that the break-up may occur where the basal shear stress gradient peaks. The distance that separates the trench and the break-up point depends on the convection style and, in case of whole-mantle convection, on the viscosity contrast between the upper and the lower mantle.

6. If the break-up occurs, the drifting-phase is driven by combined effects supplied from the active mantle drag (F_{AD}) and the trench suction force (F_{TS}), which maintain the trench-side continent coupled with the subducting plate, even when a consistent trench re-

treat takes place.

7. Relatively simpler two-dimensional simulations carried through the SINDRICO code have highlighted even more how the dimension of the convective cell depends on the viscosity contrast between the upper and lower mantle. The direct consequence of such a growth of the convective cell is that the peak of the shear stress gradient shifts more away from the right boundary. Additionally, a linear relationship between the viscosity contrast (from 20 to 150) and the distance between the peak of the shear stress gradient and the right boundary has been systematically defined.

8. Yield strength profiles and integrated strength computed by the YSE_1D code have helped us to predict if the continental break-up can occur or not for different input parameters. By comparing the tension (T) and the integrated strength (B) it was possible to verify if the continental break-up may occur or not (cf. Table 3.4).

9. It was found that, if the subduction develops a consistent trench retreat, the break-up occurs although the tension (T = 1.46 $\cdot$ 10^{13} N/m for the penetrating slab or T = 0.04 $\cdot$ 10^{13} N/m for the stagnant slab) is less than the corresponding integrated strength (B = 1.99 $\cdot$ 10^{13} N/m or B = 0.37 $\cdot$ 10^{13} N/m, respectively). In these cases, we suggest that the trench suction force (F_{TS}) provides an additional force to activate the continental break-up, which approximately may be equal to the difference between the tension and the integrated strength (F_{TS} = B - T = 0.53 $\cdot$ 10^{13} N/m and F_{TS} = 0.33 $\cdot$ 10^{13} N/m for the penetrating and the stagnant slab, respectively).

Finally, good correspondences between our models and the evolution of real ocean-continent convergent margins suggest a new interpretation of the break-up and drifting mechanisms for some continental plates, such as the North and South American plates, Calabria-Sardinia-Corsica micro-plates and the Japan arc.

6.1 Future research directions

The research presented in this thesis is a further step toward a consistent geodynamic model of the mantle convection that includes P-T dependent physical properties of the media and phase transition. However, only a limited number of aspects and effects related to continental break-up and drift could be explored throughout this project. This last section will propose some possibilities for future research, focussing on the improved evaluation of results by comparison to observations and improvements of the physical/numerical model itself.

- **Numerical implementations:** the principal aspects studied in this thesis can be addressed by the current version of the I2VIS code. However, the quality and robustness of the obtained results is likely to be improved by advancing the underlying physical model. Among these, partial melt generation can be implemented into the numerical code to understand how and to which extent partial melting processes can weaken the continental plates up to trigger the break-up. On the other hand, more realistic thermal structure of the oceanic plate as well as growth of mid-ocean ridge can be set through some numerical assumptions. In any case, future models will incorporate more and more of these complexities in order to

approximate the Earth's conditions as close as possible.

- **3-D approach:** three-dimensional modeling of the different subduction styles seen in this thesis is a next important step. The geodynamics of 2-D numerical modeling is limited to investigate the mantle flow pattern, although it highlights the crucial aspects initially considered in this thesis and it is representative of the inner portions of subduction zone where the poloidal component of the mantle flow is predominant. However, the induced mantle flow, which is the crucial agent to trigger the break-up and drifting of continental plates, is a three-dimensional process. To fully understand how and to which extent the mantle flow evolves under tectonic plates is necessary to conduct a further 3-D modeling investigation to see how mantle flow acts laterally. Following this 3-D approach, the knowledge of the interactions between the poloidal and the toroidal mantle flow and of how these two different mantle flows affect the break-up and drift mechanisms can be improved.

- **Towards constraining the mantle flow:** the evaluation of numerical models of large-scale tectonics is often difficult as these processes are very complexes, while the observations are limited to the present-day and often fragmentary. However, current geological observations can be used to constrain the dynamic and rheological parameters of the Earth's mantle, in order to develop more realistic mantle convection models. For example the dynamics of the subduction processes can be indirectly constrained by study-

ing the induced mantle flow. Recently, towards this approach some innovative and complex numerical models have been developed, which simulate the seismic anisotropy given by intrinsically anisotropic minerals to understand how the mantle flow pattern evolves around the subduction zones (e.g. Faccenda & Capitanio, 2013; Faccenda, 2014a).

- **Do not forget a simplistic approach:** it is right to continue to built and develop numerical codes more and more complex toward a robust modeling of the geodynamic processes, but is equally correct to maintain a simplified approach (e.g. SINDRICO code), especially when we want to focus on certain physical aspects. Further advances in 2-D modeling should be addressed towards this simple type of models through high-resolution simulations, from which we can get even more consistent results.

Appendix A

YSE 1D

```
% APPENDIX A ============================================== YSE_1D
%
% Luca Dal Zilio(1), Manuele Faccenda(1,2), Fabio A. Capitanio(2)
% (1) University of Padua, Department of Geosciences
% (2) Monash University, School of Geosciences
% _____________________________________________________________
% SUBDUCTION-INDUCED BREAK-UP AND DRIFTING OF CONTINENTAL PLATES
%
% 1-D STRENGTH ENVELOPE
%================================================
clc
clear all;
close all;
display('1-D STRENGTH ENVELOPE')
%================================================
% turn on // turn off         1 == on || 0 == off
%================================================
if 1==1
    on = 1;
end
if 0==0
    off = 0;
end
printmod                            =  on;
temp_celsius                        =  on;
heat_conservation_eq_implicit_method =  off;
half_space_cooling_model            =  on;
continental_geotherm                =  off;
Von_mises_criterion                 =  off;
Von_mises_value                     =  300e+6;
%================================================
% parameters
%================================================
g                       = 9.81;                 % Gravitational Acc. [m/s2 ]
Strainrate              = 1e-14;                % [1/s] Background strain rate
```

```
TopTemperature          = 273;                  % [K]
BottomTemperature       = 1600;                 % [K]
Thick_Crust             = 32e+3;                % [m] reference model: 32 km
Thick_Lithos            = 44e+3;                % [m] reference model: 44 km;
ThickModel              = Thick_Crust+Thick_Lithos;
%================================================
% other definitions
%================================================
n                       =  101;                 % # of points in z-direction
dz                      =  ThickModel/(n-1);    % z-spacing
z                       =  0:dz:ThickModel;     % z-vector
%================================================
% Material properties in dimensional units
%================================================
%                          CRUST        LITHOS
init.RockType           = [1 ;          2;       ];  % Rock types
init.Pre_exp            = [1.97e+17 ;   3.98e+16;];  % Pre-exponential factor
init.Act_energy         = [1.54e+5;     5.32e+5; ];  % Activation energy      [J/mol]
init.Act_vol            = [0.8;         1.2;     ];  % Activation Volume      [J/bar]
init.n                  = [2.3;         3.5;     ];  % Stress exponent
init.Density            = [2750;        3300;    ];  % Density (not used)     [kg/m3]
init.Cohesion           = [1e+6;        1e+6;    ];  % Cohesion               [Pa]
init.Phi                = [0.2;         0.2;     ];  % μ0 - Coeff. of Friction
final.Phi               = [0.1;         0.1;     ];  % μ1 - Coeff. of Friction
init.Conductivity       = [2.0;         2.0;     ];  % Thermal conductivity   [W/m/K ]
init.HeatCapacity       = [1000;        1000;    ];  % Spec. heat capacity    [J/kg/K]
init.RadioactiveHeat    = [1.0e-6;      2.2e-08; ];  % Radioactive heat prod. [W/m3 ]
display('RockType = 1 - CRUST ')
display('RockType = 2 - LITHOSPHERIC MANTLE')
display(['Crust thickness = ',num2str(Thick_Crust/1e+3),' Km']);
display(['Crust thickness = ',num2str(Thick_Lithos/1e+3),' Km']);
display(['Strainrate = ',num2str(Strainrate),' 1/s']);
%================================================
% set up parameter vectors
%================================================
for i=1:n
    if  z(i)<=Thick_Crust
        RockType = 1; %============== CRUST
    else
        RockType = 2; %============== LITHOSPHERIC MANTLE
    end
    k(i,1)     = init.Conductivity(RockType);
    cp(i,1)    = init.HeatCapacity(RockType);
    rho(i,1)   = init.Density(RockType);
    Hr(i,1)    = init.RadioactiveHeat(RockType);
    phi(i,1)   = init.Phi(RockType);
    C(i,1)     = init.Cohesion(RockType);
end
%================================================
% initial T-profile
%================================================
T_celsius           = zeros(n,1);
%================================================
Temp_1D(:,1)= BottomTemperature;
T_top       = TopTemperature;     %temperature at the top    [K]
T_bot       = BottomTemperature;  %temperature at the bottom [K]
%================================================
% Heat conservation equation: implicit-method
if heat_conservation_eq_implicit_method
%================================================
R = zeros(n,1);
L = sparse(n,n);
%setting boundaries
T(n,1) = T_top; %top
T(1,1) = T_bot; %bottom
for i=1:n
    if (i>1 && i<n)
        %====================================
        %calculate coefficients for left side
        %====================================
```

```
        coeff_T(1) = -k(i)/dz(i,1)^2;
        coeff_T(2) = rho(i,1)*cp(i,1)/dt-(-k(i+1,1)/dz(i,1)-k(i,1)/dz(i,1))/dz(i,1);
        coeff_T(3) = -k(i+1)/dz(i,1)^2;
    end
    %=====================================
    if (i==1)               % bottom boundary
        L(1,1) = 1;
        R(1,1) = T_bot;
    elseif (i==n)           % top boundary
        L(n,n) = 1;
        R(n,1) = T_top;
    else
        L(i,i-1) = coeff_T(1,1);
        L(i,i )  = coeff_T(1,2);
        L(i,i+1) = coeff_T(1,3);
        R(i,1 )  = rho(i,1)*cp(i,1)*T(i,1)/dt + Hr(i,1);
    end
end
%=======================================
% Solving system of equations
%=======================================
S = L\R;
T = S;
end
%=======================================
% half-space cooling model
%=======================================
if half_space_cooling_model
display('Geotherm - half space cooling model')
k = 1e-6;
t = 7e+7*365.25*86400;
for i=1:n
      T(i) = T_top+((T_bot-T_top)*erf(abs(z(i))/(2*(k*t)^0.5)));
    if temp_celsius
      T_celsius(i) = T(i) -273.15;
    end
end
end
%=======================================
% Continental geotherm
if continental_geotherm
%=======================================
Z1          = Thick_Crust+Thick_Lithos;
Hr_default  = 0.5e-6;
hr          = 10e+3;
HR          = Hr_default*exp(-z(i)/hr);
T(i) = T_top + (((T_bot-T_top)/Z1)+((HR/k(i))*(Z1/2)))*z(i)-(HR/k(i))*((z(i)^2)/2);
end
% Pressure at the surface
P_tot(1,:) = 0;
%=======================================
%compute total Pressure
for i=1:n
    if z(i)<=Thick_Crust
        RockType = 1; %============== CRUST
    else
        RockType = 2; %============== LITHOSPHERIC MANTLE
    end
    if i>1
        P_tot(1,i) = P_tot(1,i-1)+init.Density(RockType)*g*dz;
    end
end
%=======================================
% initial - strength envelope
%=======================================
strength = 0;
A  = 10^(-4.2);
G1 = 1e+9;
G0 = 9.1e+9;
Gss=3e+4;
```

```
s_peierls=zeros(n,1);
for i=1:n
    if (z(i)<=Thick_Crust)
        RockType = 1; %============== CRUST
    else
        RockType = 2; %============== LITHOSPHERIC MANTLE
    end
    ex= (init.Act_energy(RockType)+init.Act_vol(RockType)*P_tot(i)/1e+5)/8.313/T(i);
    s_visc(i) = (init.Pre_exp(RockType)*Strainrate*exp(ex))^(1/init.n(RockType));
    s_diff(i) = (init.Pre_exp(RockType)/Gss^(init.n(RockType)-1))*Strainrate*exp(ex);
    smin(i) = min([s_diff(i);s_visc(i)]);
    s_plast(i) = init.Cohesion(RockType)+P_tot(i)*init.Phi(RockType);
    if(T(i)<1473)
        s_peierls(i)=G1;
        for j=1:50
            s_peierls(i) = (1-(-1/ex*log10(Strainrate/A/s_peierls(i)^2))^0.5)*G0;
        end
        if(s_peierls(i)<0)
            s_peierls(i)=1e+30;
        end
        smin(i)= min([smin(i); s_peierls(i)]);
    end
    smin(i)= min([smin(i);s_plast(i)]);
    if Von_mises_criterion
    if smin(i) > Von_mises_value
    smin(i) = Von_mises_value;
    end
    end
    strength = strength + smin(i)*dz;
end
finder = find(smin > 10e+6);
smin_peak = max(smin);
display(['yield strength = ',num2str(smin_peak/1e+6),' MPa']);
display(['Strength = ',num2str(strength/1e+13),' x 10^13 [N/m] ']);
%=======================================
% PLOT
%=======================================
z_plot = z/1e+3;
z_max  = ((max(z))/1e+3)+2;
%=======================================
figure(1)
plot(T_celsius,z_plot,'color','r','LineWidth',1.2)
hold on
plot(s_visc/1e+6,z_plot,'--','color','c','LineWidth',1.2);
plot(s_plast/1e+6,z_plot,'--','color','g','LineWidth',1.2);
axis ij;
plot(smin/1e+6,z_plot,'k','LineWidth',1.2);
T_max = max(T_celsius); smin_max = (max(smin))/1e+6; value = [T_max; smin_max];
max_value = max(value)*1.2;
max_value1 = max(value)*1.5;
xlim([0 1300])
ylim([0 z_max])
vector_two = zeros(101,2);
vector_two(:,2) = Thick_Crust/1e3;
vector_two(:,1) = [0:max_value1/100:max_value1];
text(max_value/1.1,ThickModel/17/1e3,['B_0 = ',num2str(strength/1e+13),' x 10^{13}
[N/m]'],'HorizontalAlignment','right','color','k','FontSize',10)
%=======================================
% final - strength envelope
%=======================================
strength = 0;
s_peierls=zeros(n,1);
for i=1:n
    if (z(i)<=Thick_Crust)
        RockType = 1; %============== CRUST
    else
        RockType = 2; %============== LITHOSPHERIC MANTLE
    end
    ex= (init.Act_energy(RockType)+init.Act_vol(RockType)*P_tot(i)/1e+5)/8.313/T(i);
    s_visc(i) = (init.Pre_exp(RockType)*Strainrate*exp(ex))^(1/init.n(RockType));
```

```
    s_diff(i) = (init.Pre_exp(RockType)/Gss^(init.n(RockType)-1))*Strainrate*exp(ex);
    smin(i) = min([s_diff(i);s_visc(i)]);
    s_plast(i) = init.Cohesion(RockType)+P_tot(i)*final.Phi(RockType);

    if(T(i)<1473)
        s_peierls(i)=G1;
        for j=1:50
            s_peierls(i) = (1-(-1/ex*log10(Strainrate/A/s_peierls(i)^2))^0.5)*G0;
        end
        if(s_peierls(i)<0)
            s_peierls(i)=1e+30;
        end
        smin(i)= min([smin(i); s_peierls(i)]);
    end
    smin(i)= min([smin(i);s_plast(i)]);
    if Von_mises_criterion
    if smin(i) > Von_mises_value
    smin(i) = Von_mises_value;
    end
    end
    strength = strength + smin(i)*dz;
end
smin_peak = max(smin);
display(['yield strength = ',num2str(smin_peak/1e+6),' MPa']);
display(['Strength = ',num2str(strength/1e+13),' x 10^13 [N/m] ']);
%=======================================
% PLOT
%=======================================
z_plot = z/1e+3;
z_max  = ((max(z))/1e+3)+2;
%=======================================
figure(1)
plot(smin/1e+6,z_plot,'b','LineWidth',1.2);
xlabel(['$\sigma_{d}$ [MPa]  / T[$^{o}$C]'],'interpreter','latex','FontSize',10)
ylabel('Z - Depth [km]','FontSize',10)
axis ij;
T_max = max(T_celsius); smin_max = (max(smin))/1e+6; value = [T_max; smin_max];
legend(' Geotherm',' Flow law',' Drucker-Prager yield criterion',...
 ' Initial strength envelope',' Final strength envelope','location','bestoutside');
plot(s_visc/1e+6,z_plot,'--','color','c','LineWidth',1.0);
plot(vector_two(:,1),vector_two(:,2),'-','color','k')
plot(s_plast/1e+6,z_plot,'--','color','g','LineWidth',1.0);
plot(smin/1e+6,z_plot,'b','LineWidth',1.2);
text(max_value/1.1,ThickModel/10/1e3,['B_1 = ',num2str(strength/1e+13),...
 ' x 10^{13} [N/m]'],'HorizontalAlignment','right','color','b','FontSize',10)
text(max_value-50,Thick_Crust/1e+3/2,'Crust','HorizontalAlignment','right','FontSize',10)
text(max_value-50,Thick_Crust/1e+3,'Moho','HorizontalAlignment','right','FontSize',10)
text(max_value-50,(Thick_Lithos/1e+3/2)+Thick_Crust/1e+3,'Lithospheric
mantle','HorizontalAlignment','right','FontSize',10)
%=======================================
% SAVING PLOTS
%=======================================
if printmod
    pause(2)
    path = pwd;
    filename = 'YSE_1D';
    print ('-dpng', '-r600','-zbuffer','-cmyk',filename);
    close (figure);
    display('SAVING PLOTS.........Ok')
    display(['Saving at:' num2str(path)])
end
```

Appendix B

SINDRICO

```
% APPENDIX B ============================================ SINDRICO
%
% Luca Dal Zilio(1), Manuele Faccenda(1,2), Fabio A. Capitanio(2)
% (1) University of Padua, Department of Geosciences
% (2) Monash University, School of Geosciences
% _____________________________________________________________
% SUBDUCTION-INDUCED BREAK-UP AND DRIFTING OF CONTINENTAL PLATES
%
% CHAPTER 4: Is mantle flow a function of viscosity contrast?
%
% 2-D mechanical-viscous code;
% 9000 x 3000 km; 91 x 31 nodes; 324 x 124 markers
%=================================================================
 clear all
 close all
 clc
%=================================================================
% turn on // turn off                          1 == on || 0 == off
%=================================================================
if 1==1
    on = 1;
end
if 0==0
    off = 0;
end
%=================================================================
% on = dynamic model || off = kinematic model
slab          = off;
% color MAP
C_map         = on;
% print figures
printmod      = off;
%log-modality
log_MOD       = on;
```

```
%================= x-y domine
xsize   = 9000e+3;
ysize   = 3000e+3;
%================= number of nodes
xnum    = 91;
ynum    = 31;
%================= grid step
xstp    = xsize/(xnum-1);
ystp    = ysize/(ynum-1);
%================= gravity acceleration [m/s^2]
gy = 9.81; gx = 0;
%================= arrays
x = zeros(xnum,ynum);
y = zeros(xnum,ynum);
for i = 1 : xnum;
    for j = 1 : ynum;
        if i == 1
            x(i,j) = 0;
        else
            x(i,j) = x(i-1,j) + xstp;
        end
        if j == 1
            y(i,j) = 0;
        else
            y(i,j) = y(i,j-1) + ystp;
        end
    end
end
%=====================================================================
% markers
%=====================================================================
%vectors                 [X]                         [Y]
                x_mx = (xnum - 1)*4;      y_my = (ynum - 1)*4;
%steps
                mx_stp = xstp/4;          my_stp = ystp/4;
%arrays
                mx = zeros(x_mx,y_my);    my = zeros(x_mx,y_my);
%Physical properties
%          [lower mantle][upper mantle][rigid plate] [weak-bear.]   [slab]
rho_m  =  [ 4000;         3300;         2800;        2700;          4000  ];
eta_m  =  [ 1.5e+22;      3e+20;        3e+24;       3e+19;         3e+24 ];
eta_N  =  [ 1.5e+22;      3e+20;        3e+24;       3e+19;         3e+24 ];
%=====================================================================
display(['viscosity contrast = ',num2str(eta_m(1)/eta_m(2))]);

% lower mantle values:
% 1.5e+22  = 50x
% 3e+22    = 100x
% 4.5e+22  = 150x
%================= rock type
rt = zeros(x_mx,y_my);
%================= Lagrangian grid
for i = 1 : x_mx;
    for j = 1 : y_my;
        %******** Regular distribution of markers ********
        %         mx(i,j) = (mx_stp/2) + (mx_stp * (i-1));
        %         my(i,j) = (my_stp/2) + (my_stp * (j-1));

        %******** Random distribution of markers *********
        if(1==1)
            mx(i,j) = (mx_stp/2) + (mx_stp * (i-1));
            my(i,j) = (my_stp/2) + (my_stp * (j-1));
        else
            mx(i,j) = (mx_stp * (i-1));
            my(i,j) = (my_stp * (j-1));
            mx(i,j) =  mx(i,j)+rand(1)*mx_stp;
            my(i,j) =  my(i,j)+rand(1)*my_stp;
        end
        if my(i,j) <= 100e+3 && mx(i,j) > 300e+3 && mx(i,j) <= 8700e+3
            rt(i,j) = 3;    % rigid lithospheric plate
```

```
        elseif my(i,j) <= 100e+3 && mx(i,j) < 300e+3
            rt(i,j) = 4;    % left weak-bearing
        elseif my(i,j) <= 100e+3 && mx(i,j) >= 8700e+3
            rt(i,j) = 4;    % right weak-bearing
        % // slab? \\ %
        elseif slab == on && my(i,j) <= 2800e+3 && my(i,j) > 200e+3 && mx(i,j) >= 8900e+3
           rt(i,j)  = 5;    % slab
        elseif my(i,j) > 660e+3
            rt(i,j) = 1;    % lower mantle
        else
            rt(i,j) = 2;    % upper mantle
        end
    end
end
%==========================================================================
% - - - Scalar values - - -
D_scalar  = 3000e+3;
Nu_scalar = 1e+20;
V_scalar  = 0.05/(365.25*24*3600);  %~9 [m/year]
T         = D_scalar/V_scalar;
%==========================================================================
% - - - Characteristic values - - -
stress_scalar = (Nu_scalar)/T;
acc_scalar    = (V_scalar^2)/D_scalar;
rho_scalar    = (Nu_scalar * T)/(D_scalar^2);
%==========================================================================
% - - - dimensionless values - - -
xsize   = xsize/D_scalar;           % x size
ysize   = ysize/D_scalar;           % y size
xstp    = xstp/D_scalar;            % x-step
ystp    = ystp/D_scalar;            % y-step
x       = x/D_scalar;               % x-domain
y       = y/D_scalar;               % y-domain
mx      = mx/D_scalar;              % x-markers
my      = my/D_scalar;              % x-markers
mx_stp  = mx_stp/D_scalar;          % x-markers step
my_stp  = my_stp/D_scalar;          % y-markers step
eta_m   = eta_m/Nu_scalar;          % viscosity of the basic nodes (shear stress)
eta_N   = eta_N/Nu_scalar;          % viscosity of the additional nodes (normal stress)
rho_m = rho_m/rho_scalar;           % density
gy = gy/acc_scalar;
%================= Main loop
for ntime_stp = 1 : 1
    if C_map
       C_map  = [0 0 0;...
                 0 0.2 0.95;...                 %lower mantle
                 0 0.50196 1;...                %upper mantle
                 0.25686 0.94314 0.145686;...   %rigid lithos plate
                 0.6 0.30196 0.9;...            %bearings
                 0.50196 0.50196 0.50196;...    %5-Dark grey--Dry
                 0.6996 0.7154 0.8181;...       %6-Light grey--Wet
                 0.6 0.30196 0.9];              %0 0.50196 0
    end
    %arrays
    ETA_S = zeros(xnum,ynum);   % viscosity of the basic nodes (shear stress)
    ETA_N = zeros(xnum,ynum);   % viscosity of the additional nodes (normal stress)
    RHO   = zeros(xnum,ynum);   % density
    K     = zeros(xnum,ynum);   % thermal conductivity
    H     = zeros(xnum,ynum);   % radiogenic heating
    Cp    = zeros(xnum,ynum);   % heat capacity
    w       = zeros(xnum,ynum); % weight function
    w_eta_s = zeros(xnum,ynum); % weight function for the shear stress viscosity
    w_eta_n = zeros(xnum,ynum); % weight function for the normal stress viscosity

    %**************************************************************************
    % Defined the values in the initial Lagrangian grid, we have to interpolate
    % the corresponding values in the Eulerian nodes:
    for m = 1 : x_mx
        for n = 1 : y_my
            i = floor(mx(m,n)/xstp)+1;
```

```
        j = floor(my(m,n)/ystp)+1;

        dx = (mx(m,n) - x(i,j))/xstp; %x(i,j) == gx(i)
        dy = (my(m,n) - y(i,j))/ystp; %y(i,j) == gx(j)
        % i,j
        RHO(i,j)   = RHO(i,j) + rho_m(rt(m,n))*(1-dx)*(1-dy);
        w(i,j)     = w(i,j)   + (1-dx)*(1-dy);
        % i+1,j
        RHO(i+1,j)   = RHO(i+1,j) + rho_m(rt(m,n))*dx*(1-dy);
        w(i+1,j)     = w(i+1,j)   + dx*(1-dy);
        % i,j+1
        RHO(i,j+1)   = RHO(i,j+1) + rho_m(rt(m,n))*dy*(1-dx);
        w(i,j+1)     = w(i,j+1)   + dy*(1-dx);
        % i+1,j+1
        RHO(i+1,j+1)   = RHO(i+1,j+1) + rho_m(rt(m,n))*dx*dy;
        w(i+1,j+1)     = w(i+1,j+1)   + dx*dy;
        % (i,j) ---> Upper-left node
        if(dx <= 0.5 && dy <= 0.5)
            ETA_S(i,j)   = ETA_S(i,j) + eta_m(rt(m,n))*(1-dx)*(1-dy);
            w_eta_s(i,j) = w_eta_s(i,j) + (1-dx)*(1-dy);
        end
        % (i+1,j) ---> Upper-right node
        if(dx >= 0.5 && dy <= 0.5)
            ETA_S(i+1,j)   = ETA_S(i+1,j) + eta_m(rt(m,n))*dx*(1-dy);
            w_eta_s(i+1,j) = w_eta_s(i+1,j) + dx*(1-dy);
        end
        % (i,j+1) ---> Lower-left node
        if(dx <= 0.5 && dy >= 0.5)
            ETA_S(i,j+1)   = ETA_S(i,j+1) + eta_m(rt(m,n))*dy*(1-dx);
            w_eta_s(i,j+1) = w_eta_s(i,j+1) + dy*(1-dx);
        end
        % (i+1,j+1) ---> Lower-right node
        if(dx >= 0.5 && dy >= 0.5)

            ETA_S(i+1,j+1)   = ETA_S(i+1,j+1) + eta_m(rt(m,n))*dx*dy;
            w_eta_s(i+1,j+1) = w_eta_s(i+1,j+1) + dx*dy;
        end
        % Add viscosity etan() to the center of current cell (pressure node)
        ETA_N(i+1,j+1)   = ETA_N(i+1,j+1)+ eta_m(rt(m,n))*(abs(0.5-dx))*(abs(0.5-dy));
        w_eta_n(i+1,j+1) = w_eta_n(i+1,j+1)+(abs(0.5-dx))*(abs(0.5-dy));
    end
end
%matrixes
RHO_1  = zeros(xnum,ynum);
ETA_N1 = zeros(xnum,ynum);
ETA_S1 = zeros(xnum,ynum);
% Computing  physical properties
for i = 1 : xnum;
    for j = 1 : ynum;
        % interpolating of the new values from markers to nodes
        if w(i,j)>0
            RHO_1(i,j)  = RHO(i,j)/w(i,j);
        end
        if w_eta_s(i,j)>0
            ETA_S1(i,j) = ETA_S(i,j)/w_eta_s(i,j);
        end
        if w_eta_n(i,j)>0
            ETA_N1(i,j) = ETA_N(i,j)/w_eta_n(i,j);
        end
    end
end
%matrix
n_nodes   = xnum*ynum*3;
% Composing matrix of coefficients L()
L         = sparse(n_nodes,n_nodes);
%vector (column) of right parts R()
R         = zeros(n_nodes,1);
```

```
%********************************** 1_Solving x-y Stokes, continuity equations
%                                  * 2_continuity: dvx/dx+dvy/dy=0
%          Staggered Grid          * 3_x-Stokes: ETA_1(d2vx/dx2+d2vx/dy2)-dP/dx=0
%                                  * 4_y-Stokes: ETA_1(d2vy/dx2+d2vy/dy2)-dP/dy=gy*RHO
%    P  vx   P   vx   P   vx       *
%                                  *
%       +---vy---+---vy---+   vy   *
%       |        |        |        *
%    P  vx   P   vx   P   vx       *
%       |        |        |        *
%       +---vy---+---vy---+   vy   *
%       |        |        |        *
%    P  vx   P   vx   P   vx       *
%       |        |        |        *
%       +---vy---+---vy---+   vy   *
%                                  *
%      vx       vx       vx       *
%                                  *
%**********************************
% Process all grid points
for i = 1 : xnum
    for j = 1 : ynum
        %index
        gi  =  (i-1)*ynum+j; %global index
        gip =  gi*3-2;       %pressure
        gix =  gi*3-1;       %Vx
        giy =  gi*3;         %Vy

        %**************************************
        %         CONTINUITY EQUATION          *
        %**************************************
        %ghost pressure nodes
        if (i == 1 || j == 1)
            L(gip,gip) = 1;
            R(gip,1) = 0;

            % One cell
        elseif i == 3 && j == 2
            L(gip,gip) = 1;
            R(gip,1) = 0;

            %upper left corners
        elseif i == 2 && j == 2
            L(gip,gip) = 1;
            L(gip,gip+ynum*3) = -1;
            R(gip,gip) = 0;

            %lower left corners
        elseif i == 2 && j == ynum
            L(gip,gip) = 1;
            L(gip,gip+ynum*3) = -1;
            R(gip,1) = 0;

            %upper right corners
        elseif i == xnum && j == 2
            L(gip,gip) = 1;
            L(gip,gip-ynum*3) = -1;
            R(gip,gip) = 0;

            %lower right corners
        elseif (i == xnum && j == ynum)
            L(gip,gip) = 1;
            L(gip,gip-ynum*3) = -1;
            R(gip,gip) = 0;
        else

            %internal nodes
            %scaled P value of the internal nodes [2*eta/(xstp+ystp)]

            L(gip,gix-3)        =  1/xstp;            %Vx(i,j-1)
```

```
                L(gip,gix-3-ynum*3) = -1/xstp;          %Vx(i-1,j-1)
                L(gip,giy-ynum*3)   =  1/ystp;            %Vy(i-1,j)
                L(gip,giy-3-ynum*3) = -1/ystp;          %Vy(i-1,j-1)
                R(gip,1) = 0;
            end
            %*************************************
            %             X - STOKES               *
            %*************************************
            %ghost nodes (Vx = 0)
            if j == ynum
                L(gix,gix) = 1;
                R(gix,1)   = 0;
                %Left       Free slip x-stokes (equal to no slip conditions)
            elseif i == 1
                L(gix,gix) = 1;     %Vx = 0
                R(gix,1)   = 0;
                %Right      Free slip (equal to no slip conditions)
            elseif i == xnum
                L(gix,gix) =  1;
                R(gix,1)   =  0;
                %Top
            elseif (j == 1 && i > 1 && i <= xnum)
              %Free slip ----------------------------------vx(i,j)-vx(i,j+1)=0
                L(gix,gix)          =  1;
                L(gix,gix+3)        = -1;
                R(gix,1)            =  0;
              %No slip -----------------------------------vx=0: vx(i,j)-1/3*vx(i,j+1)=0
%                 L(gix,gix)   =  1;                                  %vx(i,j)
%                 L(gix,gix+3) = -1/3;                                %vx(i,j+1)
%                 R(gix,1)     =  0;
                %Bottom
            elseif (j == ynum-1 && i > 1 && i < xnum)
                L(gix,gix)   =  1;
                L(gix,gix-3) = -1;
                R(gix,1)     =  0;
%               No slip -----------------------------------vx=0: vx(i,j)-1/3*vx(i,j-1)=0
%               L(gix,gix)   =  1;                                  %vx(i,j)
%               L(gix,gix-3) = -1/3;                                %vx(i,j-1)
%               R(gix,1)     =  0;
            else
                %internal nodes
                L(gix,gip+3+ynum*3) =  -1/xstp;
%Pb(i+1,j+1)
                L(gix,gip+3)        =   1/xstp;
%Pa(i,j+1)
                L(gix,gix+ynum*3)   =  (2*ETA_N1(i+1,j+1))/(xstp^2);
%Vx(i+1,j)
                L(gix,gix)          =  (-(2*ETA_N1(i+1,j+1))/(xstp^2))-
((2*ETA_N1(i,j+1))/(xstp^2))-((ETA_S1(i,j+1))/(ystp^2))-((ETA_S1(i,j))/(ystp^2));
%Vx(i,j)
                L(gix,gix-ynum*3)   =  (2*ETA_N1(i,j+1))/(xstp^2);
%Vx(i-1,j)
                L(gix,gix-3)        =  ETA_S1(i,j)/(ystp^2);
%Vx(i,j-1)
                L(gix,gix+3)        =  ETA_S1(i,j+1)/(ystp^2);
%Vx(i,j+1)
                L(gix,giy+3)        =  ETA_S1(i,j+1)/(xstp*ystp);
%Vy(i,j+1)
                L(gix,giy+3-ynum*3) = -ETA_S1(i,j+1)/(xstp*ystp);
%Vy(i-1,j-1)
                L(gix,giy)          = -ETA_S1(i,j)/(xstp*ystp);
%Vy(i,j)
                L(gix,giy-ynum*3)   =  ETA_S1(i,j)/(xstp*ystp);
%Vy(i-1,j)
                R(gix,1)            = -((RHO_1(i,j)+RHO_1(i,j+1))*gx)/2;
            end
```

```
            %************************************
            %             Y - STOKES             *
            %************************************
            %ghost nodes Vy=0
            if i == xnum
                L(giy,giy) = 1;
                R(giy,1)   = 0;
                %Top
            elseif j == 1
                L(giy,giy) = 1;
                R(giy,1)   = 0;
                %Bottom
            elseif j == ynum
                L(giy,giy) = 1;
                R(giy,1)   = 0;
                %left boundary   --- free slip  Vy1-Vy2=0
            elseif (i == 1 && j > 1 && j < ynum)
                L(giy,giy)        =  1;                                    %Vy1-Vy2 = 0
                L(giy,giy+ynum*3) = -1;
                R(giy,1)          =  0;
%               no slip -------------------------------------
%               L(giy,giy)             =  1*bc_scalar;                     %vy(i,j)
%               L(giy,giy + (ynum*3))  = -1/3*bc_scalar;                   %vy(i+1,j)
%               R(giy,1)               =  0;
                %Right boundary
            elseif (i == (xnum-1) && j > 1 && j < ynum)
                %************************************
                if slab == on  % ***** dynamic model *****
                %Free slip
                L(giy,giy)        =  1;
                L(giy,giy-ynum*3) = -1;
                R(giy,1)          =  0;
                end
                %****************************************
                if slab == off % ***** kinematic model *****
%               No slip -------------------------------------
                L(giy,giy)             =  1;                               %vy(i,j)
                L(giy,giy - (ynum*3))  = -1/3;                             %vy(i-1,j)
                R(giy,1)               =  2/3;
                end
            else
                %internal nodes
                L(giy,gip+3+ynum*3)  = - 1/ystp;
%Pb(i+1,j+1)
                L(giy,gip+ynum*3)    =   1/ystp;
%Pa(i+1,j)
                L(giy,gix+ynum*3)    =   ETA_S1(i+1,j)/(xstp*ystp);
%Vx(i+1,j)
                L(giy,gix+ynum*3-3)  = - ETA_S1(i+1,j)/(xstp*ystp);
%Vx(i+1,j-1)
                L(giy,giy+ynum*3)    =   ETA_S1(i+1,j)/(xstp^2);
%Vy(i+1,j)
                L(giy,giy)           = - (ETA_S1(i+1,j)/(xstp^2))-(ETA_S1(i,j)/(xstp^2))-
((2*ETA_N1(i+1,j+1))/(ystp^2))-((2*ETA_N1(i+1,j))/(ystp^2));  %Vy(i,j)
                L(giy,gix)           = - ETA_S1(i,j)/(xstp*ystp);
%Vx(i,j)
                L(giy,gix-3)         =   ETA_S1(i,j)/(xstp*ystp);
%Vx(i,j-1)
                L(giy,giy-ynum*3)    =   ETA_S1(i,j)/(xstp^2);
%Vy(i-1,j)
                L(giy,giy+3)         =   (2*ETA_N1(i+1,j+1))/(ystp^2);
%Vy(i,j+1)
                L(giy,giy-3)         =   (2*ETA_N1(i+1,j))/(ystp^2);
%Vy(i,j-1)
                R(giy,1)             = - ((RHO_1(i,j)+RHO_1(i+1,j))*gy)/2;
            end
        end
    end
    S = L\R;
```

```
P  = zeros(xnum,ynum);
vy = zeros(xnum,ynum);
vx = zeros(xnum,ynum);
for i=1:1:xnum
    for j=1:1:ynum
        % Global index for P, vx, vy
        gi  =  (i-1)*ynum+j;%global index
        gip =  gi*3-2;      %pressure index
        gix =  gi*3-1;      %Vx index
        giy =  gi*3;        %Vy index
        % P
        P(i,j)  = S(gip)*1; % pressure
        % vx
        vx(i,j) = S(gix);   % horizontal velocity
        % vy
        vy(i,j) = S(giy);   % vertical velocity
    end
end

%**************************************
%              TIME STEP              *
%**************************************
dt = 1e+6*365.25*24*3600; %1 Myr
% Courant factor
for i = 1 : xnum;
    for j = 1 : ynum;
        if  xstp/(2*abs(vx(i,j))) < dt
            dt = xstp/(2*abs(vx(i,j)));
        end
        if  ystp/(2*abs(vy(i,j))) < dt
            dt = ystp/(2*abs(vy(i,j)));
        end
    end
end
%**************************************
%            STREAM FUNCTION           *
%**************************************
    psi   = zeros(xnum,ynum);
    for i = 2 : xnum
        for j = 1 : ynum
            psi(i,j) = psi(i-1,j) + (vy(i-1,j) * xstp);
        end
    end
    for i = 1 : xnum
        for j = 2 : ynum
            psi(i,j) = psi(i,j-1) - (vx(i,j-1) * ystp);
        end
    end
%**************************************
%              SHEAR STRESS            *
%**************************************
sgm_xy_dx = zeros(xnum,1);
sgm_xy    = zeros(xnum,ynum);
for i = 2 : 1 : xnum -1
    for j = 2 : 1 : ynum -1

        sgm_xy(i,j) = ETA_S1(i,j)*(((vx(i,j)-vx(i,j-1))/ystp)+...
            ((vy(i,j)-vy(i-1,j))/xstp));
    end
end
for i = 2 : 1 : xnum
    for j = 1 : 1 : ynum
        sgm_xy_dx(i,j) = (sgm_xy(i,j) - sgm_xy(i-1,j))/xstp;
    end
end
%**************************************
%               VORTICITY              *
%**************************************
W = zeros(xnum,ynum);
for i = 2 : 1 : xnum -1
```

```
    for j = 2 : 1 : ynum -1
        W(i,j) = 0.5*(((vx(i,j)-vx(i,j-1))/ystp)-...
                 ((vy(i,j)-vy(i-1,j))/xstp));
    end
end
%====================================================================
% re-scaling values
%====================================================================
x1 = x.*3e+3;
y1 = y.*3e+3;
mx1 = mx.*3e+3;
my1 = my.*3e+3;
%====================================================================
% PLOT --- yellow, red, green
%====================================================================
% rock type; profiles of shear stress and shear stress gradient
figure(1);
%====================================================================
subplot(3,1,1)
pcolor(mx,my,rt)
hold on
title('Rock type and stream function','FontSize', 12);
shading interp
colormap(C_map);
caxis ([0 8])
axis ij image;
xlabel('x - width');
ylabel('z - depth');
contour(x,y,psi,'color','c');
%----sxy
subplot(3,1,2)
hold on
plot(x,sgm_xy(:,2),'color','c','LineWidth',1.5);     %---! y, r, g
hold on
vector_ = zeros(91,2);
vector_(:,2) = 0;
vector_(:,1) = [0:xsize/90:xsize];
plot(vector_(:,1),vector_(:,2),'--','color','k')
ylim([-100 100])
xlim([0.5 2.7])
ylabel('shear stress','FontSize', 10);
%----sxy gradient
subplot(3,1,3)
hold on
plot(x,sgm_xy_dx(:,2),'color','c','LineWidth',1.5);  %---! y, r, g
hold on
plot(vector_(:,1),vector_(:,2),'--','color','k')
xlim([0.5 2.7])
xlabel('x - width','FontSize', 10);
ylabel('shear stress gradient','FontSize', 10);
hold on
%====================================================================
% SAVING PLOTS
if printmod
pause(2)
path = pwd;
filename = 'fig_profiles';
print ('-dpng', '-r600','-zbuffer','-cmyk',filename);
display('SAVING PLOTS.........Ok')
display(['Saving at:' num2str(path)])
end
%====================================================================
%rock type superimposed stream function
figure(2);
%====================================================================
pcolor(mx,my,rt)
shading interp
colormap(C_map);
caxis ([0 8])
hold on
```

```
contour(x,y,psi,'color','c');  %---! y, r, g
axis ij image;
title('Rock type and velocity field','FontSize',14);
xlabel('x - width');
ylabel('z - depth');
hold on
%====================================================================
%SAVING PLOTS
if printmod
pause(2)
path = pwd;
filename = 'rt_stream_func';
print('-dpng', '-r600','-zbuffer','-cmyk',filename);
close;
display('SAVING PLOTS.........Ok')
display(['Saving at:' num2str(path)])
end

%====================================================================
% Rock type superimposed stream function and velocity field
figure(3);
%====================================================================
pcolor(mx,my,rt)
shading interp
colormap(C_map);
caxis ([0 8])
hold on
contour(x,y,psi,15,'color','c');
quiver(x,y,vx,vy,'w')
axis ij image;
title('Rock type and velocity field','FontSize',14);
xlabel('x - width');
ylabel('z - depth');
%====================================================================
% SAVING PLOTS
if printmod
pause(2)
path = pwd;
filename = 'rt_vel_stream';
print ('-dpng', '-r600','-zbuffer','-cmyk',filename);
close;
display('SAVING PLOTS.........Ok')
display(['Saving at:' num2str(path)])
end
%====================================================================
% Shear stress
figure(4);
%====================================================================
if log_MOD
    for i = 2 : 1 : xnum -1
        for j = 2 : 1 : ynum -1
            if abs(sgm_xy(i,j)) < 1
                sgm_xy(i,j) = 0;
            else
                sgm_xy(i,j) = sign(sgm_xy(i,j)).*log10(abs(sgm_xy(i,j)));
            end
        end
    end
end
pcolor(x,y,sgm_xy);
hold on
title('shear stress map','FontSize', 14,'color','b');
xlabel('x - width');
ylabel('z - depth');
shading interp
axis ij image;
caxis([-2 2]);
colorbar
%colorbar('location','southoutside');
quiver(x,y,vx,vy,'k')
```

```
hold off
%=================================================================
% SAVING PLOTS
if printmod
pause(2)
path = pwd;
filename = 'map_shear_stress';
print ('-dpng', '-r600','-zbuffer','-cmyk',filename);
close;
display('SAVING PLOTS.........Ok')
display(['Saving at:' num2str(path)])
end
%=================================================================
% Vorticity MAP
figure(5);
%=================================================================
if log_MOD
    for i = 2 : 1 : xnum -1
        for j = 2 : 1 : ynum -1
            if abs(W(i,j)) < 1
                W(i,j) = 0;
            else
                W(i,j) = sign(W(i,j)).*log10(abs(W(i,j)));
            end
        end
    end
end
pcolor(x,y,W);
hold on
colorbar
%colorbar('location','southoutside');
quiver(x,y,vx,vy,'k')
axis ij image;
caxis([-1 1]);
title('vorticity map and velocity field','FontSize', 12,'color','k');
shading interp
xlabel('x - width');
ylabel('z - depth');
%=================================================================
% SAVING PLOTS
if printmod
pause(2)
path = pwd;
filename = 'map_vorticity';
print ('-dpng', '-r600','-zbuffer','-cmyk',filename);
close;
display('SAVING PLOTS.........Ok')
display(['Saving at:' num2str(path)])
end
%=================================================================
% Vx vertical profile
figure(6)
%=================================================================
z = flipud(y);
%subplot(1,2,1)
plot(vx(75,:),z,'color','c','LineWidth',1.8);   %---! y, r, g
axis ij image;
hold on
vector_plate = zeros(51,2);
vector_plate(:,2) = 0.03333;
vector_plate(:,1) = [-0.6:1.8/50:1.2];
vector_mantle = zeros(51,2);
vector_mantle(:,2) = 0.21;
vector_mantle(:,1) = [-0.6:1.8/50:1.2];
plot(vector_mantle(:,1),vector_mantle(:,2),'--','color','k')
plot(vector_plate(:,1),vector_plate(:,2),'--','color','k')
hold on
title('vx - vertical profile 75x','color','k');
xlim([-0.6 1.2])
xlabel('vx');
```

```
    ylabel('z - depth')
    hold on
    %====================================================================
    % SAVING PLOTS
    if printmod
    pause(2)
    path = pwd;
    filename = 'Vx_prof_75x';
    print ('-dpng', '-r600','-zbuffer','-cmyk',filename);
    %close;
    display('SAVING PLOTS.........Ok')
    display(['Saving at:' num2str(path)])
    end
    %====================================================================
    %Shear stress peak
    %====================================================================
    sxy_dx_peak = find(sgm_xy_dx(1:86,2)==max(sgm_xy_dx(1:86,2)));
    dist_shear_stress_gradient = sxy_dx_peak*100;
    dist_sxy_dx_peak_from_trench = 9000-dist_shear_stress_gradient;
    display(['X Node - shear stress gradient peak: ', num2str(sxy_dx_peak), ' /90']);
    display(['distance_sxy-peak - trench: ', num2str(dist_sxy_dx_peak_from_trench),' km'])

end
```

Bibliography

Alvarez, Walter. 1974. Fragmentation of the Alpine orogenic belt by microplate dispersal. *Nature*, 248, 309–314.

Anderson, Don L. 2010. Hawaii, boundary layers and ambient mantle—geophysical constraints. *Journal of Petrology*, egq068.

Argand, Emile. 1924. La tectonique de l'Asie. Conférence faite á Bruxelles, le 10 août 1922. *Compte-rendu du XIII° Congrès géologique international (XIIIe session)-Belgique 1922*, 171–372.

Bercovici, David. 2003. The generation of plate tectonics from mantle convection. *Earth and Planetary Science Letters*, 205(3), 107–121.

Birch, Francis. 1965. Energetics of core formation. *Journal of Geophysical Research*, 70(24), 6217–6221.

Bird, Peter. 2003. An updated digital model of plate boundaries. *Geochemistry, Geophysics, Geosystems*, 4(3).

Burov, Evgene B, & Diament, Michel. 1995. The effective elastic thickness (T e) of continental lithosphere: What does it really mean? *Journal of Geophysical Research: Solid Earth (1978–2012)*, 100(B3), 3905–3927.

Carminati, Eugenio, Lustrino, Michele, & Doglioni, Carlo. 2012. Geodynamic evolution of the central and western Mediterranean: Tectonics vs. igneous petrology constraints. *Tectonophysics*, 579, 173–192.

Carter, Neville L, & Tsenn, Michael C. 1987. Flow properties of continental lithosphere. *Tectonophysics*, 136(1), 27–63.

Cavazza, William, & Barone, Mirko. 2010. Large-scale sedimentary recycling of tectonic mélange in a forearc setting: The Ionian basin (Oligocene–Quaternary, southern Italy). *Geological Society of America Bulletin*, 122(11-12), 1932–1949.

Chapple, William M, & Tullis, Terry E. 1977. Evaluation of the forces that drive the plates. *Journal of geophysical research*, 82(14), 1967–1984.

Christensen, Ulrich. 1982. Phase boundaries in finite amplitude mantle convection. *Geophysical Journal International*, 68(2), 487–497.

Cloetingh, Sierd, & Burov, Evgene B. 1996. Thermomechanical structure of European continental lithosphere: constraints from rheological profiles and EET estimates. *Geophysical Journal International*, 124(3), 695–723.

Connolly, JAD. 2005. Computation of phase equilibria by linear programming: a tool for geodynamic modeling and its application to subduction zone decarbonation. *Earth and Planetary Science Letters*, 236(1), 524–541.

Crameri, F, Schmeling, H, Golabek, GJ, Duretz, T, Orendt, R, Buiter, SJH, May, DA, Kaus, BJP, Gerya, TV, & Tackley, PJ. 2012. A comparison of numerical surface topography calculations in geodynamic modelling:

An evaluation of the 'sticky air'method. *Geophysical Journal International*, 189(1), 38–54.

Davies, Geoffrey F. 1977. Viscous mantle flow under moving lithospheric plates and under subduction zones. *Geophysical Journal International*, 49(3), 557–563.

Davies, Geoffrey Frederick. 1999. *Dynamic Earth: Plates, plumes and mantle convection*. Cambridge University Press.

Davies, J. Huw, & Stevenson, D. J. 1992. Physical model of source region of subduction zone volcanics. *Journal of Geophysical Research: Solid Earth*, 97(B2), 2037–2070.

Dewey, JF, Helman, ML, Knott, SD, Turco, E, & Hutton, DHW. 1989. Kinematics of the western Mediterranean. *Geological Society, London, Special Publications*, 45(1), 265–283.

Dickinson, William R, & Snyder, Walter S. 1979. Geometry of subducted slabs related to San Andreas transform. *The Journal of Geology*, 609–627.

Doglioni, Carlo, Ismail-Zadeh, Alik, Panza, Giuliano, & Riguzzi, Federica. 2011. Lithosphere–asthenosphere viscosity contrast and decoupling. *Physics of the Earth and Planetary Interiors*, 189(1), 1–8.

Dziewonski, Adam M, & Anderson, Don L. 1981. Preliminary reference Earth model. *Physics of the earth and planetary interiors*, 25(4), 297–356.

Faccenda, M. 2014a. Mid mantle seismic anisotropy around subduction zones. *Physics of the Earth and Planetary Interiors*, 227, 1–19.

Faccenda, Manuele. 2014b. Water in the slab: A trilogy. *Tectonophysics*, 614, 1–30.

Faccenda, Manuele, & Capitanio, FA. 2013. Seismic anisotropy around subduction zones: Insights from three-dimensional modeling of upper mantle deformation and SKS splitting calculations. *Geochemistry, Geophysics, Geosystems*, 14(1), 243–262.

Faccenda, Manuele, Gerya, Taras V, & Burlini, Luigi. 2009. Deep slab hydration induced by bending-related variations in tectonic pressure. *Nature Geoscience*, 2(11), 790–793.

Faccenna, Claudio, Becker, Thorsten W, Lucente, Francesco Pio, Jolivet, Laurent, & Rossetti, Federico. 2001. History of subduction and back arc extension in the Central Mediterranean. *Geophysical Journal International*, 145(3), 809–820.

Fornberg, B. *A Practical Guide to Pseudospectral Methods*. Cambridge University Press.

Forsyth, Donald, & Uyeda, Seiya. 1975. On the relative importance of the driving forces of plate motion. *Geophysical Journal International*, 43(1), 163–200.

Fukao, Yoshio, Obayashi, Masayuki, Inoue, Hiroshi, & Nenbai, Masakazu. 1992. Subducting slabs stagnant in the mantle transition zone. *Journal of Geophysical Research: Solid Earth (1978–2012)*, 97(B4), 4809–4822.

Fukao, Yoshio, Obayashi, Masayuki, & Nakakuki, Tomoeki. 2009. Stagnant slab: a review. *Annual Review of Earth and Planetary Sciences*, 37, 19–46.

Gerya, T. *Introduction to Numerical Geodynamic Modelling*. Cambridge University Press.

Gerya, Taras. 2011. Future directions in subduction modeling. *Journal of Geodynamics*, 52(5), 344–378.

Gerya, Taras. 2014. Precambrian geodynamics: concepts and models. *Gondwana Research*, 25(2), 442–463.

Gerya, Taras V., & Yuen, David A. 2003. Characteristics-based marker-in-cell method with conservative finite-differences schemes for modeling geological flows with strongly variable transport properties. *Physics of the Earth and Planetary Interiors*, 140(4), 293 – 318.

Gerya, Taras V, & Yuen, David A. 2007. Robust characteristics method for modelling multiphase visco-elasto-plastic thermo-mechanical problems. *Physics of the Earth and Planetary Interiors*, 163(1), 83–105.

Gerya, Taras V, Connolly, James AD, & Yuen, David A. 2008. Why is terrestrial subduction one-sided? *Geology*, 36(1), 43–46.

Grand, Stephen P. 1994. Mantle shear structure beneath the Americas and surrounding oceans. *Journal of Geophysical Research: Solid Earth (1978–2012)*, 99(B6), 11591–11621.

Grand, Stephen P, van der Hilst, Rob D, & Widiyantoro, Sri. 1997. Global seismic tomography: A snapshot of convection in the Earth. *GSA today*, 7(4), 1–7.

Gung, Yuancheng, Panning, Mark, & Romanowicz, Barbara. 2003. Global anisotropy and the thickness of continents. *Nature*, 422(6933), 707–711.

Gurnis, Michael. 1988. Large-scale mantle convection and the aggregation and dispersal of supercontinents. *Nature*, 332(6166), 695–699.

Hess, Harry H. 1962. History of ocean basins. *Petrologic studies*, 4, 599–620.

Hofmeister, A. M. 1999. Mantle Values of Thermal Conductivity and the Geotherm from Phonon Lifetimes. *Science*, 283(5408), 1699–1706.

Holmes, Arthur. 1931. Radioactivity and earth movements. *Nature*, 128, 496.

Huang, Jinli, & Zhao, Dapeng. 2006. High-resolution mantle tomography of China and surrounding regions. *Journal of Geophysical Research: Solid Earth (1978–2012)*, 111(B9).

Jolivet, L, Daniel, JM, Truffert, C, & Goffé, B. 1994a. Exhumation of deep crustal metamorphic rocks and crustal extension in arc and back-arc regions. *Lithos*, 33(1), 3–30.

Jolivet, Laurent, & Faccenna, Claudio. 2000. Mediterranean extension and the Africa-Eurasia collision. *Tectonics*, 19(6), 1095–1106.

Jolivet, Laurent, Tamaki, Kensaku, & Fournier, Marc. 1994b. Japan Sea, opening history and mechanism: A synthesis. *Journal of Geophysical Research: Solid Earth (1978–2012)*, 99(B11), 22237–22259.

Karato, Shun-ichiro. 2010. Rheology of the deep upper mantle and its implications for the preservation of the continental roots: A review. *Tectonophysics*, 481(1), 82–98.

Karato, Shun-ichiro, & Wu, Patrick. 1993. Rheology of the upper mantle: A synthesis. *Science*, 260(5109), 771–778.

Karato, Shun-ichiro, Riedel, Michael R, & Yuen, David A. 2001. Rheological structure and deformation of subducted slabs in the mantle transition zone: implications for mantle circulation and deep earthquakes. *Physics of the Earth and Planetary Interiors*, 127(1), 83–108.

Katayama, Ikuo, & Karato, Shun-ichiro. 2008. Low-temperature, high-stress deformation of olivine under water-saturated conditions. *Physics of the Earth and Planetary Interiors*, 168(3), 125–133.

Lei, Jianshe, & Zhao, Dapeng. 2005. P-wave tomography and origin of the Changbai intraplate volcano in Northeast Asia. *Tectonophysics*, 397(3), 281–295.

Lowrie, William. 2007. *Fundamentals of geophysics*. Cambridge University Press.

Lux, Richard A, Davies, Geoffrey F, & Thomas, John H. 1979. Moving lithospheric plates and mantle convection. *Geophysical Journal International*, 58(1), 209–228.

Malinverno, Alberto, & Ryan, William BF. 1986. Extension in the Tyrrhenian Sea and shortening in the Apennines as result of arc migration driven by sinking of the lithosphere. *Tectonics*, 5(2), 227–245.

McKenzie, DP. 1977. The initiation of trenches. *Island arcs, deep sea trenches and back-arc basins*, 57–61.

Mele, Giuliana, Rovelli, Antonio, Seber, Dogan, Hearn, Thomas M, & Barazangi, Muawia. 1998. Compressional velocity structure and anisotropy in the uppermost mantle beneath Italy and surrounding regions. *Journal of Geophysical Research: Solid Earth (1978–2012)*, 103(B6), 12529–12543.

Melosh, Jay. 1977. Shear stress on the base of a lithospheric plate. *pure and applied geophysics*, 115(1-2), 429–439.

Miller, Meghan S, & Kennett, Brian LN. 2006. Evolution of mantle structure beneath the northwest Pacific: Evidence from seismic tomography and paleogeographic reconstructions. *Tectonics*, 25(4).

Mishin, Yury A, Gerya, Taras V, Burg, Jean-Pierre, & Connolly, James AD. 2008. Dynamics of double subduction: Numerical modeling. *Physics of the Earth and Planetary Interiors*, 171(1), 280–295.

Moresi, L., Dufour, F., & MÃhlhaus, H.-B. 2003. A Lagrangian integration point finite element method for large deformation modeling of viscoelastic geomaterials. *Journal of Computational Physics*, 184(2), 476 – 497.

Okino, Kyoko, Ando, Masataka, Kaneshima, Satoshi, & Hirahara, Kazuro. 1989. The horizontally lying slab. *Geophysical Research Letters*, 16(9), 1059–1062.

Pan, Frank, & Acrivos, Andreas. 1967. Steady flows in rectangular cavities. *Journal of Fluid Mechanics*, 28(04), 643–655.

Panza, Giuliano, Doglioni, Carlo, & Levshin, Anatoli. 2010. Asymmetric ocean basins. *Geology*, 38(1), 59–62.

Peltier, W Richard. 1989. *Mantle Convection: Plate tectonics and global dynamics*. Vol. 4. CRC Press.

Piromallo, C, Becker, TW, Funiciello, F, & Faccenna, C. 2006. Three-dimensional instantaneous mantle flow induced by subduction. *Geophysical Research Letters*, 33(8).

Piromallo, Claudia, & Morelli, Andrea. 2003. P wave tomography of the mantle under the Alpine-Mediterranean area. *Journal of Geophysical Research: Solid Earth (1978–2012)*, 108(B2).

Pollack, Henry N. 1986. Cratonization and thermal evolution of the mantle. *Earth and Planetary Science Letters*, 80(1), 175–182.

Ranalli, G. 1994. Nonlinear flexure and equivalent mechanical thickness of the lithosphere. *Tectonophysics*, 240(1), 107–114.

Ranalli, Giorgio. 1995. *Rheology of the Earth*. Springer.

Ren, Yong, Stutzmann, Eléonore, Van Der Hilst, Robert D, & Besse, Jean. 2007. Understanding seismic heterogeneities in the lower mantle beneath the Americas from seismic tomography and plate tectonic history. *Journal of Geophysical Research: Solid Earth (1978–2012)*, 112(B1).

Schmeling, Harro. 1987. On the relation between initial conditions and late stages of Rayleigh-Taylor instabilities. *Tectonophysics*, 133(1â“2), 65 – 80.

Schmid, Christian, Goes, Saskia, van der Lee, Suzan, & Giardini, Domenico. 2002. Fate of the Cenozoic Farallon slab from a compar-

ison of kinematic thermal modeling with tomographic images. *Earth and Planetary Science Letters*, 204(1), 17–32.

Schubert, Gerald, Yuen, David A, & Turcotte, Donald L. 1975. Role of phase transitions in a dynamic mantle. *Geophysical Journal International*, 42(2), 705–735.

Schubert, Gerald, Stevenson, David, & Cassen, Patrick. 1980. Whole planet cooling and the radiogenic heat source contents of the Earth and Moon. *Journal of Geophysical Research: Solid Earth (1978–2012)*, 85(B5), 2531–2538.

Schubert, Gerald, Turcotte, Donald L, & Olson, Peter. 2001. *Mantle Convection in the Earth and Planets 2 Volume Set*. Cambridge University Press.

Seton, M, Müller, RD, Zahirovic, S, Gaina, C, Torsvik, T, Shephard, G, Talsma, A, Gurnis, M, Turner, M, Maus, S, *et al.* . 2012. Global continental and ocean basin reconstructions since 200Ma. *Earth-Science Reviews*, 113(3), 212–270.

Stock, JM, & Hodges, KV. 1989. Pre-Pliocene Extension around the Gulf of California and the transfer of Baja California to the Pacific Plate. *Tectonics*, 8(1), 99–115.

Sutton, J. 1963. Long-term cycles in the evolution of the continents.

Tackley, Paul J, Stevenson, David J, Glatzmaier, Gary A, & Schubert, Gerald. 1993. Effects of an endothermic phase transition at 670 km depth in a spherical model of convection in the Earth's mantle. *Nature*, 361(6414), 699–704.

Torrance, K, Davis, R, Eike, K, Gill, P, Gutman, D, Hsui, A, Lyons, S, & Zien, H. 1972. Cavity flows driven by buoyancy and shear. *Journal of Fluid Mechanics*, 51(02), 221–231.

Turcotte, D.L., & Schubert, G. *Geodynamics*. Cambridge University Press.

Turcotte, Donald L, & Emerman, Steven H. 1983. Mechanisms of active and passive rifting. *Tectonophysics*, 94(1), 39–50.

Turcotte, Donald L, & Oxburgh, ER. 1972. Mantle convection and the new global tectonics. *Annual Review of Fluid Mechanics*, 4(1), 33–66.

van der Hilst, Rob, & Seno, Tetsuzo. 1993. Effects of relative plate motion on the deep structure and penetration depth of slabs below the Izu-Bonin and Mariana island arcs. *Earth and Planetary Science Letters*, 120(3), 395–407.

van der Lee, Suzan, & Nolet, Guust. 1997. Seismic image of the subducted trailing fragments of the Farallon plate. *Nature*, 386(6622), 266–269.

Wegener, Alfred. 1920. *Die entstehung der kontinente und ozeane*. Vol. 66. F. Vieweg.

Weinberg, Roberto Ferrez, & Schmeling, Harro. 1992. Polydiapirs: multiwavelength gravity structures. *Journal of Structural Geology*, 14(4), 425 – 436.

Wilson, J Tuzo. 1966. *Did the Atlantic close and then re-open?* Nature.

Woidt, W.-D. 1978. Finite element calculations applied to salt dome analysis. *Tectonophysics*, 50(2â“3), 369 – 386.

Acknowledgment

First of all, I would like to express my gratitude to my supervisor Manuele Faccenda, for giving me the chance to work in this project and for all the support and guidance over the last year. Thanks Manuele for brilliant intuitions, your never-ending enthusiasm, for critical review of this thesis, for your fabulous numerical modeling skills and, above all, for your friendship. You are one of the best teachers I've ever met.

I am grateful to my office mates and the entire HAPG-group for making these two years of master an unforgettable experience! I would like to specially mention Alberto, Andrea, Chiara, Matteo and Giacomo with whom I shared many great moments with regard to science, food, culture and sports, always combined with a lots of beer!

My life in Treviso would not be so great without support of my friends. Thank you Federico, Matteo, Beppe, Mirko and Susy for the nights spent together or just to inspire me to think about something else than mantle convection, subduction and break-up, at least for a while...

Infinite gratitude goes to my parents and my sister, that represent the roots of my existence and that I feel as part of myself. In particular I am grateful to my father Paolo and my grandmother Maria, for all the years of support and encouragement. My years of study here at the University of Padua would have been much harder without the financial and, above all, the mental backing of my family. Thanks for everything!

The last paragraph of this thesis is dedicated to someone special, Federica. I am very grateful to my lovely girlfriend, who was and who is with me all the time from the beginning of my studies and gave me a great support in every step of my life, only you really know how much effort I put in over the last five years! You deserve my deepest thank for the love that you have given me, for your infinite patience in tolerating all the ups and downs of my life as a master student and for your constant loving encouragement. This experience would not have been the same without your love.